学位論文

Formation and growth of massive black holes in the early universe

（宇宙初期での大質量ブラックホールの形成と成長）

平成29年12月　博士（理学）申請

東京大学大学院 理学系研究科
物理学専攻

櫻井 祐也

ABSTRACT

Observations of high-redshift quasars have revealed the existence of supermassive black holes (SMBHs) in the early universe. Importantly, the SMBHs are believed to have grown within 1 Gyr to as massive as $\gtrsim 10^9$ solar masses ($\mathrm{M}_\odot$), suggesting a big problem in the context of structure formation in the early universe that "how does a SMBH grow so fast?".

As origins of the high-redshift SMBHs, theoretical astrophysicists often consider that a small 'seed' BH, left as a remnant of a massive star, grows via gas accretion and mergers to become a SMBH. As a comparative model for formation of such a seed, a BH of mass $\sim 100\,\mathrm{M}_\odot$, which is left after death of a first star or a Population III (Pop III) star, is thought to grow via a nearly Eddington accretion rate. This means that a SMBH of mass $\sim 10^9\,\mathrm{M}_\odot$ is marginally formed within the age of the universe at $z \sim 6$. Unfortunately, this model has a problem that the BH growth is delayed due to effects of radiation, which is emitted when gravitational energy is released from accreting gas and is converted to radiation energy. This radiation feedback significantly suppresses the accretion rate well below the Eddington accretion rate and makes the SMBH formation impossible by the Pop III BH model.

As alternative models to facilitate the formation of the high-redshift SMBHs, there are three models: the direct collapse model, the super-Eddington accretion model and the runaway stellar collision model. These models have been intensively studied by many authors, but there still remain many things to be examined. Specifically, previous works often consider idealized situations, whereby the validity of the models cannot be correctly discussed.

In this thesis, we study the BH formation models by considering more realistic situations in order to examine the validity of the models.

First, we work on the direct collapse model, where a supermassive star (SMS) of mass $\sim 10^5\,\mathrm{M}_\odot$ almost entirely collapses at the end of stellar lifetime, directly leaving a $\sim 10^5\,\mathrm{M}_\odot$ BH. A SMS can form under peculiar conditions, e.g., inside an atomic-cooling halo strongly irradiated by Lyman-Werner radiation emitted from external sources, whereby a rapid gas accretion of $\sim 0.1 - 1\,M_\odot\,\mathrm{yr}^{-1}$ on to a growing protostar is realized. However, there is a problem that, during the formation of a SMS via rapid gas accretion, strong stellar radiation is expected to stop the accretion by UV radiation feedback. To clarify if the expectation is true or not, Hosokawa et al. (2013) compute stellar evolution of the accreting SMS, by assuming a constant accretion rate. They find that a growing SMS is actually largely inflated with a low surface temperature of $\sim 5000\,\mathrm{K}$ and emit a small amount of UV photons to cause the UV feedback. The SMS evolution is contrasted to a relatively slowly accreting Pop III star which contracts and emit a significant amount of UV radiation. In a more realistic case, the accretion history will be highly variable with time, since the accretion occurs through a gravitationally unstable disk where fragments form and migrate to fall on to the central protostar, causing accretion bursts. In this case, the evolution of the growing SMS can be affected if there are long, quiescent accretion phases during which the star can contract.

We examine stellar evolution of an accreting SMS with a highly variable, episodic accretion history, where burst accretion followed by quiescent accretion is repeated. We construct an analytic model of

episodic accretion histories with parameters characterizing the burst and quiescent phases, and then calculate the evolution. It is found that the SMS significantly contracts during the quiescent phases and emits a copious amount of UV photons, likely resulting in the efficient radiation feedback, if the length of the quiescent phases is longer than a thousand years. We also investigate the effect of a more realistic episodic accretion history, which is obtained from 2D hydrodynamics simulations of a gravitationally unstable disk, on the SMS evolution. In this case, the duration of the quiescent phases is typically shorter than $10^3\,\mathrm{yr}$ and the accreting protostar does not contract. Then, the protostar is able to grow to become as massive as $\sim 10^5\,\mathrm{M}_\odot$ without UV feedback and the direct collapse BH formation is viable.

Next, we study the super-Eddington model, in which a BH grows with very rapid super-Eddington gas accretion and becomes a SMBH in a short time. How can such super-Eddington accretion be realized? It is naively expected that such a rapid gas accretion flow near the BH causes strong radiation force with emitting nearly Eddington luminosity, which halts the accretion and stops the BH growth. Photon trapping, however, is thought to reduce the emerging luminosity. In fact, several studies including numerical simulations and (semi-)analytical studies show that the super-Eddington accretion is not prevented by the radiation force within the BH accretion flow near the BH. On the other hand, radiation heating can suppress gas accretion at larger scales where gas pressure and BH gravity is comparable. Thus, the small and large scale regions need to be self-consistently investigated. To this end, Inayoshi, Haiman & Ostriker (2016) perform a 1D radiation hydrodynamical simulation of a spherical accretion flow at the large scales, assuming a functional form of luminosity emerging from the central region, which is at most the Eddington luminosity for this spherical case. They find that transition occurs from the usual Eddington accretion to a 'hyper-Eddington' accretion, which is essentially a Bondi accretion. The transition occurs because an ionized region is initially smaller than the Bondi radius at which BH gravity balances gas pressure. More realistically, however, the emerging luminosity can exceed the Eddington luminosity due to the deviation from the spherical morphology, i.e., due to formation of an accretion disk where emitting radiation can preferentially escape through polar directions.

We examine the large-scale BH accretion flow with a super-Eddington luminosity source by performing 1D radiation hydrodynamics simulations, in order to see whether the transition to the steady hyper-Eddington accretion occurs in this high-luminosity case. We construct an analytical model of the central source which exceeds the Eddington luminosity. It is shown that the transition occurs even when the luminosity reaches at most 100 times the Eddington luminosity. We argue, using analytic models and numerical results, that the transition is realized because ram pressure of accreting gas in addition to gas gravity overcomes the radiation force from the super-Eddington luminosity source. Thus, the BH growth would continue not to be halted by the strong radiation.

Finally, we study the runaway stellar collision model, in which stars in a dense star cluster successively collide and merge with a specific star residing near the center. The star eventually becomes as massive as $\sim 1000\,\mathrm{M}_\odot$ and collapses to leave an intermediate-mass BH (IMBH), possibly serving as a seed for forming a SMBH at high redshift. Although several studies have shown that star cluster formation is likely to occur within metal-enriched atomic-cooling halos in the early universe, it is still uncertain whether such a runaway collision process is prevalent. Katz, Sijacki & Haehnelt (2015) perform direct N-body simulations of star clusters formed in a mini-halo system, which is identified in cosmological simulations. They show that the runaway collision and IMBH formation are very likely outcomes in mini-halos.

This work encourages us to statistically examine the star cluster dynamics and evolution for clusters forming in atomic-cooling halos. We first perform cosmological simulations to find star cluster forming sites. We then generate star cluster initial conditions for direct N-body simulations assuming star formation efficiency and an initial mass function. For the star clusters, direct N-body simulations are conducted, to follow stellar collisions and mergers. It is found that in all the clusters except one the runaway stellar collisions occur and massive stars of mass $400 - 1900\,\mathrm{M}_{\odot}$ form, which would leave IMBHs at the end of their lives. The diversity of the final stellar masses is attributed to the diversity of the parent atomic-cooling halo properties as virial mass, central gas density and central gas velocity dispersion. We also derive an IMBH mass-cluster mass relation for our simulated clusters and compare it with a SMBH mass-bulge mass relation in the local universe.

We conclude that the three models are viable until the seed BH formation. However, it is still unclear whether the seed BHs grow to the SMBHs. In future works, we will study the subsequent evolution in the context of the three models considered in this thesis. Specifically, we will follow the evolution and growth of the IMBHs left inside the star clusters (Chapter 5). We will focus on tidal disruption of stars and BH merger which would occur during the IMBH growth and estimate the event rates to compare to the future X-ray/gravitational-wave observations. The comparison would greatly help us to further understand the origin of the SMBHs in the early universe.

ACKNOWLEDGEMENT

I express my heartfelt thanks to my supervisor, Naoki Yoshida, who introduces to me the interesting and worthwhile topic and always guides me to correct way during my Ph.D. course. His teachings and advises not only encourage me to achieve my studies but also importantly affect my way of thinking about things which must be essential to my later life. I am really thankful to my collaborators Takashi Hosokawa and Harold W. Yorke, who teach me how to use the sophisticated stellar evolution code STELLAR and enthusiastically support me to complete my first two studies. I am very grateful to my collaborators Eduard I. Vorobyov and Kazuyuki Omukai, who help me to accomplish my second study where their supports are indispensable. I express my gratitude to my collaborators, Kohei Inayoshi and Zoltán Haiman for their hospitality during my three-month stay at Columbia University from January 2nd to March 30th, 2016. Their insightful knowledges and advises are essential to obtain very interesting and meaningful results when writing the third paper. I express my appreciation to my collaborators Michiko S. Fujii, who teach me to use the direct N-body code BRIDGE, and Shingo Hirano, who give me very valuable knowledges about early structure formation. Their supports are essential when I finish my fourth study.

I spend my 5 year Ph.D. course at Hongo Campus of the University of Tokyo and I express my heartfelt gratitude to the group members. Seminars and meetings that I have shared time with them are always fruitful, increasing and polishing my knowledge and broadening my perspectives through questions and discussions. I also show appreciation to SOCs and LOCs who organize fruitful meetings, workshops and symposiums I have attended. They give me opportunities to present my works through talks or posters, as well as to exchange opinions with astronomers and astrophysicists in the world. In some meetings and workshops, they also kindly financially support me.

I am very thankful to the examiners, Noriko Yamasaki (chief), Akito Kusaka, Fujihiro Hamba, Masahiro Kawasaki and Kipp Cannon, who have taken time to read this thesis and have greatly helped me to improve this thesis through fruitful discussions and comments.

I am very thankful to my family who always support me in my daily life. Their ongoing support is also indispensable when I complete my works during this 5 year Ph.D. course.

In this thesis, numerical calculations and simulations are partly performed on PC cluster and Cray XC30 at Center for Computational Astrophysics, National Astronomical Observatory of Japan. The figures in this thesis are in part generated using Gnuplot[*1], Matplotlib[*2], yt[*3] and Inkscape[*4]. The works in this thesis are partly supported by Advanced Leading Graduate Course for Photon Science (ALPS) and Grant-in-Aid for Japan Society for the Promotion of Science (JSPS) Research Fellow.

[*1] http://www.gnuplot.info

[*2] https://matplotlib.org

[*3] http://yt-project.org

[*4] https://inkscape.org

Contents

Chapter 1

Introduction

1.1 Observations of supermassive black holes lurking in the distant universe

In the past decade, observations of the distant universe have revealed the existence of supermassive black holes (SMBHs) with mass $\sim 10^9$ $\mathrm{M}_\odot$ at high redshift $z \gtrsim 6$ or the age of the universe $\lesssim 1$ Gyr (e.g., Fan et al. 2001, Jiang et al. 2007, Kurk et al. 2007, Willott et al. 2010, Mortlock et al. 2011, Venemans et al. 2013, De Rosa et al. 2014, Wu et al. 2015, Mazzucchelli et al. 2017, Bañados et al. 2017). The origin of these high redshift SMBHs remain to be elucidated.

In Figure 1.1, we show the BH mass M_{BH} of observed quasars at $z \gtrsim 6$ whose masses have been estimated. The observed quasars are summarized in Table 1.1.

1.1.1 Eddington ratios

A large fraction of the high-redshift quasars emits luminosity of nearly the Eddington limit, i.e., accreting at nearly the Eddington accretion rate. In Figure 1.2, we plot bolometric luminosity versus BH mass of the high-redshift quasars (Table 1.1). The Eddington ratios for the high-redshift quasars range $\sim 0.1 - 1$, which is comparable to the ratios for the quasars at $z < 4$ (Kollmeier et al. 2006).

For comparison, the bolometric luminosity versus mass of compact objects for the local ultra-luminous X-ray sources (ULXs; Table 1.2) are also shown in Figure 1.2. For the ULXs, the luminosity can significantly exceed the Eddington limit with a range of $\sim 1 - 100\times$ the Eddington luminosity, indicating that the super-Eddington accretion on to the compact objects occurs.

1.2 Theoretical models of SMBH formation in the early universe

In many theoretical works which attempt to elucidate the origin of the SMBHs at $z \gtrsim 6$, small 'seed' BHs of mass $100 - 10^5$ $\mathrm{M}_\odot$ are often deemed as the initial states and then grow to the SMBHs via mass accretion and mergers with other BHs. The evolution of the seed BH mass is estimated by the following equation:

$$\frac{\mathrm{d}M_{\mathrm{BH}}}{\mathrm{d}t} = (1-\epsilon)\dot{m} = \left(\frac{1-\epsilon}{\epsilon}\right)\left(\frac{L}{L_{\mathrm{Edd}}}\right)\frac{M_{\mathrm{BH}}}{t_{\mathrm{Edd}}}, \tag{1.1}$$

where ϵ is radiative efficiency of accreting gas, $\dot{m} = L/\epsilon c^2$ is a total mass accretion rate, L is an accretion luminosity, L_{Edd} is the Eddington luminosity and $t_{\mathrm{Edd}} \equiv M_{\mathrm{BH}}c^2/L_{\mathrm{Edd}}$ is the Eddington

Table 1.1 High-z quasars observed at $z \gtrsim 6$ whose masses are estimated.

Name	Redshift	$M_{\rm BH}$ $(10^9\,{\rm M}_\odot)$	$L_{\rm bol}$ $(10^{47}\,{\rm erg\,s^{-1}})$	$L_{\rm bol}/L_{\rm Edd}$	References
VIK J0109-3047	6.7909 ± 0.0004	$1.33^{+0.38}_{-0.62}$	$0.51^{+0.05}_{-0.06}$	$0.29^{+0.88}_{-2.59}$	[1]
PSO J036.5078+03.0498	6.541 ± 0.002	$3.00^{+0.92}_{-0.77}$	$2.0^{+0.22}_{-0.64}$	$0.51^{+0.17}_{-0.21}$	[1]
VIK J0305-3150	6.6145 ± 0.0001	$0.90^{+0.29}_{-0.27}$	$0.75^{+0.10}_{-0.34}$	$0.64^{+2.20}_{-3.42}$	[1]
PSO J167.6415-13.4960	6.5148 ± 0.0005	$0.30^{+0.08}_{-0.12}$	$0.47^{+0.16}_{-0.22}$	$1.22^{+0.51}_{-0.75}$	[1]
ULAS J1120+0641	7.0842 ± 0.0004	$2.47^{+0.62}_{-0.67}$	$1.83^{+0.19}_{-0.072}$	$0.57^{+0.16}_{-0.27}$	[1, 2]
HSC J1205-0000	6.73 ± 0.02	$4.7^{+1.2}_{-3.9}$	$0.36^{+0.18}_{-0.20}$	$0.06^{+0.32}_{-0.58}$	[1]
PSO J231.6576-20.8335	6.5864 ± 0.0005	$3.05^{+0.44}_{-2.24}$	$1.89^{+0.34}_{-0.45}$	$0.48^{+0.11}_{-0.39}$	[1]
PSO J247.2970+24.1277	6.476 ± 0.004	$0.52^{+0.22}_{-0.25}$	$1.77^{+0.06}_{-0.76}$	$2.60^{+0.08}_{-0.15}$	[1]
PSO J323.1382+12.2986	6.5881 ± 0.0003	$1.39^{+0.32}_{-0.51}$	$0.81^{+0.07}_{-0.50}$	$0.44^{+1.09}_{-3.19}$	[1]
PSO J338.2298+29.5089	6.666 ± 0.004	$2.70^{+0.85}_{-0.97}$	$0.4^{+0.2}_{-0.1}$	$0.11^{+0.71}_{-0.49}$	[1]
VIK J2348-3054	6.9018 ± 0.0007	$1.98^{+0.57}_{-0.84}$	$0.43^{+0.20}_{-0.13}$	$0.17^{+0.92}_{-0.88}$	[1]
SDSS J010013.02+280225.8	6.30 ± 0.01	$12.4^{+1.9}_{-1.9}$	16.2	$1.0^{\rm a}$	[3]
J2229+1457	6.1517 ± 0.0005	$0.12^{+0.14}_{-0.08}$	0.36	2.4	[4, 5]
J1319+0950	6.1330 ± 0.0007	$2.1^{+3.8}_{-1.4}$	2.7	$1.0^{\rm b}$	[4, 8]
J2054-0005	6.0391 ± 0.0001	$0.9^{+1.6}_{-0.6}$	1.1	$1.0^{\rm b}$	[4, 8]
J0055+0146	6.0060 ± 0.0008	$0.24^{+0.26}_{-0.14}$	0.38	1.2	[4, 5]
J2310+1855	6.0031 ± 0.0002	$2.8^{+5.1}_{-1.8}$	3.6	$1.0^{\rm b}$	[4, 8]
J1044-0125	5.7847 ± 0.0007	11^{+19}_{-7}	4.5	$0.35^{\rm a}$	[4, 8]
J0129-0035	5.7787 ± 0.0001	$0.17^{+0.31}_{-0.11}$	0.22	$1.0^{\rm b}$	[4, 8]
J0210-0456	6.438 ± 0.004	$0.08^{+0.055}_{-0.04}$	0.25	2.4	[5]
J2329-0301	6.417 ± 0.002	$0.25^{+0.04}_{-0.04}$	0.43	1.3	[5]
J0050+3445	6.253 ± 0.003	$2.6^{+0.5}_{-0.4}$	2.1	0.62	[5]
J0221-0802	6.161 ± 0.014	$0.70^{+0.75}_{-0.47}$	0.30	0.33	[5]
J1509-1749	6.121 ± 0.002	$3.0^{+0.3}_{-0.3}$	2.6	0.68	[5]
J2100-1715	6.087 ± 0.005	$0.94^{+0.29}_{-0.25}$	0.59	0.49	[5]
J1641+3755	6.047 ± 0.003	$0.24^{+0.10}_{-0.08}$	0.72	2.3	[5]
J0836+0054	5.810 ± 0.003	$9.3^{+1.6}_{-1.6}$	5.25	0.44	[6]
J1030+0524	6.309 ± 0.009	$3.6^{+0.9}_{-0.9}$	2.34	0.50	[6]
J1306+0356	6.016 ± 0.005	$3.2^{+0.6}_{-0.6}$	2.51	0.61	[6]
J1411+1217	5.927 ± 0.004	$1.3^{+0.3}_{-0.3}$	1.58	0.94	[6]
J1623+3112	6.247 ± 0.005	$1.5^{+0.3}_{-0.3}$	2.14	1.11	[6]
J1342+0928	7.5413 ± 0.0007	$0.78^{+0.33}_{-0.19}$	1.5	$1.5^{+0.5}_{-0.4}$	[7]

[a] We use the values of bolometric luminosity and black hole mass for the calculation of $L_{\rm bol}/L_{\rm Edd}$. [b] The Eddington accretion is assumed for the derivation of the BH masses. [1] Mazzucchelli et al. (2017) (their tables 5 and 8). For the quasar PSO J338+29, we recalculate the bolometric luminosity $L_{\rm bol}$ using their equation (13). [2] Mortlock et al. (2011). [3] Wu et al. (2015). [4] Gallerani et al. (2017) (their table 1). [5] Willott et al. (2010) (their table 2). [6] Jiang et al. (2007) (their tables 2 and 5). [7] Bañados et al. (2017). [8] Wang et al. (2013) (their table 3 for $L_{\rm bol}$).

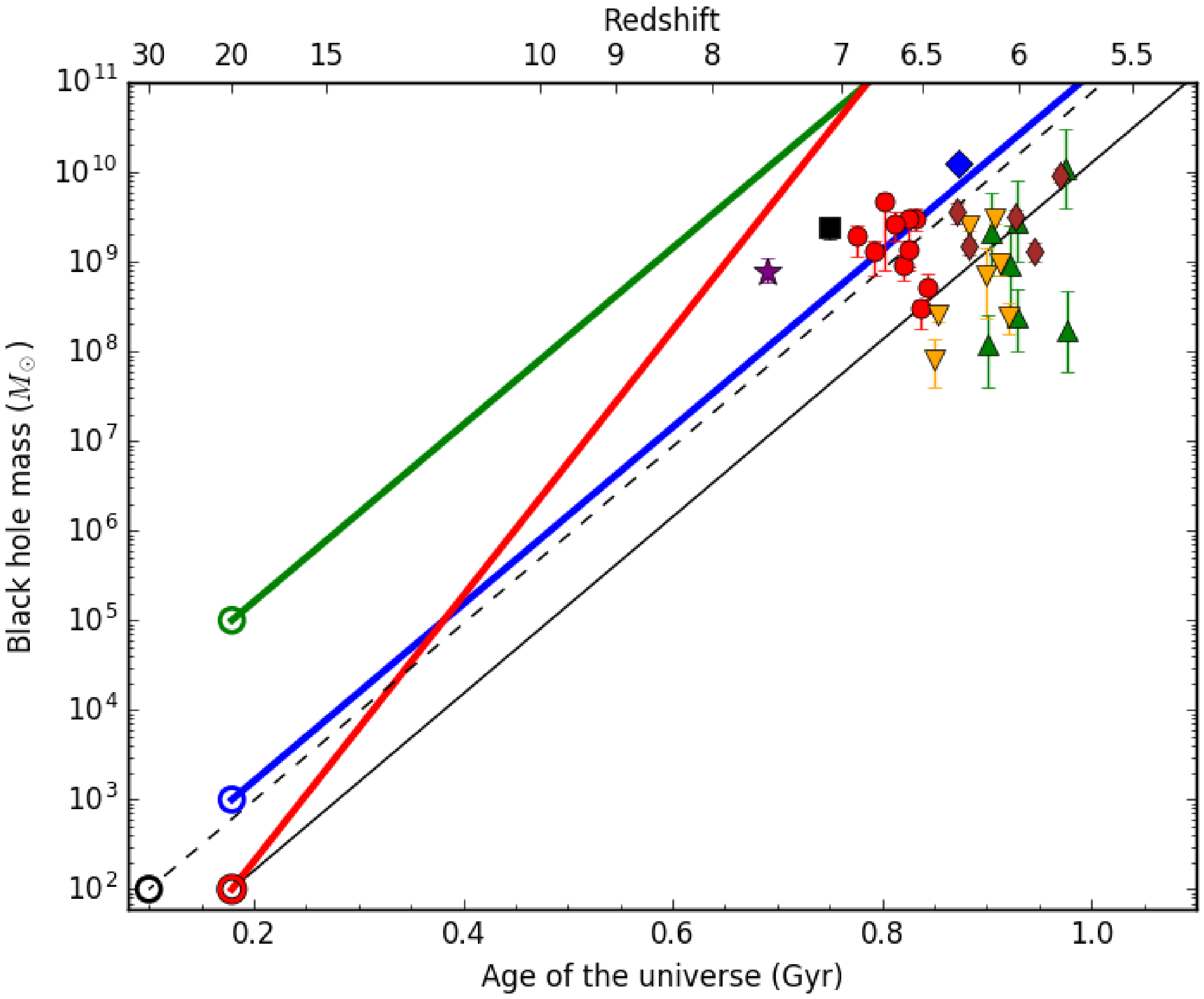

Fig. 1.1 Redshift versus mass of high-z quasars observed at $\gtrsim 6$. We use the estimates of redshift and BH mass from Mazzucchelli et al. (2017) (red circles and black square), Wu et al. (2015) (blue diamond), Gallerani et al. (2017) (green triangles), Willott et al. (2010) (orange down-pointing triangles), Jiang et al. (2007) (brown diamonds) and Bañados et al. (2017) (purple star). The black square represents the quasar discovered by (Mortlock et al. 2011). Evolutions of BH mass are also shown as lines from the initial seed BH mass depicted as open circles (see Section 1.2). The black solid and dashed lines depict evolutions of BH mass from $z = 20$ and 30 respectively, assuming the initial seed BH mass $M_{\rm seed} = 100$ $\rm M_\odot$ and the Eddington accretion rate, i.e., $L = L_{\rm Edd}$ in equation (1.4). The green and blue solid lines represent the mass growth from $z = 20$ with the larger seed BH mass $M_{\rm seed} = 10^5$ $\rm M_\odot$ and 1000 $\rm M_\odot$ respectively, assuming the Eddington accretion rate. The red solid line shows the mass growth from $z = 20$ with a super-Eddington accretion rate with $L = 1.5L_{\rm Edd}$ in equation (1.4) from $M_{\rm seed} = 100$ $\rm M_\odot$.

time scale. The Eddington luminostiy is

$$L_{\rm Edd} = \frac{4\pi G M \mu_{\rm e} m_{\rm p} c}{\sigma_{\rm T}}, \tag{1.2}$$

where $\mu_{\rm e}$ is mean molecular mass per an electron, $m_{\rm p}$ is the proton mass and $\sigma_{\rm T}$ is the Thompson scattering cross section. We can solve the equation (1.1) as

$$M_{\rm BH} = M_{\rm seed} \exp\left(\frac{t}{t_{\rm grow}}\right), \tag{1.3}$$

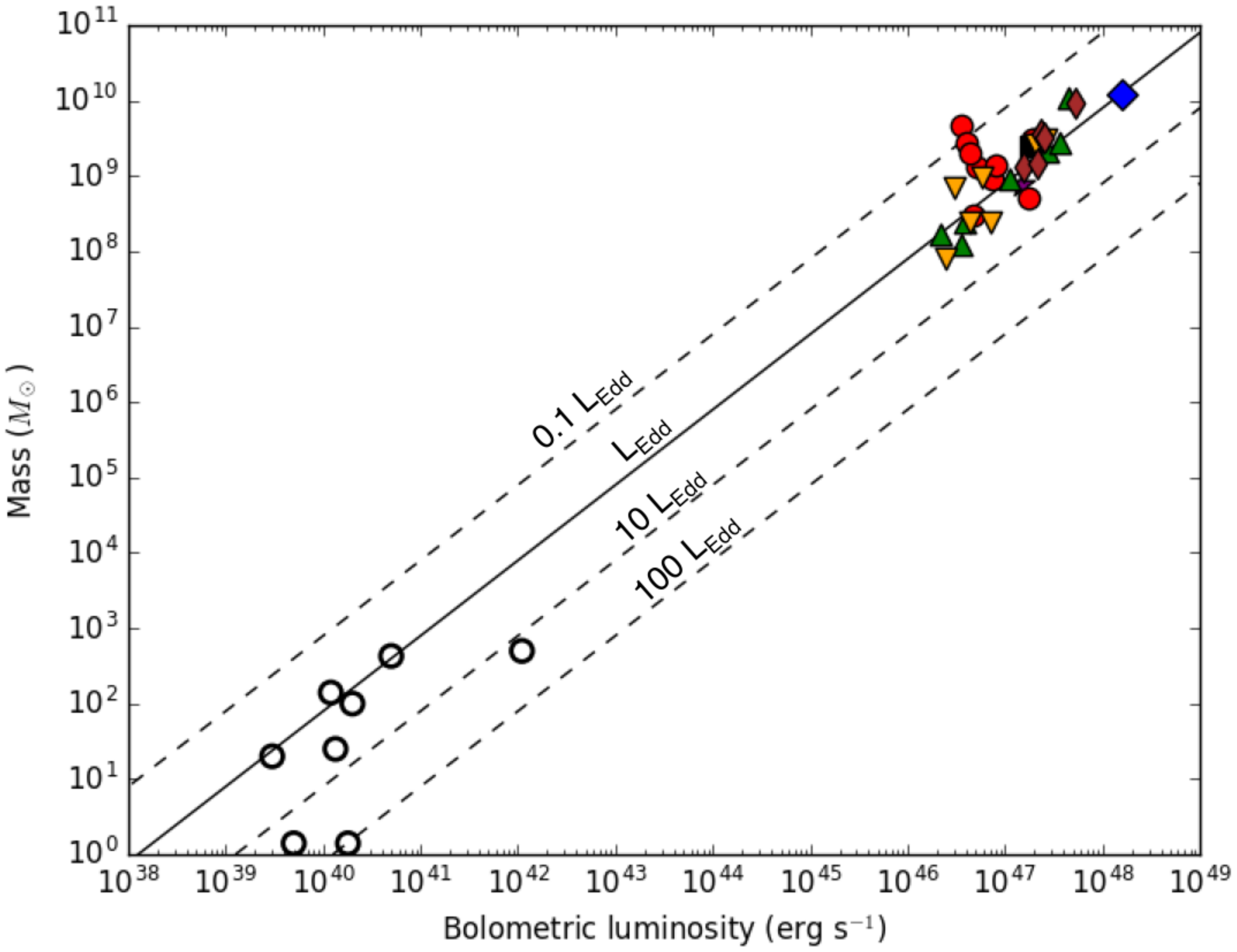

Fig. 1.2 Bolometric luminosity versus BH mass for the quasars in the early universe (Table 1.1, the colors and markers are the same as in Figure 1.1). The corresponding quantities for some ULXs are also shown by black open circles (Table 1.2). The lines denote the relation of mass-$fL_{\rm Edd}$, where $L_{\rm Edd}$ is the Eddington luminosity (equation 1.2) and $f = 0.1$, 1, 10 and 100.

Table 1.2 Some examples of ULXs.

Name	M ($\mathrm{M_\odot}$)	L ($10^{40}\,\mathrm{erg\,s^{-1}}$)	$L/L_{\rm Edd}$	References
Holmberg II X-1	> 25	$1.34^{\rm a}$	< 4.3	[1]
M 82 X-1	428 ± 105	$5^{\rm b}$	0.8 ± 0.2	[2]
M 82 X-2	~ 1.4	$1.8^{\rm b}$	~ 100	[3]
NGC 7793 P13	~ 1.4	$0.2 - 0.5^{\rm b}$	~ 30	[4]
M 101 ULX-1	$20 - 40$	$0.3^{\rm a}$	~ 1	[5]
NGC 1313 X-1/X-2	> 100	$2.0/0.66^{\rm b}$	$< 1.6/ < 0.52$	[6]
M74 X-1	~ 140	$< 1.2^{\rm b}$	< 0.7	[7]
ESO 243-49	> 500	$< 110^{\rm b}$	< 20	[8]

[a] Bolometric luminosity. [b] X-ray luminosity. [1] Cseh et al. (2014). [2] Pasham, Strohmayer & Mushotzky (2014). [3] Bachetti et al. (2014). [4] Israel et al. (2017). [5] Liu et al. (2013). [6] Miller et al. (2003). [7] Krauss et al. (2005). [8] Farrell et al. (2009).

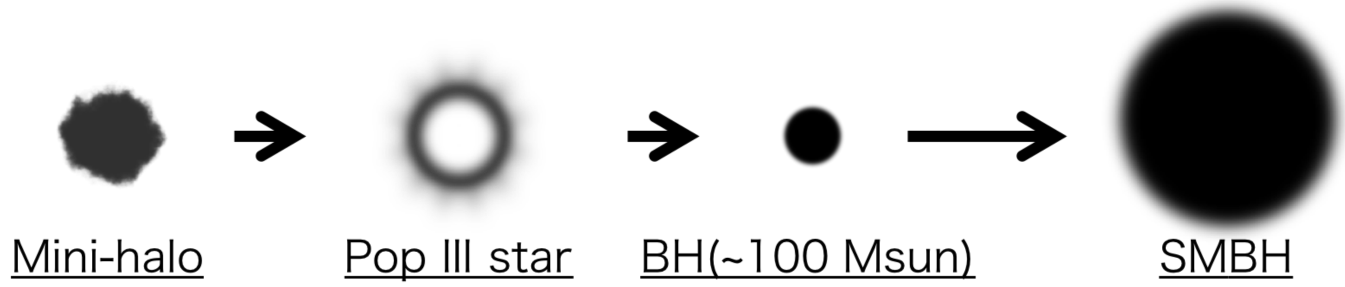

Fig. 1.3 Pop III BH model for the formation of the high-redshift SMBHs.

Table 1.3 A mini-halo versus an atomic-cooling halo.

Nomenclature	Redshift	$M_{\rm vir}$ ($\rm M_\odot$)	Components	Coolants	T (K)	$\dot{M}$ ($M_\odot\,{\rm yr}^{-1}$)
Mini-halo	$\gtrsim 20$	$\sim 10^{5-6}$	primordial species including $\rm H_2$	$\rm H_2$	~ 200	$\sim 10^{-4} - 10^{-3}$
Atomic-cooling (AC) halo	$\gtrsim 10$	$\sim 10^{7-8}$	primordial species without $\rm H_2$	H	$\sim 10^4$	$\sim 0.1 - 1$

Column 2: typical redshift when the halo forms or becomes unstable and commences gas collapse due to Jeans instability with gas density $\lesssim 1\,{\rm cm}^{-3}$; column 3: virial mass of the halo at the halo formation; column 4: components of the halo at the halo formation; column 5: main coolants during the gas collapse; column 6: typical gas temperature during the gas collapse; column 7: accretion rates which would be realized after protostellar formation at density $\sim 10^{21}\,{\rm cm}^{-3}$.

where $M_{\rm seed}$ is the initial seed BH mass and $t_{\rm grow}$ is the growth time scale. The latter quantity is

$$t_{\rm grow} = \left(\frac{\epsilon}{1-\epsilon}\right)\left(\frac{L_{\rm Edd}}{L}\right) t_{\rm Edd} = 4.4 \times 10^7 \ {\rm yr} \left(\frac{L_{\rm Edd}}{L}\right), \tag{1.4}$$

where we use radiative efficiency $\epsilon = 0.1$, typical for local quasars (Soltan 1982, Yu & Tremaine 2002), and $\mu_{\rm e} = 1.14$, expected in fully ionized primordial gas with the hydrogen and helium mass fractions of $X = 0.75$ and $Y = 0.25$.

As in Figure 1.3, possible seed BHs are remnant BHs of Population III (Pop III) stars (Madau & Rees 2001), which have typical stellar mass of ~ 100 $\rm M_\odot$ (Hirano et al. 2014, Susa, Hasegawa & Tominaga 2014) and can leave the BHs with mass ~ 100 $\rm M_\odot$ after their lifetimes (see figure 2 of Heger & Woosley 2002). The seed BH of ~ 100 $\rm M_\odot$ can just barely attain mass of $\sim 10^9$ $\rm M_\odot$ by $z \simeq 6$ if we assume the Eddington accretion rate, as is depicted by the black solid line of Figure 1.1. Recent studies, however, suggest difficulties in this model. For example, radiation feedback from a BH accretion disk readily suppresses a gas supply from an intergalactic medium, resulting in decrease of the accretion rate far below the Eddington values (Alvarez, Wise & Abel 2009, Jeon et al. 2012). The growth time of the BH then becomes much longer than the age of the universe at $z \sim 6$.

To circumvent the difficulties in the Pop III BH model, three models which accelerate the formation of the high-redshift SMBHs have been suggested: the direct collapse model, the super-Eddington model and the runaway stellar collision model. In Figure 1.4, we show a schematic picture which depicts these three models.

In Tables 1.3 and 1.4, we briefly summarize the nomenclatures used in this thesis.

1.2.1 Supermassive stars and direct collapse massive seed BHs

One alternative model to ease the growth delay problem is so-called direct collapse model. In the model, SMBHs are assumed to be built from larger seed BHs of $M_{\rm BH} \sim 10^5\,\rm M_\odot$ which are remnants

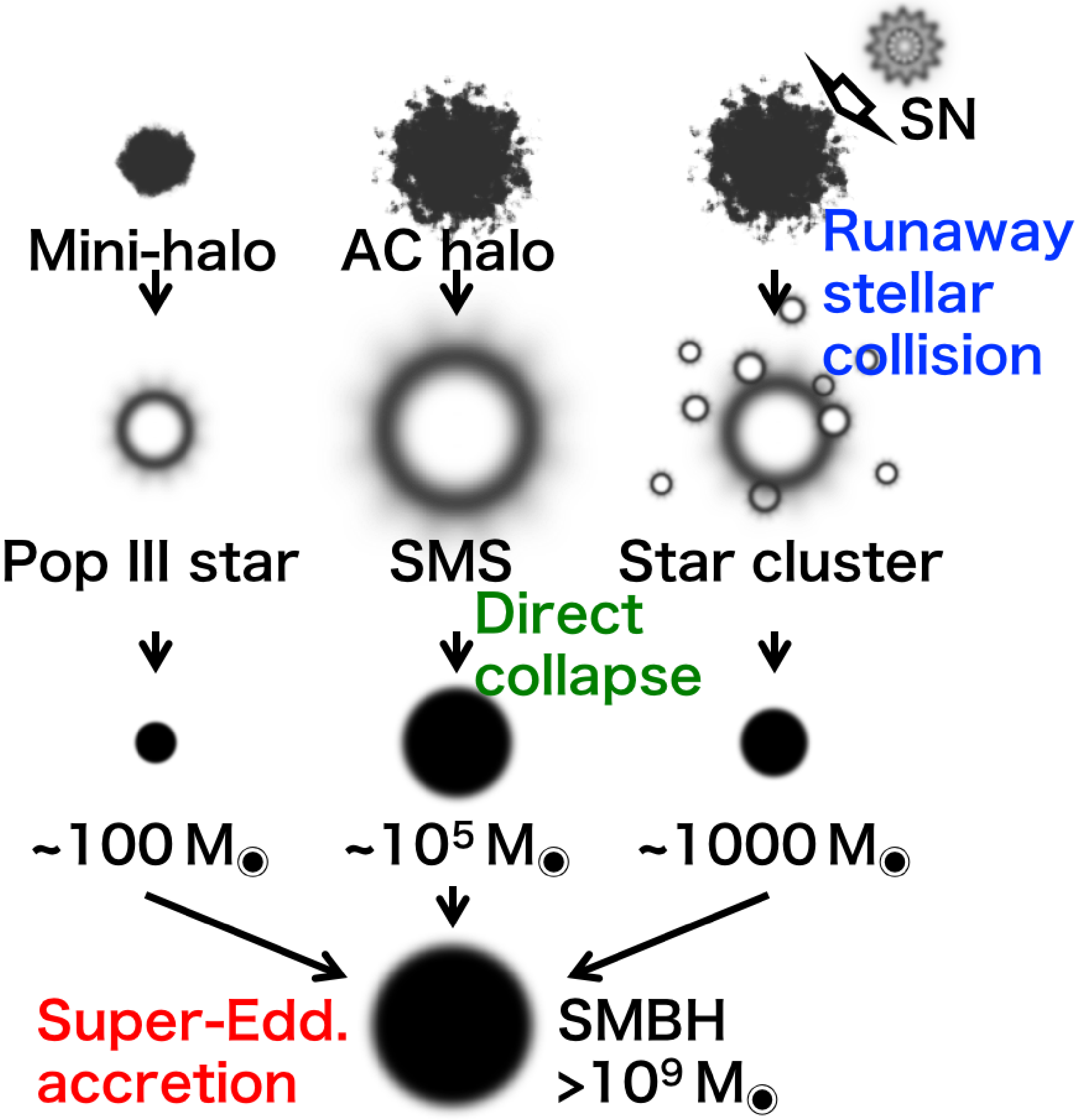

Fig. 1.4 Three SMBH formation models which accelerate the formation of SMBHs in the early universe: the direct collapse model, the super-Eddington model and the runaway stellar collision model.

Table 1.4 A Pop III star versus a supermassive star.

Nomenclature	Formation site	M_* ($\mathrm{M}_\odot$)
(Normal) Pop III star	Mini-halo	~ 100
Supermassive star (SMS)	AC halo	$\sim 10^5$

after gravitational collapse of supermassive stars (SMSs) with similar masses (Shibata & Shapiro 2002, Bromm & Loeb 2003, Reisswig et al. 2013). The growth time of the BH is significantly shortened in this case. For instance, a $\sim 10^5\,\mathrm{M}_\odot$ seed BH will easily increase its mass and becomes a $\gtrsim 10^9\,\mathrm{M}_\odot$ SMBH via accretion at the Eddington rate (see the solid green line of Figure 1.1). With reduced accretion rates due to, e.g., radiation feedback from a BH-disk system, an SMBH of $\sim 10^9\,\mathrm{M}_\odot$ can still form at $\simeq 6$ if the average accretion rate is higher than ~ 50 per cent of the Eddington accretion rate. Indeed, cosmological simulations show that efficient cold accretion flows allow such high accretion rates in the epoch of the first galaxy formation (Di Matteo et al. 2012).

In the direct collapse model, a critical assumption is that sufficiently massive stars form in a gas cloud. Specifically, SMSs are considered to form in the so-called atomic-cooling halos of virial temperature $T_{\rm vir} \sim 10^4\,\mathrm{K}$ (Inayoshi & Omukai 2012, Agarwal et al. 2014, Visbal, Haiman & Bryan 2014). When molecular hydrogen cooling is suppressed in these massive primordial halos due to strong ultraviolet radiation, gas clouds gravitationally collapses mainly with atomic hydrogen cooling, almost isothermally at $T \simeq 8000\,\mathrm{K}$ (Omukai 2001). An embryonic protostar eventually forms and starts to grow by gas accretion from a surrounding envelope (Inayoshi & Haiman 2014, Van Borm et al. 2014), in analogy with normal Pop III star formation (Yoshida, Omukai & Hernquist 2008). The accretion rate at the accretion phase has the well-known temperature dependence of

$$\dot{M}_* \sim \frac{c_{\rm s}^3}{G} \sim 0.2 \left(\frac{T_{\rm vir}}{10^4\,\mathrm{K}} \right)^{3/2} M_\odot\,\mathrm{yr}^{-1}, \tag{1.5}$$

wherein $c_{\rm s}$ is a sound speed of gas and G is the gravitational constant. Due to the higher gas temperature during the collapse stage, the accretion rate is significantly higher than that in normal Pop III cases. If such a high mass accretion rate is maintained for $\sim 1\,\mathrm{Myr}$, which is the lifetime of massive stars, SMSs of $10^5 - 10^6\,\mathrm{M}_\odot$ will form and finally provide massive BH seeds after their deaths.

A possible hurdle for the growth of SMSs by rapid gas accretion is radiative feedback from the central massive protostar. Even for a normal Pop III star of $\sim 100\,\mathrm{M}_\odot$ forming by accretion, stellar UV radiation becomes sufficiently strong to create an H II region which dynamically expands through the accretion envelope (McKee & Tan 2008). The H II expansion eventually leads to halting the gas accretion; final stellar mass is determined by this mechanism (Hosokawa et al. 2011). It is expected that, for the case of SMS formation, similar or even stronger UV radiation feedback might largely reduce or even halt the gas accretion. The feedback could occur since an SMS would emit significant amounts of photons with stellar luminosity being nearly at the Eddington value, which is proportional to stellar mass.

Strength of the stellar radiation feedback is dependent critically on the ionizing photon emissivity from primordial protostars, which is derived considering their evolution during accretion. For normal Pop III cases of average accretion rates $\sim 10^{-3}\,M_\odot\,\mathrm{yr}^{-1}$, a radius of an accreting protostar is large during the early evolution but eventually becomes small with contraction to the zero-age main sequence (ZAMS) for $M_* \sim 100\,\mathrm{M}_\odot$ (Omukai & Palla 2003). During the contraction of the star, its ionizing photon emissivity rises and UV radiative feedback becomes effective.

By contrast, protostellar evolution with very rapid accretion rates $\dot{M}_* \gtrsim \dot{M}_{*,\rm cr} = 4 \times 10^{-2}\,M_\odot\,\mathrm{yr}^{-1}$ expected in the direct collapse model is qualitatively different from that in the Pop III cases. At the high accretion rates, a protostar continues to expand and does not contract even after the star becomes as massive as $\sim 100\,\mathrm{M}_\odot$ (Hosokawa, Omukai & Yorke 2012). The radius of the star reaches $\sim 10^4\,R_\odot$ for $M_* \gtrsim 10^3\,\mathrm{M}_\odot$ (Hosokawa et al. 2013, Schleicher et al. 2013). Effective temperature of such a 'supergiant protostar' is as low as $T_{\rm eff} \simeq 5000\,\mathrm{K}$ and the ionizing photon emissivity for

$M_* \lesssim 10^4\,\mathrm{M}_\odot$ remains only $\lesssim 10^{45}\,\mathrm{s}^{-1}$, which is several orders of magnitude smaller than for main-sequence SMSs. The resulting UV feedback would be too weak to stop the mass accretion. For giant stars, mass loss can be induced due to a pulsational instability, but expected mass-loss rates are much lower than the rapid mass growth rates via accretion (Inayoshi, Hosokawa & Omukai 2013). Thus, the high mass accretion rate is expected to be maintained and SMSs of mass $\gtrsim 10^5\,\mathrm{M}_\odot$ will ultimately form.

In the previous studies, only constant accretion rates are considered. In more realistic situations, however, the gas accretion on to a growing SMS would be dynamic with highly time-variable accretion histories. For normal Pop III cases, for example, a circumstellar accretion disk becomes gravitationally unstable and fragments (Stacy, Greif & Bromm 2010, Greif et al. 2011). Such fragments migrate inward within the disk and accrete on to the star (Greif et al. 2012), resulting in a drastic increase of the accretion rate which is so-called burst accretion (Vorobyov, DeSouza & Basu 2013). In this case, the accretion history has two phases: one is the burst phase with $\dot{M}_* \sim 0.1\,M_\odot\,\mathrm{yr}^{-1}$ and the other is a quiescent phase with $\dot{M}_* \sim 10^{-4}\,M_\odot\,\mathrm{yr}^{-1}$, whose time spans are $\lesssim 10^2$ and $\sim 10^3 - 10^4\,\mathrm{yr}$ respectively. This episodic accretion is also expected to occur during the SMS formation via disk gas accretion (Inayoshi & Haiman 2014). In fact, recent high-resolution simulations report signatures of the disk fragmentation within atomic-cooling halos (Regan, Johansson & Wise 2014, Becerra et al. 2015).

1.2.2 Super-Eddington mass accretion on to seed BHs

One of the other models to avoid the growth delay in the Pop III BH model is the super-Eddington accretion model, in which seed BHs grow via very rapid super-Eddington accretion flows. How are such super-Eddington accretion flows achieved? Usually, when the BH is fed by sufficiently strong gas flows and the emitting luminosity increases, radiative feedback is likely to disturb gas dynamics. Such radiation feedback is caused by radiation pressure force and radiation heating.

Radiation force is crucially important in the vicinity of the BH horizon since the gas is highly opaque to electron scattering. Specifically, if the luminosity approaches the Eddington luminosity (equation 1.2), the radiation force becomes comparable to the BH gravity, limiting the accretion rate to the Eddington rate. To overcome the limit of the Eddington accretion, 'photon trapping' (Katz 1977, Begelman 1978) during BH growth would be helpful. The photon trapping becomes effective when radiation within an optically thick flow is advected inwards via efficient electron scattering faster than the radiation can escape by radiative diffusion. The emergent luminosity is then limited, and it is prevented from exceeding the Eddington luminosity for a spherical symmetric flow case (Begelman 1979). We can estimate the characteristic 'trapping radius' as

$$R_{\mathrm{tr}} \equiv \frac{\kappa_{\mathrm{es}}\dot{M}}{4\pi c}, \tag{1.6}$$

outside which photons escape and contribute to the emergent luminosity. Using the radius, we can see that the maximum luminosity released by gravitational energy is limited to the Eddington luminosity as $\simeq GM_{\mathrm{BH}}\dot{M}/R_{\mathrm{tr}} \sim L_{\mathrm{Edd}}$.

Considering the photon trapping effect which reduces radiation force, previous studies have shown that the super-Eddington accretion is realized with very rapid gas flows. Numerical simulations have examined rapid accretion with $\dot{M} \gg L_{\mathrm{Edd}}/c^2$ and showed that the high accretion rates are possible in a disk-like configuration, with which radiation escapes vertically (Ohsuga et al. 2005, Fragile, Olejar & Anninos 2014, Jiang, Stone & Davis 2014, McKinney et al. 2014, Sądowski et al. 2014, Sądowski & Narayan 2016). In semi-analytical models, the possibility of such rapid growth of BHs in the early universe is also suggested (Volonteri & Rees 2005, Alexander & Natarajan 2014, Madau, Haardt & Dotti 2014, Volonteri, Silk & Dubus 2015). Analytical studies also support rapid growth by gas accretion at a super-Eddington rate (Pacucci, Volonteri & Ferrara 2015). A recent work of Pezzulli, Valiante & Schneider (2016) shows that a very high accretion rate of $\gtrsim 10^3\,L_{\rm Edd}/c^2$ is maintained at $z > 10$, even if BH feedback effect is included.

Radiation heating, on the other hand, can suppresses gas inflows from larger scales wherein gas is not bounded by BH gravity. By the radiation heating effect, the accretion behavior can become episodic and the mean accretion rate is limited to $\lesssim 10\,L_{\rm Edd}/c^2$ (Ciotti & Ostriker 2001, Milosavljević, Couch & Bromm 2009, Park & Ricotti 2011, 2012, Park et al. 2016).

In order to address the issue of BH accretion flows more correctly, we need to consider a self-consistent solution of the flows from large scales, wherein the mass accretion begins, to small scales, wherein photon trapping diminishes the emergent luminosity. Recently, Inayoshi, Haiman & Ostriker (2016: hereafter IHO16) found a self-consistent spherically symmetric steady solution of BH accretion flows at a rate of $\gtrsim 5000 L_{\rm Edd}/c^2$ ('hyper-Eddington accretion') when the condition is satisfied as

$$\left(\frac{n_\infty}{10^5\,{\rm cm^{-3}}}\right) \gtrsim \left(\frac{M_{\rm BH}}{10^4\,{\rm M_\odot}}\right)^{-1} \left(\frac{T_\infty}{10^4\,{\rm K}}\right)^{3/2}, \tag{1.7}$$

in which n_∞ and T_∞ are density and temperature of ambient gas. They showed that this condition corresponds to a H II region, generated by ionizing radiation emanating from a photosphere, being smaller than the Bondi radius. In this case, the solution consists of a radiation-dominated core, whereby photon trapping due to electron scattering is effective, and an accreting envelope that follows an isothermal Bondi profile with $T \simeq 8000\,{\rm K}$. When the photon trapping suppresses luminosity emanating from the photosphere to $\lesssim L_{\rm Edd}$, radiation from the central region does not halt the gas accretion from larger scales. In fact, the H II region size remains much smaller than the Bondi radius, resulting in a high inflow rate which is unimpeded by radiation feedback.

In IHO16, they adopted a model which assumed that photon trapping is effective, and that luminosity is limited to $L_{\rm Edd}$. This assumption is, however, not valid if a compact nuclear disk is produced by the accretion flow with non-zero angular momentum. From the disk, outflows or jets are potentially launched into polar regions (Ohsuga et al. 2005, McKinney et al. 2014, Sądowski et al. 2014). Also, in the polar regions, photon trapping is found less efficient than in spherically symmetric flows, with the vertical escape of radiation being facilitated by magnetic buoyancy (Jiang, Stone & Davis 2014). As a result, luminosity away from the disk place can largely exceed the Eddington luminosity.

1.2.3 Formation of massive stars and intermediate-mass BHs via runaway collision of stars in dense star clusters

There is still another mechanism to facilitate formation of massive BHs in the early universe. In some star clusters in the present-day Universe, it has been suggested that intermediate-mass BHs (IMBHs) lurk at the central regions. Such IMBHs, if they exist, can be remnants of very massive stars which could have formed via runaway stellar collisions in the clusters (Ebisuzaki et al. 2001, Vanbeveren et al. 2009, Devecchi et al. 2010, Katz, Sijacki & Haehnelt 2015). Omukai, Schneider & Haiman (2008) have discussed that dense star clusters, within which runaway collision can occur, are formed in atomic-cooling halos with a virial temperature of $\gtrsim 10^4\,{\rm K}$, which are enriched by metals (elements heavier than helium) through a supernova ejection of matter fused inside a star. They argue that a gas cloud with metallicity larger than $Z_{\rm cr} \sim 5 \times 10^{-6}\,Z_\odot$ can undergo dust-induced cooling and fragmentation, resulting in production of a star cluster. Devecchi et al. (2010) have investigated formation of very massive stars and BH seeds in star clusters considering a hierarchical galaxy formation model. They predict in their semi-analytic model that a BH mass density is as large as $\rho_{\rm seed} \sim 2000 - 4000\,{\rm M_\odot\,Mpc^{-3}}$ at $z \gtrsim 6$.

Formation of star clusters at high redshift has been also examined by numerical simulations (Boley et al. 2009, Trenti, Padoan & Jimenez 2015). Bromm & Clarke (2002) have performed Smoothed Particle Hydrodynamics (SPH) simulations of dwarf galaxy formation in the early universe and show that globular clusters with mass $\sim 10^5\,{\rm M_\odot}$ form in small-mass halos. Kimm et al. (2016) have studied formation of globular clusters at $z > 10$ by performing cosmological radiation-hydrodynamical simulations. They find that metal-cooling induced gas fragmentation drives formation of dense star clusters with mass $6 \times 10^5\,{\rm M_\odot}$ and a half-light radius $\lesssim 1\,{\rm pc}$ within about $10\,{\rm Myr}$.

Overall, the dense star cluster formation in the early universe is plausible. There are, however, few simulations to date which follow primordial star cluster evolution until the runaway stellar collisions occur and IMBHs form. Katz, Sijacki & Haehnelt (2015) have performed a cosmological simulation to examine the dynamical evolution of a star cluster which is formed in a metal-enriched mini-halo. Identifying the star cluster from the cosmological simulation and then performing direct N-body simulations, they show that the runaway stellar collisions occur in the cluster, where a very massive star of $\sim 300 - 1000\,{\rm M_\odot}$ is yielded. The massive stars would leave IMBHs after their lifetimes. The cluster model of Katz, Sijacki & Haehnelt (2015) provides promising IMBH formation channel in the early universe, but unfortunately their cluster model is based on only one specific mini-halo. Thus, it is still unclear how rare such IMBH formation at high redshift is.

1.3 Aim of this thesis

This thesis aims to study the three BH seed formation models which circumvent the BH growth delay (Section 1.2), namely, the direct collapse model, the super-Eddington accretion model and the runaway stellar collision model. Specifically, we adopt more realistic situations for each model than those in previous works in order to examine the validity of the models.

In Chapter 2, in the context of the direct collapse model, we work on the formation of SMSs via rapid gas accretion, in order to see whether UV feedback can be effective to halt the growth of the accreting SMS. In Hosokawa et al. (2013), they consider SMS evolution with constant high accretion rates $\gtrsim 0.1\,{\rm M_\odot}$ and show that the protostar becomes supergiant with a bloating, low temperature surface of $T_{\rm eff} \sim 5000\,{\rm K}$ and that UV feedback is ineffective. By contrast, we study the SMS evolution with a highly time-variable accretion history, expected for accretion through a gravitationally unstable disk, where fragments form by fragmentation and fall on to the central protostar causing accretion bursts. We use a stellar evolution code STELLAR which can solve basic equations of stellar evolution, treating nuclear reactions and convection within the star (Yorke & Bodenheimer 2008). The evolutions of the accreting SMSs are computed, assuming episodic accretion histories for which we use parameters to mimic the variable features of the accretion. We compare our results with those for the constant accretion case to examine the impact of the episodic accretion histories on the evolution of the SMSs. We also vary episodic accretion histories by changing values of the parameters and see the variation of the SMS evolution. Finally, the efficiency of UV feedback is discussed.

In Chapter 2, we assume rather idealized, parameterized episodic accretion histories with analytical functions. In Chapter 3, as the next step, we examine stellar evolution with more realistic accretion histories. We first perform a 2D hydrodynamical simulation using a grid-based code ZEUS-2D (Stone & Norman 1992) to follow the protostellar accretion, adopting a central sink cell to monitor the accretion history for the central protostar. A gravitationally unstable disk around a rapidly accreting SMS is analyzed, focusing on the properties of fragments and the difference from a disk forming around a Pop III star, as studied in Vorobyov, DeSouza & Basu (2013). We then compute stellar evolution using the obtained accretion history in a post-process manner. The UV feedback efficiency is again discussed.

In Chapter 4, we examine the impact of a high-luminosity central source of $L > L_{\rm Edd}$ on a very rapid, spherical accretion flow at large radii, using 1D radiation hydrodynamical simulations with a code ZEUS (Stone & Norman 1992), to see whether or not hyper-Eddington accretion can also occur as in IHO16. Because of the computational difficulty to follow the entire accretion regions, we only focus on the large scale regions where BH gravity is comparable to accreting gas pressure and do not resolve smaller scales where photon trapping is effective and photosphere is formed. In the ZEUS code, as well as the basic hydrodynamical equations, non-equilibrium chemical reactions of primordial gas and radiation transfer are solved. We model the analytical functions of luminosity coming from a central source, or, a nuclear accretion disk, which can emit a super-Eddington luminosity of $L \gtrsim L_{\rm Edd}$, with a parameter of the maximum luminosity. From the simulations, BH accretion histories are derived to see whether the transition to the hyper-Eddington accretion occurs. We also see the variation of the histories when adopting different values of the maximum luminosity. We then discuss the results to explain the behavior of the histories using analytical arguments and a simple numerical model.

In Chapter 5, we perform direct-tree hybrid N-body simulations to follow evolution of several dense star clusters, which are assumed to form in atomic-cooling halos identified in cosmological SPH simulations. In contrast to the work by Katz, Sijacki & Haehnelt (2015) who consider a cluster formed in a mini-halo and focus on one realization, we consider clusters formed in an atomic-cooling halo and focus on several realizations. In this work, we will examine if runaway stellar collisions and IMBH formation are prevalent in primordial star clusters forming in atomic-cooling halos. First, we perform the cosmological simulations using a code Gadget-2 (Springel 2005) which is updated by Hirano et al. (2014) to get several atomic-cooling halo data. Then, star cluster initial conditions for the N-body simulations are generated, assuming parameters relating to star formation efficiency, an initial mass function (IMF) and a virial ratio which is the ratio of kinetic energy to gravitational energy of the clusters. From the initial conditions, we perform the N-body simulations using a code BRIDGE (Fujii et al. 2007). We also investigate the dependence of the parameters for the star cluster generation on the results.

Chapter 2

Primordial supermassive star formation via episodic accretion: I. Controlled cases with model accretion histories

2.1 Overview

We study stellar evolution of supermassive stars (SMSs) growing by rapid mass accretion in atomic-cooling halos. We show the assumed physical conditions of the atomic-cooling halo in Table 1.3 where SMSs are supposed to be formed in contrast to normal Pop III star formation in mini-halos (see Table 1.4). Although constant accretion rates are often assumed in previous works, which is a rather idealized assumption, we here examine the impact of time-dependent mass accretion of repeating burst and quiescent phases which is expected to occur with a self-gravitating circumstellar disk. Our calculations show that protostars growing via episodic accretion can substantially contract in the quiescent phases, in contrast to the constant mass accretion case, whereby the star expands roughly monotonically. Accordingly, the stellar effective temperature and ionizing photon emissivity increase, which can trigger strong ionizing feedback and suppress the mass accretion. With a fixed duration of the quiescent phase $\Delta t_{\rm q}$, the contraction occurs in early evolutionary phases, i.e., when $M_* \lesssim 10^3\ {\rm M}_\odot$ with $\Delta t_{\rm q} \simeq 10^3$ yr. For later epochs and larger masses with the same $\Delta t_{\rm q}$, stellar contraction is negligible even during quiescent phases. In the case with larger $\Delta t_{\rm q}$, however, the star continues to contract in quiescent phases even for the higher stellar masses. We find that this stellar behavior is well understood by comparing the interval time between bursts $\Delta t_{\rm q}$ and the thermal time for a bloated surface layer. We conclude that the stellar radiation feedback becomes effective if $\Delta t_{\rm q} \gtrsim 10^3$ yr. Such a long interval time is possible in an accretion disk forming in the direct collapse model.

2.2 Numerical method and modeling of episodic accretion

2.2.1 Stellar evolution code for accreting stars

We use the stellar evolution code STELLAR developed by Yorke & Bodenheimer (2008) to calculate evolution of accreting massive protostars. The basic equations are

$$\frac{\partial r}{\partial m} = \frac{1}{4\pi r^2 \rho}\ , \tag{2.1}$$

Table 2.1 Models of episodic accretion. The average accretion rates are 0.1 $M_\odot\,\mathrm{yr}^{-1}$. The table is taken from Sakurai et al. (2015).

Model	A	B	C	D
Duration of the burst phase Δt_b (yr)	25	50	100	500
Duration of the quiescent phase Δt_q (yr)	270	540	1080	5400
Accretion rate in the burst phase $\dot{M}_{*,\mathrm{b}}$ ($M_\odot\,\mathrm{yr}^{-1}$)	1	1	1	1
Accretion rate in the quiescent phase $\dot{M}_{*,\mathrm{q}}$ ($M_\odot\,\mathrm{yr}^{-1}$)	10^{-3}	10^{-3}	10^{-3}	10^{-3}
Transition time Δt_t (yr)	50	100	200	1000
Radiative efficiency η	0.1	0.1	0.1	0.01

$$\frac{\partial P}{\partial m} = -\frac{Gm}{4\pi r^4} \ , \tag{2.2}$$

$$\frac{\partial l}{\partial m} = E_\mathrm{nuc} - c_P \frac{\partial T}{\partial t} + \frac{\delta}{\rho}\frac{\partial P}{\partial t} \tag{2.3}$$

$$\frac{\partial T}{\partial m} = -\frac{GmT}{4\pi r^4 P}\nabla, \tag{2.4}$$

where m is the enclosed mass, r is the radial distance from the center, ρ is the density, P is the total pressure, l is the net energy flux, E_nuc is the net energy generation rate by nuclear fusion, c_P is the specific heat at constant pressure, T is the temperature, $\delta \equiv (\partial \ln \rho / \partial \ln T)_\mathrm{P}$ and $\nabla \equiv \partial \ln T / \partial \ln P$ is the temperature gradient. The temperature gradient ∇ is computed using the mixing-length theory for convective regions (see e.g., Kippenhahn, Weigert & Weiss 2012). The nuclear reactions of hydrogen and helium burning are included in the rate E_nuc.

We assume hydrostatic equilibrium in equation (2.2) and omit the inertial term. The assumption is valid since the dynamical time in the stellar interior is much shorter than the duration of temporal change in accretion rates $\sim$ 10 yr (see Δt_t in Table 2.1). We retain the time derivatives in equation (2.3) and allow deviation from thermal equilibrium.

Mass accretion onto a stellar surface is included in the code by adding mass $\dot{M}\Delta t$ to the outermost grid in each time step. We assume that the accreting gas is thermally adjusted to the atmosphere before accretion, e.g., when slowly orbiting in a circumstellar disk. In this case the physical quantities of newly accreting gas are the same as in the stellar atmosphere. Note that the gas can actually bring additional energy which comes from released gravitational energy into the stellar surface region. We treat the effect by adding the advected energy to the stellar luminosity. The advected energy $L_{*,\mathrm{acc}}$ is expressed using a parameter η as the fraction of released gravitational energy,

$$L_{*,\mathrm{acc}} = \eta \frac{GM_* \dot{M}_*}{R_*}. \tag{2.5}$$

The adopted values of η are summarized in Table 2.1. As explained in Hosokawa et al. (2013) the stellar evolution is not changed by varying η for $M_* \gtrsim 100$ $\mathrm{M}_\odot$.

The initial stellar structure is constructed by solving the Lane-Emden equation with a polytropic index of $n = 1.5$ which means that the star is initially fully convective. The initial model has mass 2 $\mathrm{M}_\odot$ and a radius 25 $R_\odot$. The choice of the initial model is rather arbitrary, but the subsequent stellar evolution is insensitive to the initial condition for $M_* \gtrsim 100$ $\mathrm{M}_\odot$. We assume that the composition of the initial star and the accreting material is $X = 0.72$ and $Y = 0.28$.

2.2.2 Modeling of episodic accretion

Hydrodynamical simulations of a gravitationally unstable disk show that the accretion rate becomes episodic repeating alternately bursty and quiescent phases. For example, a burst occurs when a fragment emerging by gravitational instability migrates toward the central protostar to be accreted (Vorobyov, DeSouza & Basu 2013). Such a burst is usually followed by a quiescent phase at which the accretion rate becomes moderate. Another burst is triggered when another fragment forming in the gravitationally unstable disk again falls on to the star. The tendency of the burst accretion will continue while the disk self-gravity is effective by mass growth of the disk from a surrounding envelope.

We model episodic accretion histories using parameters. The burst and quiescent modes of the accretion are characterized by constant accretion rates $\dot{M}_{*,\mathrm{b}}$ and $\dot{M}_{*,\mathrm{q}}$, respectively. The durations of these phases are set by Δt_{b} and Δt_{q}. We also assume that the transition time between bursty and quiescent phases Δt_{t} is finite. The accretion rate during the transition phase is determined by linear interpolation.

We examine four different episodic accretion models with different sets of the parameters as listed in Table 2.1. The values are chosen so that the average accretion rates become $0.1\ M_{\odot}\,\mathrm{yr}^{-1}$ which is an expected value for the direct collapse model. For the other parameters, typical values are inferred in the analytical and numerical studies. Hydrodynamical simulations suggest that the durations of burst and quiescent phases are $10\ \mathrm{yr} \lesssim \Delta t_{\mathrm{b}} \lesssim 200\ \mathrm{yr}$ and $\Delta t_{\mathrm{q}} \lesssim 10^4\ \mathrm{yr}$ respectively, though these values are for normal Pop III star formation cases (e.g., DeSouza & Basu 2015, Vorobyov, DeSouza & Basu 2013). An analytical arguments of Inayoshi & Haiman (2014) also suggests $\Delta t_{\mathrm{q}} \lesssim 10^4$ yr for SMS formation cases (see their figure 2). As to values of $\dot{M}_{*,\mathrm{b}}$ and $\dot{M}_{*,\mathrm{q}}$, the numerical simulations usually show that the ratio of the two accretion rates $\dot{M}_{*,\mathrm{b}}/\dot{M}_{*,\mathrm{q}} \sim 10^3 - 10^4$. Thus we choose the values $\dot{M}_{*,\mathrm{b}} = 1\ M_{\odot}\,\mathrm{yr}^{-1}$ and $\dot{M}_{*,\mathrm{q}} = 10^{-3}\ M_{\odot}\,\mathrm{yr}^{-1}$ so that the average rate becomes $0.1\ M_{\odot}\,\mathrm{yr}^{-1}$. Note that the latter value is below the critical accretion rate $\dot{M}_{*,\mathrm{cr}} \sim 0.04\ M_{\odot}\,\mathrm{yr}^{-1}$. The transition time Δt_{t} is expected to be comparable to Δt_{b} as is seen in the numerical simulations. We assume finite transition times with $\Delta t_{\mathrm{b}} = 2\Delta t_{\mathrm{t}} < \Delta t_{\mathrm{q}}$, where the specific value is chosen to achieve numerical stability. We have checked that the effect of varying Δt_{t} by a factor of a few on the results is small.

We compare the results of the four models with the same mean accretion rate $0.1\ M_{\odot}\,\mathrm{yr}^{-1}$. We regard the Model C in Table 2.1 as a fiducial case (Section 2.3.2.1). The evolutionary calculations are commenced at burst phases.

2.3 Results

2.3.1 Evolution by constant accretion rates

We briefly describe the cases with constant accretion rates to compare to episodic accretion cases.

2.3.1.1 Normal Pop III star formation case with $10^{-3}\ M_{\odot}\,\mathrm{yr}^{-1}$

In the typical case of an accretion rate $10^{-3}\ M_{\odot}\,\mathrm{yr}^{-1}$, a protostar grow with several distinct evolutionary stages. To understand the behavior of the stellar evolution the two time scales are useful (Stahler, Palla & Salpeter 1986, Omukai & Palla 2003, Hosokawa & Omukai 2009a): the Kelvin-Helmholtz (KH) time scale

$$t_{\mathrm{KH}} = \frac{GM_*^2}{R_* L_*}, \tag{2.6}$$

which is the thermal time over which the gravitational energy is released by radiation, and the accretion time scale

$$t_{\rm acc} = \frac{M_*}{\dot{M}_*}, \tag{2.7}$$

which is the characteristic stellar growth time. In the early evolutionary phases of $M_* \lesssim 5$ $\mathrm{M}_\odot$, the star evolves adiabatically with $t_{\rm acc} < t_{\rm KH}$. As the star grows by mass accretion and the stellar luminosity L_* becomes larger, the KH time scale shortens. The luminosity increases because the opacity deep in the star decreases as the temperature increases according to Kramers' law ($\kappa \propto \rho T^{-3.5}$). With the decrease of the opacity, the heat accumulated in the inner region gradually escapes outward by radiation energy transport. The KH time finally becomes shorter than the accretion time and the protostar begins to contract losing more energy away from the surface by radiation. The KH contraction phase starts when $M_* \gtrsim 8$ $\mathrm{M}_\odot$ for the case of $\dot{M}_* = 10^{-3}$ $M_\odot\,\mathrm{yr}^{-1}$, which can be seen in Figure 2.1. The stellar internal temperature rises during the KH contraction phase, and eventually hydrogen burning commences at the center when $M_* \simeq 40$ $\mathrm{M}_\odot$. After this time, the evolution of the stellar radius traces the mass-radius relation of a ZAMS star.

Figure 2.1 shows that the ionizing photon emissivity rapidly rises during the KH contraction. Before the contraction, the emissivity is only $\sim 10^{37}$ s^{-1}. As the star contracts and the surface temperature increases, the emissivity quickly rises to $\gtrsim 10^{49}$ s^{-1}. With the large amount of emitting UV photons, radiation hydrodynamic simulations show that the radiation feedback is effective in the late KH contraction stage and finally suppresses the mass accretion (e.g., Hosokawa et al. 2011).

2.3.1.2 Direct collapse case with 0.1 $M_\odot\,\mathrm{yr}^{-1}$

We consider evolution of a protostar with the high constant accretion rate of 0.1 $M_\odot\,\mathrm{yr}^{-1}$. Unlike the normal Pop III star formation case of 10^{-3} $M_\odot\,\mathrm{yr}^{-1}$, the protostar does not experience KH contraction (see the black dashed lines in Figure 2.1). Instead, the overall evolution is that the star continues to expand nearly monotonically as the mass increases.

The Figure 2.2 shows that the time scale inversion explained in Section 2.3.1.1 occurs at $M_* \simeq 22$ $\mathrm{M}_\odot$ ($t \simeq 200$ yr) in this case. The star evolves adiabatically before this point. In the adiabatic epoch, the stellar radius at a given mass is larger than for 10^{-3} $M_\odot\,\mathrm{yr}^{-1}$ since the rapid accretion of 0.1 $M_\odot\,\mathrm{yr}^{-1}$ enhances average entropy in the inner region of the star. Unlike the normal Pop III case, the protostar continues to expand even when $t_{\rm KH} < t_{\rm acc}$, which at a glance is counterintuitive: with the time scale imbalance, a star normally radiates internal energy through the surface and contracts. Actually, for this bloating phase most of the stellar interior contracts, while only the surface layer with newly accreting gas inflates due to absorption of the heat flux coming from the contracting inner region (Hosokawa, Omukai & Yorke 2012). Specifically, though the bloating surface layer contains a small fraction of the total stellar mass, the opacity at the layer is large due to H^- bound-free absorption. The opacity of H^- has a very strong temperature dependence which makes the stellar effective temperature locked at a constant value of $\simeq 5000$ K as in the case of red giants. Using $T_{\rm eff} \simeq 5000$ K and $L_* = 4\pi R_*^2 \sigma_{\rm SB} T_{\rm eff}^4 \simeq L_{\rm Edd}$ where $\sigma_{\rm SB}$ is the Stefan-Boltzmann constant and $L_{\rm Edd}$ is the Eddington luminosity, we get the mass-radius relation during the bloating phase

$$R_* \simeq 2.4 \times 10^3 \; R_\odot \left(\frac{M_*}{100 \; \mathrm{M}_\odot} \right)^{1/2}, \tag{2.8}$$

which is consistent with the numerical results (Hosokawa et al. 2013).

The evolution of ionizing photon emissivity is also different to the case of 10^{-3} $M_\odot\,\mathrm{yr}^{-1}$. Even when $M_* \gtrsim 100$ $\mathrm{M}_\odot$, the emissivity is very small because of the low surface temperature of the

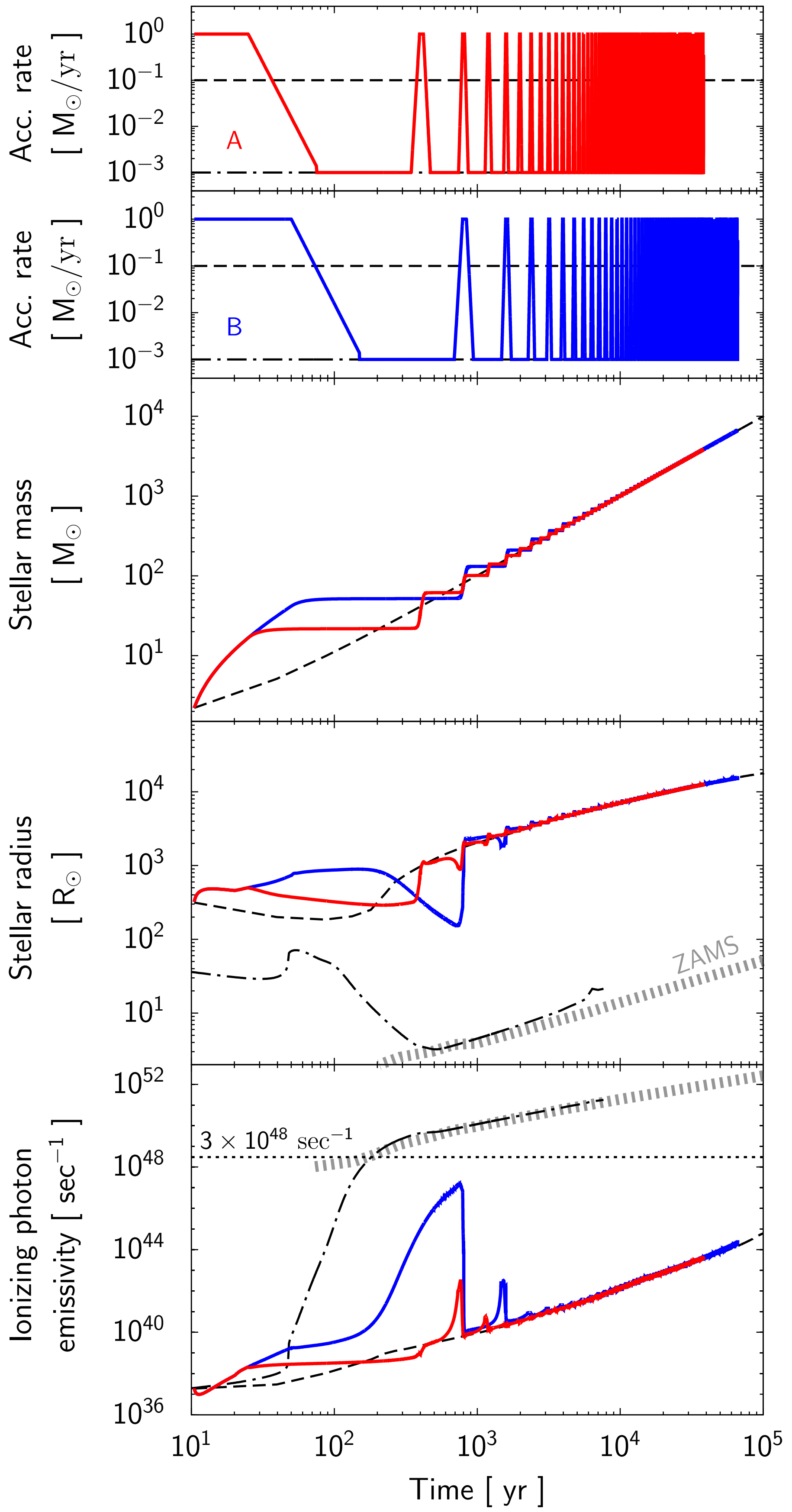

Fig. 2.1 Evolution of the accretion rates (top two panels), stellar mass (third panel), stellar radius (fourth panel), and ionizing photon emissivity (bottom panel). The red and blue lines in each panel represent Model A and B (Table 2.1). Evolution for constant accretion rates of 0.1 $M_\odot\,\mathrm{yr}^{-1}$ and 10^{-3} $M_\odot\,\mathrm{yr}^{-1}$ are also shown by the black dashed and dot-dashed lines respectively. The black dot-dashed lines for 10^{-3} $M_\odot\,\mathrm{yr}^{-1}$ in the bottom two panels are horizontally shifted so that the line of the mass increase matches that for 0.1 $M_\odot\,\mathrm{yr}^{-1}$, e.g., $M_* = 100$ $\mathrm{M}_\odot$ at the time of 10^3 yr. The radii and ionizing photon emissivity for ZAMS stars are also shown by the thick gray dashed lines, where ZAMS mass is translated to time by the relation of $t = M_{\mathrm{ZAMS}}/0.1$ $M_\odot\,\mathrm{yr}^{-1}$. In the bottom panel, the horizontal dotted line represents the critical value of ionizing photon emissivity above which UV feedback would become significant for the accretion rate 0.1 $M_\odot\,\mathrm{yr}^{-1}$ (see Section 2.4.1). This figure is reproduced from Sakurai et al. (2015).

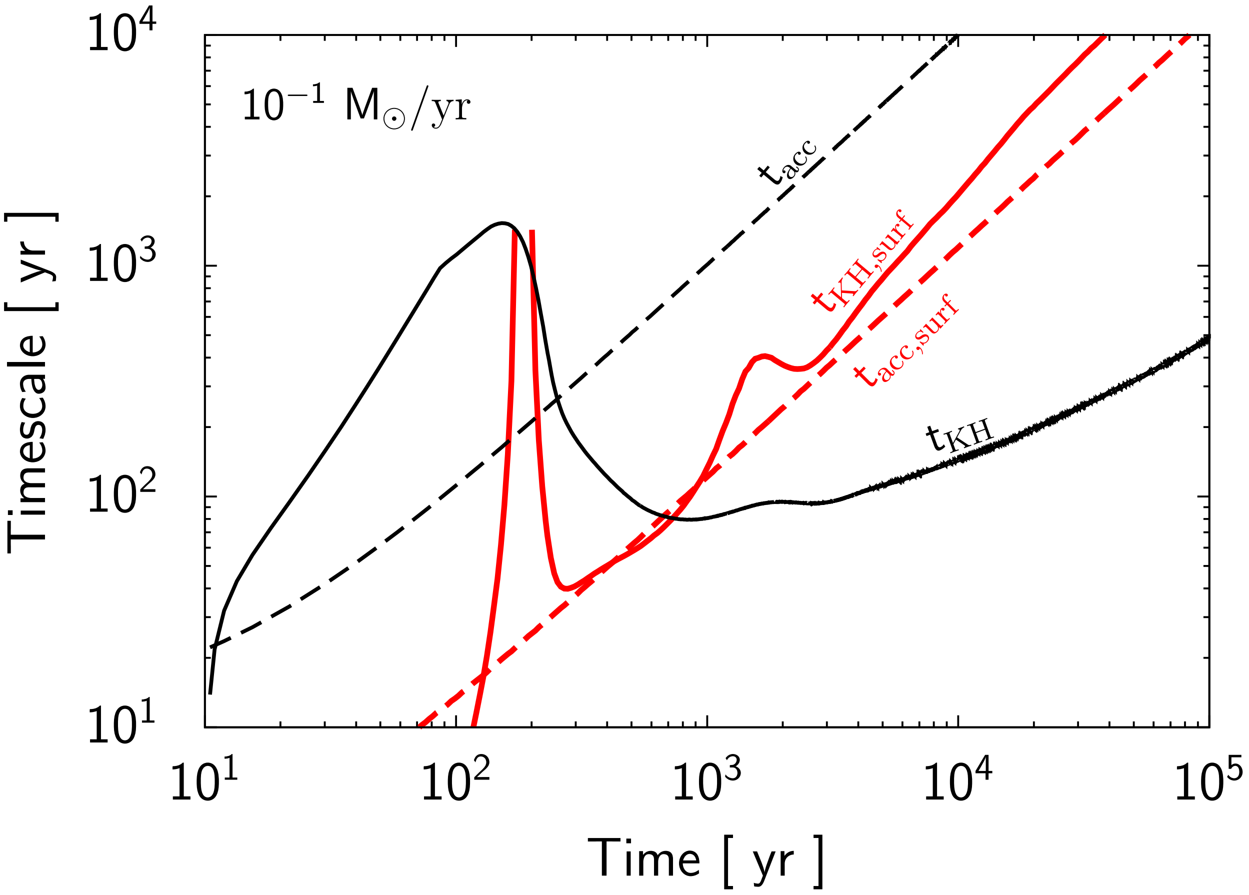

Fig. 2.2 Evolution of the time scales for the constant accretion case of 0.1 $M_\odot\,{\rm yr}^{-1}$. The KH time $t_{\rm KH}$ (black solid) and accretion time $t_{\rm acc}$ (black dashed) as in equations (2.6) and (2.7) are plotted respectively. The local KH time $t_{\rm KH,surf}$ (red solid) and accretion time $t_{\rm acc,surf}$ (red dashed) as in equations (2.9) and (2.10) are also plotted. This figure is reproduced from Sakurai et al. (2015).

protostar. UV feedback is then too weak to stop the rapid accretion (see Section 2.4.1).

We have found that despite the time scale imbalance $t_{\rm KH} < t_{\rm acc}$, the protostar continues to inflate. We can explain the apparent discrepancy by noticing the fact that the usual KH time scale $t_{\rm KH}$ in equation (2.6) is a global quantity which does not takes into account the internal structure of the star. In the stellar interior, most of the mass is concentrated in the central region and the bloating surface region has a small fraction of the stellar mass (see fig. 2 in Hosokawa et al. (2013)). We thus define the local KH time scale for the surface layer which is evaluated considering the actual mass distribution in the star,

$$t_{\rm KH,surf} = f\frac{\int s_{\rm rad} T {\rm d}m}{\int {\rm d}l}, \tag{2.9}$$

where $s_{\rm rad}$ is entropy of radiation and f is a dimensionless constant of $\mathcal{O}(1)$. The time scale is deemed as a surface KH time scale since the numerator corresponds to the thermal energy in the surface region and the denominator corresponds to the energy flux in the same region, which is in analogy with the usual definition $t_{\rm KH}$ in equation (2.6). The factor f is introduced assuming that only a fraction of the surface energy is radiated away over the time scale. Note that the surface KH time scale $t_{\rm KH,surf}$ does not match $t_{\rm KH}$ even if we integrate over whole star because of the inhomogeneous internal structure of the star. The above local KH time scale is compared with the local accretion time scale for the surface region

$$t_{\rm acc,surf} = f \frac{\int {\rm d}m}{\dot{M}_*}. \tag{2.10}$$

For consistency, the same factor f is also included in equation (2.10). We set $f = 0.4$ as a fit to our numerical results and the range of integration $0.7\ M_* \leq m \leq M_*$ in equations (2.9) and (2.10) to cover the surface layer. We have checked that the choice of the lower limit of the integration does not significantly affect the main results. In Figure 2.2 we show that the local accretion time scale $t_{\rm acc,surf}$ continues to be shorter than the local KH time scale $t_{\rm KH,surf}$ even when the global time scales satisfies $t_{\rm KH} < t_{\rm acc}$. The star keeps expanding because, with the rapid mass accretion, gas accumulates faster than heat escapes by radiation in the surface layer. We will show that the two local time scales $t_{\rm KH,surf}$ and $t_{\rm acc,surf}$ can be used for understanding stellar evolution via episodic accretion.

2.3.2 Stellar evolution via episodic accretion

2.3.2.1 The fiducial case: Model C

We first focus on the Model C as a fiducial case of stellar evolution via episodic accretion. In this model, the accretion rates in the burst and quiescent phases are $\dot{M}_{*,b} = 1\ M_\odot\,{\rm yr}^{-1}$ and $\dot{M}_{*,q} = 10^{-3}\ M_\odot\,{\rm yr}^{-1}$ with time durations of $\Delta t_{\rm b} = 100$ yr and $\Delta t_{\rm q} = 1080$ yr (Table 2.1). The accretion history is plotted in the top panel of Figure 2.3. The protostellar evolution is also shown in Figure 2.3, where there are differences from the case with the constant accretion rate $0.1\ M_\odot\,{\rm yr}^{-1}$. Firstly, the star shrinks during the quiescent phases. For instance, when $300\ {\rm yr} \lesssim t \lesssim 1500$ yr the stellar radius decreases to $100\ R_\odot$ which is about 10 times smaller than the supergiant protostar with the constant accretion of $\dot{M}_* = 0.1\ {\rm M}_\odot$. In addition, the stellar contraction leads to the increase of ionizing photon emissivity which eventually reaches the level for ZAMS stars.

Because the accretion rate during the quiescent phases is smaller than the critical rate for maintaining the star inflating $\dot{M}_{*,\rm cr} \simeq 0.04\ M_\odot\,{\rm yr}^{-1}$, the star shrinks as in the normal KH contraction stage. To demonstrate this, we analytically derive an equation for the time evolution of the stellar radius assuming that the contraction continues over the usual KH time scale [*1],

$$\frac{R_*}{R_\odot} = \left(\frac{1}{R_{*,0}/R_\odot} + C \frac{t - t_0}{1\ {\rm yr}} \frac{1}{M_*/{\rm M}_\odot} \right)^{-1}, \tag{2.11}$$

where C is a fitting parameter, and the quantities at the beginning of the contraction have the subscript 0. In the fourth panel of Figure 2.3, the fitting curve from equation (2.11) is plotted (black solid line) together with out numerical result.

The protostar again expands when the next burst accretion occurs and accordingly the ionizing photon emissivity decreases. The cycle of contraction and expansion is repeated for the following two cycles of quiescent and burst phases when $2000\ {\rm yr} \lesssim t \lesssim 5000$ yr. As the star gets more mass,

---

[*1] Using equation (2.6), the time derivative of the stellar radius is

$$\frac{{\rm d}R_*}{{\rm d}t} \sim -\frac{R_*}{t_{\rm KH}} = -\frac{L_* R_*^2}{G M_*^2}.$$

The stellar luminosity is well approximated by the Eddington luminosity $L_{\rm Edd} \propto M_*$ and the equation becomes

$$\frac{{\rm d}R_*}{{\rm d}t} = -{\rm const.} \times \frac{R_*^2}{M_*}.$$

Regarding the stellar mass almost constant during quiescent phases, integration of the equation gives equation (2.11).

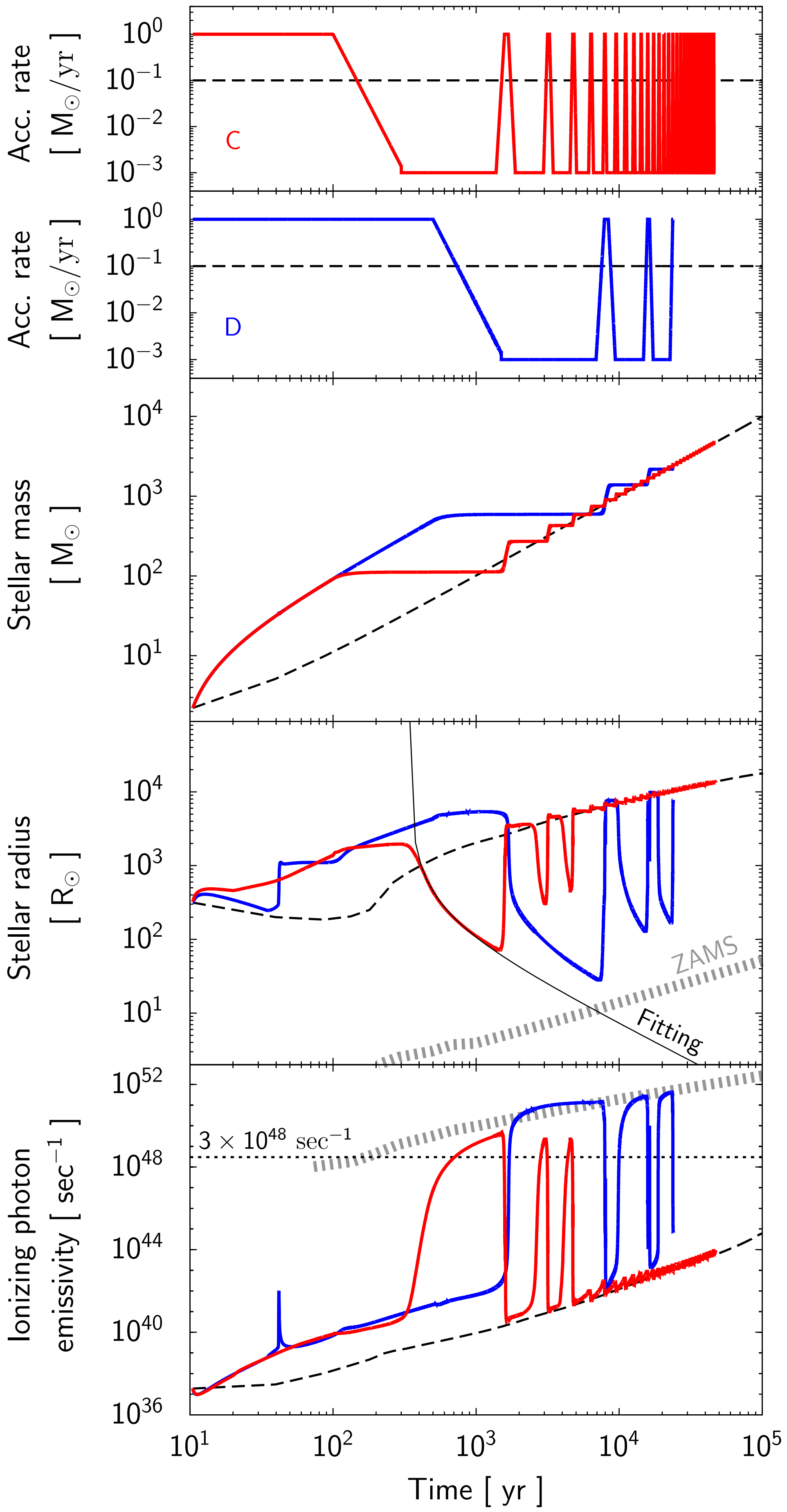

Fig. 2.3 The same plots as Figure 2.3 but for Models C and D (Table 2.1) which are represented by red and blue lines respectively. The black solid line in the fourth panel is a fitting for the KH contraction in Model C (see text for detail). This figure is reproduced from Sakurai et al. (2015).

the degree of the contraction gradually diminishes. The stellar contraction hardly occurs during the quiescent phases for $t \gtrsim 5000$ yr, i.e., $M_* \gtrsim 500$. Overall, for the model C, the ionizing photons can cause stellar feedback in the early evolutionary epoch.

We understand the numerical result by comparing the duration of the quiescent phase Δt_q to the local KH time scale at the surface layer $t_\mathrm{KH,surf}$ which is defined in equation (2.9). For the range of the integration in equation (2.9), we take a surface layer of $0.01\ R_* \leq r \leq R_*$ which contains only $\simeq 10 - 30\%$ of the stellar mass but 99.9999% of the volume. As shown in Figure 2.4, the surface KH time scale monotonically increases with time and stellar mass, other than some bump features which appear during the stellar contraction. The increase of $t_\mathrm{KH,surf}$ with stellar mass is explained by rewriting equation (2.9) as

$$t_\mathrm{KH,surf} \sim f \frac{\int Gm/r \mathrm{d}m}{\int \mathrm{d}l} \propto \frac{GM_*^2}{L_* R_*} \propto M_*^{1/2}, \tag{2.12}$$

where the second term comes from the hydrostatic equilibrium for radiation pressure, $Ts_\mathrm{rad} \sim P_\mathrm{rad}/\rho \sim Gm/r$, and we use the relations $L_* \sim L_\mathrm{Edd} \propto M_*$ and $R_* \propto M_*$ (see equation 2.8). For $t \lesssim 5 \times 10^3$ yr, the surface KH time scale is shorter than the duration of the quiescent phases. In this early stage, the quiescent phase is long enough so that the protostar loses its thermal energy trapped in the surface layer and then contracts.

Even in this case, however, the contraction of the star does not promptly follow the decrease of the accretion rate. For example, after the first burst, the accretion rate drops below $\dot{M}_{*,\mathrm{cr}}$ at $t \simeq 150$ yr (Figure 2.3), but the stellar contraction commences only at $t \simeq 400$ yr. The top panel of Figure 2.4 shows that the surface KH time at this time is a few 100 yr, which is comparable to the delay time of the contraction. In addition, Figure 2.3 shows that, after the second and third bursts at $t \sim 2000 - 4000$ yr, the corresponding delay lengthens to $\sim 10^3$ yr. The delay time is also consistent to the calculated surface KH time at $t \sim 2000 - 4000$ yr in the top panel of Figure 2.4.

As described in Section 2.3.1.2, it is crucial to use $t_\mathrm{KH,surf}$ as the thermal time for the inflating protostars instead of the usual KH time t_KH. The latter time scale is a global quantity for which the inhomogeneous internal structure of the star is not taken into account. As seen in Figure 2.5 and Figure 2.6, the mass is actually strongly concentrated in the central region when the star is bloating. For $M_* \sim 4 \times 10^3\ \mathrm{M}_\odot$ or $t \sim 4 \times 10^4$ yr, for instance, 0.0001 percent of the central volume contains ~ 90 percent of the stellar mass (Figure 2.6).

As seen in the top panel of Figure 2.4, for the bloating phases, the normal KH time t_KH is shorter than the surface KH time $t_\mathrm{KH,surf}$. It might appear puzzling that the global time t_KH is shorter than the local time $t_\mathrm{KH,surf}$. To solve the puzzle, we first note that the normal KH time provides the thermal time if

$$\int_0^{M_*} \frac{Gm}{r} \mathrm{d}m \sim \frac{GM_*}{R_*}, \tag{2.13}$$

which is not the case for the bloating protostar. Since most of the mass is concentrated near the stellar center, we actually have

$$\int_0^{M_*} \frac{Gm}{r} \mathrm{d}m \sim 10 - 100 \frac{GM_*}{R_*}, \tag{2.14}$$

depending on accretion history and the stellar mass. As a consequence, the effective thermal time for the whole star is now $t_\mathrm{KH,eff} \sim 10 - 100 \times t_\mathrm{KH}$, which at any time is larger than the local surface KH time $t_\mathrm{KH,surf}$.

We confirmed that the effective KH time $t_\mathrm{KH,eff}$ becomes comparable to Δt_q at $\sim 10^3$ yr, which

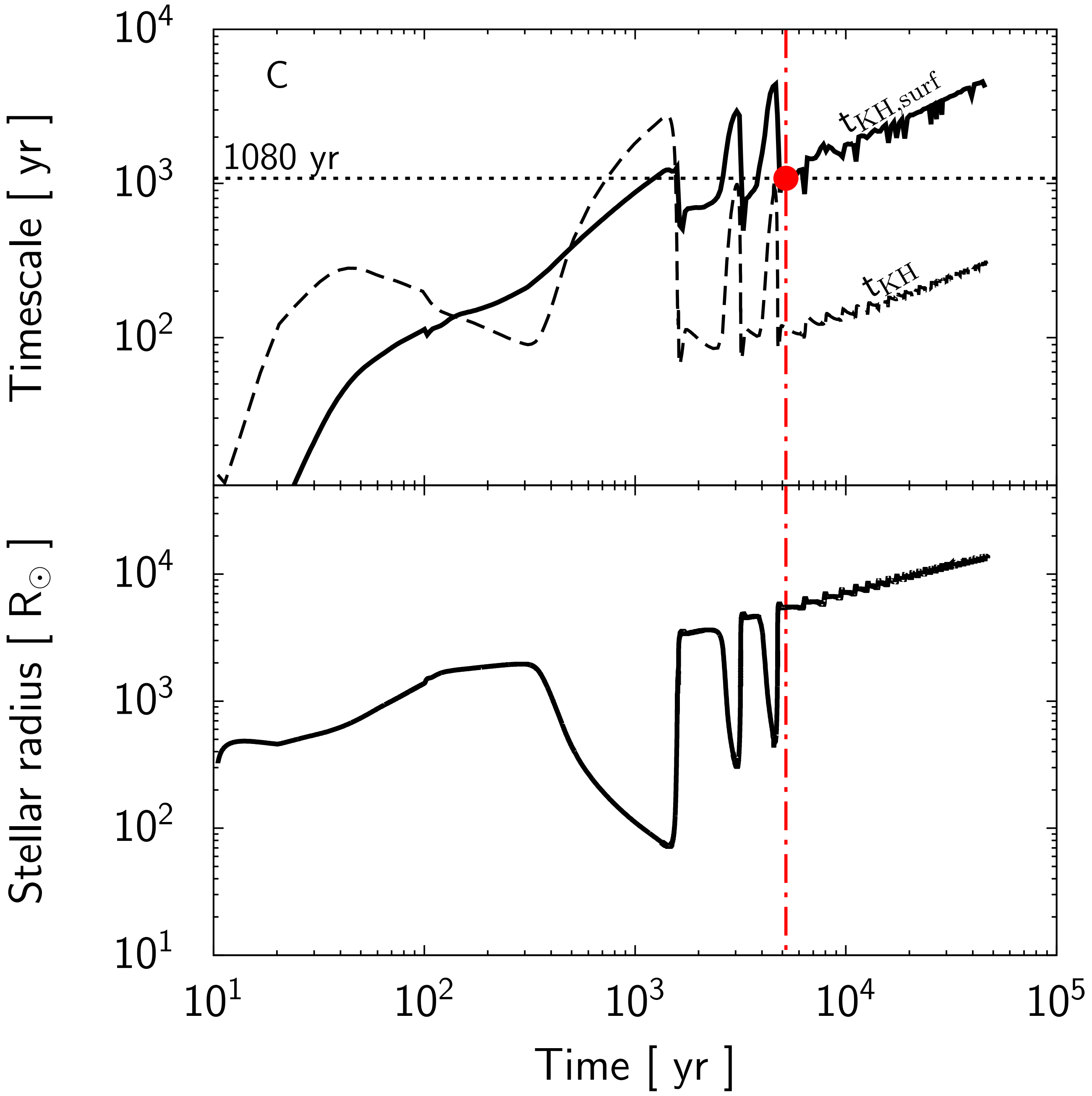

Fig. 2.4 *Upper panel*: the surface KH time $t_{\rm KH,surf}$ (solid line, equation 2.9) and the KH time of the usual definition (dashed line, equation 2.6) are compared to the duration of the quiescent phase $\Delta t_{\rm q}$ (horizontal dotted line) for Model C. The red circle and vertical dot-dashed line represents the time when $t_{\rm KH,surf} = \Delta t_{\rm q}$. *Lower panel*: evolution of the stellar radius in Model C. The star can contract only for the quiescent phases and the early epoch when $t_{\rm KH,surf} \lesssim \Delta t_{\rm q}$. This figure is reproduced from Sakurai et al. (2015).

does not point the time when the stellar contraction ceases. For the bloating star, only entropy in the stellar surface layer determines whether the star contracts or not. Thus, it is reasonable to use the surface KH time $t_{\rm KH,surf}$ for comparison to $\Delta t_{\rm q}$.

2.3.2.2 Variations with different episodic accretion histories

The numerical results of Models A, B and D can be explained based on our findings for Model C. In Model B, for instance, the fourth panel of Figure 2.1 shows that the stellar contraction during the quiescent phases ceases when $t \gtrsim 2000$ yr. The top panel of Figure 2.7 shows the evolution of the KH times for Model B. We see that $t_{\rm KH,surf}$ increases with time and becomes comparable to the duration of the quiescent phases $\Delta t_{\rm q}$ at $t \simeq 2000$ yr, which explains the absence of stellar contraction

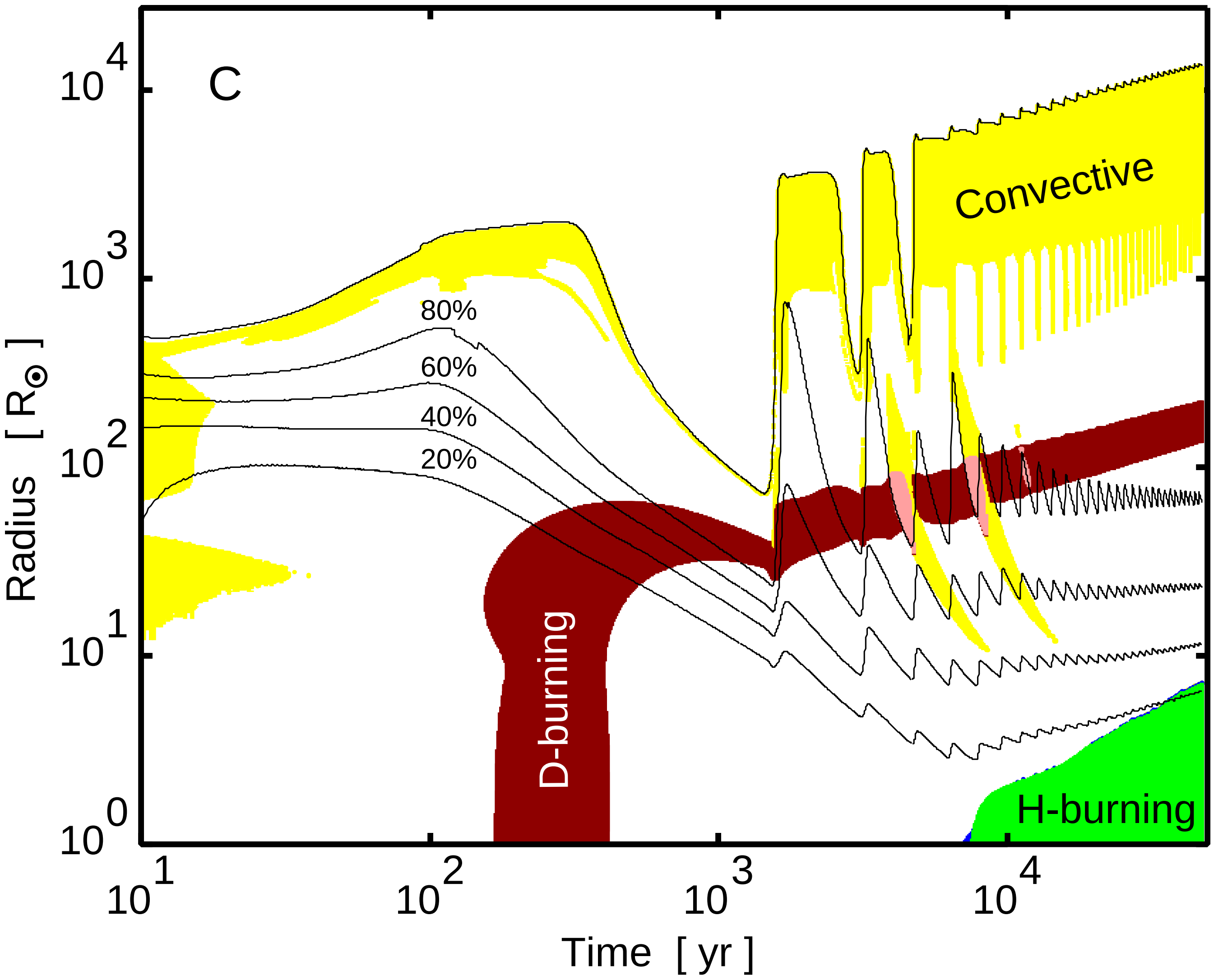

Fig. 2.5 Evolution of the stellar internal structure in Model C. The black solid lines represents the positions of the mass coordinates for 20, 40, 60, 80 and 100 per cent of the total stellar mass in ascending order. The white, yellow, green, brown and pink regions indicate radiative layers, convective layers, a hydrogen-burning convective core, deuterium-burning layers and deuterium-burning convective layers respectively. The burning regions are identified where the depletion time of the corresponding composition is shorter than the main sequence lifetime. Note that the stellar mass is roughly estimated as $\overline{\dot{M}_*}t$ for $t \gtrsim 10^3$ yr, where $\overline{\dot{M}_*}$ is the average accretion rate. This figure is reproduced from Sakurai et al. (2015).

for the late epoch.

Figure 2.1 and Figure 2.3 show that the protostar stops contracting earlier for the models with shorter duration of quiescent phases. Unless the stellar contraction lasts for a long time, the resulting rise of the stellar ionizing photon emissivity is not significant. We conclude that episodic accretion causes stellar contraction and possible UV feedback when a quiescent phase continues for $\gtrsim 10^3$ yr (see Section 2.4.1).

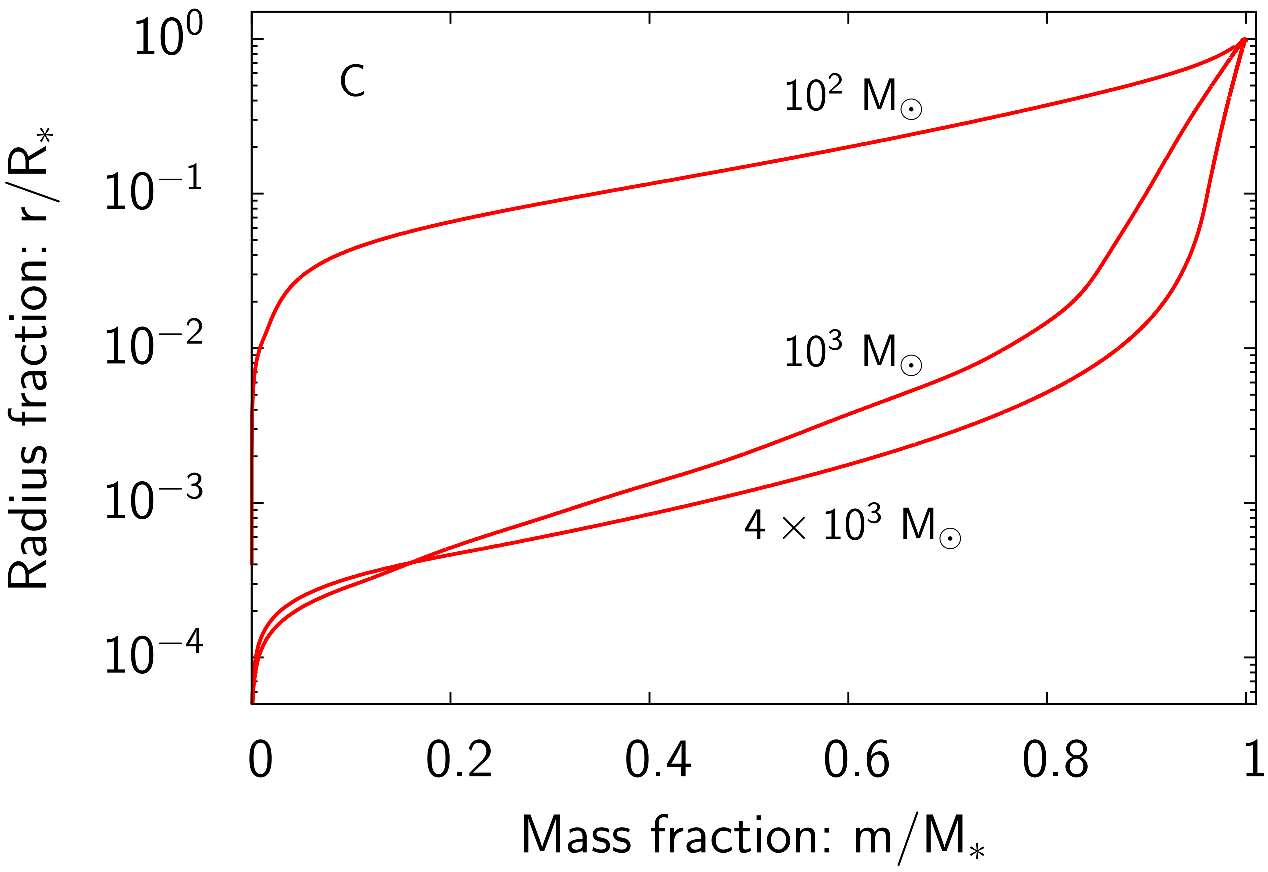

Fig. 2.6 The internal mass distribution of the star for Model C. The three distributions for $M_* = 10^2, 10^3$ and $4 \times 10^3 = \mathrm{M}_\odot$ ($t = 10^2, 10^4, 4 \times 10^4$ yr) are represented. The latter two plots are for the bloating protostars. The normalized quantities m/M_* and r/R_* are used for the horizontal and vertical axes respectively, where m is the mass coordinate and r is the radial distance from the stellar center. This figure is reproduced from Sakurai et al. (2015).

2.4 Discussions

2.4.1 UV feedback from SMSs evolving via episodic accretion

We discuss whether UV photons emitted from a growing SMS with episodic accretion can ionize the surrounding gas to cause radiation feedback. We derive the lower limit of ionizing photon emissivity for the UV feedback to be effective by assuming that the feedback sets in when all accreting atoms are ionized. From the estimate of the total number of neutral hydrogen and helium atoms accreting per second for $\dot{M}_* = 0.1\ M_\odot\,\mathrm{yr}^{-1}$, the critical ionizing photon emissivity is $S_\mathrm{min} \equiv 3 \times 10^{48}\ \mathrm{s}^{-1}$. The critical value is represented by the dotted horizontal lines in the bottom panels of Figure 2.1 and Figure 2.3. In Models A and B, with the short durations of the quiescent phase Δt_q, the emissivity is always lower than S_min. By contrast, in Model C and D which have the longer duration of the quiescent phase, the emissivity gets larger than S_min when the star contracts during the quiescent phases. Overall, the UV feedback becomes effective in quiescent phases if $\Delta t_\mathrm{q} \gtrsim 10^3$ yr, even for the average accretion rate of $0.1\ M_\odot\,\mathrm{yr}^{-1}$.

There are several uncertainties about the UV feedback since we do not see evolutions and structures of a circumstellar disk and a gas envelope. For example, UV photons can be consumed by re-ionizing the recombining gas within an H II region. Moreover, even if the H II region appears around the star,

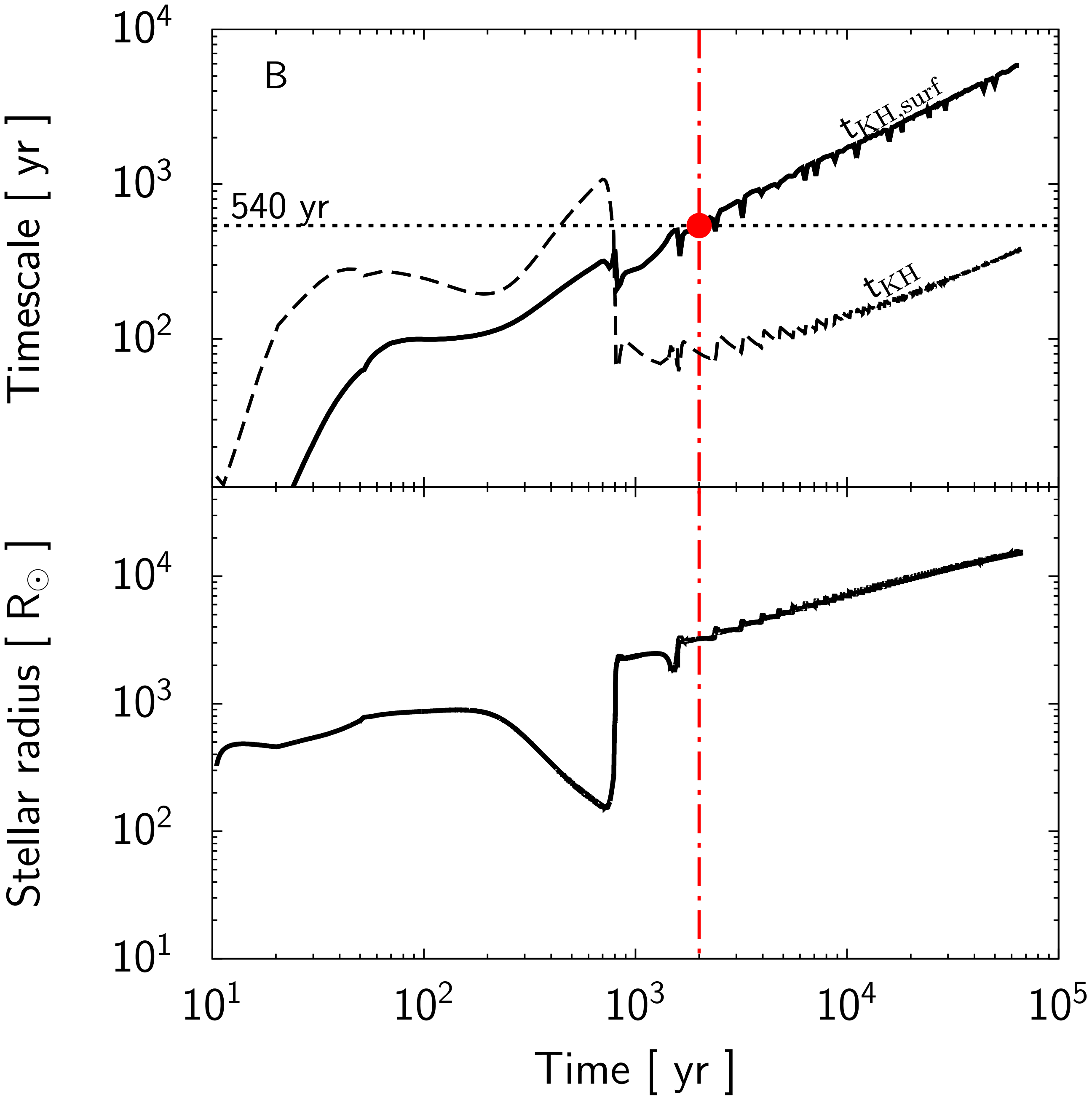

Fig. 2.7 The same plot as Figure 2.4, but for Model B. This figure is reproduced from Sakurai et al. (2015).

its expansion can be hindered by a burst accretion, which is induced by gravitational instability of the accretion disk. The disk can become gravitationally unstable after the H II region emerges, if mass supply from the gas envelope to the accretion disk continues, e.g., with UV photons escaping preferentially to polar directions to form anisotropic H II regions (e.g., Hosokawa et al. 2011). With the unstable disk and the resulting burst accretion, the star stops contracting and expands, the ionizing photon emissivity strongly decreases and the H II region disappears. Some of the gas expelled by the expanding H II region may fall back on to the disk before the H II region again emerges during the next stellar contraction. Therefore, it is still uncertain whether the protostar can continue to grow via episodic accretion and intermittent UV feedback. Further studies are necessary to examine the overall impact of episodic accretion on disk accretion and formation of H II regions.

2.4.2 Stellar evolution for $M_* \gtrsim 10^4$ M$_\odot$

Due to difficulty in numerical convergence, we have stopped the calculation at the stellar mass $M_* \lesssim 10^4$ M$_\odot$. The mass is below the putative critical mass 10^{5-6} M$_\odot$ at which for $\gtrsim 0.1\ M_\odot\,\mathrm{yr}^{-1}$ non-rotating SMSs collapse to form seed black holes by general relativistic instability (e.g., Shibata, Uchida & Sekiguchi 2016). Regarding the later evolution for $M_* \gtrsim 10^4$ M$_\odot$ until the black hole formation, the surface KH time will continue to increase with the stellar mass (equation 2.12). Since $\Delta t_\mathrm{q} \lesssim 10^3$ yr $< t_\mathrm{KH,surf} \propto M_*^{1/2}$, entropy in the stellar surface layer will remain high and the contraction of the more massive star will become harder. In the absence of the stellar contraction, the drastic increase of ionizing photon emissivity will not occur.

It is possible, however, that UV feedback becomes effective without significant stellar contraction in late evolutionary phases. Hosokawa et al. (2013) calculate the later stellar evolution for 10^4 M$_\odot \lesssim M_* \lesssim 10^5$ M$_\odot$ with a higher constant accretion rate $1\ M_\odot\,\mathrm{yr}^{-1}$. Such a high accretion rate is actually suggested for the direct collapse case by numerical simulations (e.g., Latif et al. 2013). Although in this case the star also expands following equation (2.8) for $M_* \lesssim 10^4$ M$_\odot$, the stellar expansion ceases after the mass exceeds a few $\times 10^4$ M$_\odot$. The effective temperature of the star and UV emissivity accordingly rise, irrespective of the variability in an accretion history. The ionizing photon emissivity reaches $\sim 10^{50}\ \mathrm{s}^{-1}$ for $M_* \sim 10^5$ M$_\odot$ (see fig. 11 in Hosokawa et al. (2013)), which exceeds the critical value S_min for accretion rates $0.1 - 1\ M_\odot\,\mathrm{yr}^{-1}$. Thus, UV feedback may finally regulate the growth of the SMSs before the seed black hole formation.

2.4.3 Accretion histories in atomic-cooling halos

We have modeled the time variable accretion histories by simple functional forms with several free parameters (Table 2.1). Despite progresses in 3D numerical simulations, a long-term accretion history for a SMS formation is not well understood. Latif et al. (2013) simulate the long-term evolution for the protostellar accretion phase using the so-called sink cell technique. Their obtained accretion histories show some time variability (see their fig. 4), but overall rather smoother than our model accretion histories. Regan, Johansson & Wise (2014) and Becerra et al. (2015) perform simulations with much higher spatial resolutions and find signatures of disk fragmentation. Though their simulations only follow the initial $10 - 100$ yr for the accretion phase, the results suggest that highly time-dependent accretion can be realized for the direct collapse model.

Vorobyov, DeSouza & Basu (2013) follow the long-term evolution of a self-gravitating disk for normal Pop III star formation cases by high-resolution 2D simulations. In the simulations, highly time-variable episodic accretion occurs with a mean accretion rate $\sim 10^3\ M_\odot\,\mathrm{yr}^{-1}$, which indicates the accretion rate on to the disk from a surrounding envelope. As the disk gets more mass and becomes more gravitationally unstable, fragmentation occurs and clumps migrate inward to the star, resulting in an increase of the accretion rate to $\sim 10^{-2} - 0.1\ M_\odot\,\mathrm{yr}^{-1}$. In the intervals between such accretion burst events, the accretion rate falls to $10^{-5} - 10^{-4}\ M_\odot\,\mathrm{yr}^{-1}$.

Episodic accretion with large variations is also expected for a large mean accretion rate of $\sim 0.1\ M_\odot\,\mathrm{yr}^{-1}$ in the direct collapse case. In particular, the duration of the quiescent phase Δt_q is a key value since the value determines whether the star contracts or not. The value Δt_q will be controlled by the two time scales, namely, the effective fragmentation time t_frag and the migration time t_mig. The fragmentation time t_frag is the mean time for a fragment to form in a self-gravitating disk or the inverse of a clump formation rate. The migration time t_mig is the time scale over which new-born fragments migrate inward to the star. We expect $\Delta t_\mathrm{q} \sim t_\mathrm{frag} + t_\mathrm{mig}$.

The two time scales can be estimated based on previous numerical and analytical studies. For instance, Vorobyov, Zakhozhay & Dunham (2013) find that, based on their simulations of the present-day star formation, $t_{\rm frag}$ can be determined by the time scale over which the disk grows via mass supply from the accretion envelope,

$$t_{\rm frag} = \frac{M_{\rm d}}{\dot{M}_{\rm d}}, \tag{2.15}$$

where $M_{\rm d}$ is the disk mass and $\dot{M}_{\rm d}$ is the accretion rate on to the disk.

For the estimation of $t_{\rm mig}$, the analytic model of Inayoshi & Haiman (2014) is useful which describes the structure of an accretion disk around an SMS for the accretion rate $0.1\ M_\odot\,{\rm yr}^{-1}$. They consider migration of a fragment from the fragmentation radius $R_{\rm f}$ within which disk fragmentation is efficient. When $M_* \lesssim 10^4\ {\rm M}_\odot$, the radius $R_{\rm f}$ is well in the regions where the disk gravity dominates the protostellar gravity, and in this case the migration time is approximately estimated as the viscous time scale,

$$t_{\rm mig,max} \simeq 4 \times 10^3\ {\rm yr}. \tag{2.16}$$

This can be considered as the maximum time scale since the fragment formed within $R_{\rm f}$ will have the shorter migration time.

We can predict the evolution of $\Delta t_{\rm q}$ by comparing the two time scales $t_{\rm frag}$ and $t_{\rm mig}$. In an early evolutionary phase for $t_{\rm frag} < t_{\rm mig}$, the duration of the quiescent phase $\Delta t_{\rm q}$ is limited by the migration time $t_{\rm mig}$. In this stage, the quiescent phase lasts for $t_{\rm mig} < 4 \times 10^3$ yr, which can be shorter than the critical value 10^3 yr for the formation of an H II region (Section 2.3.2.2). For the accretion rate $0.1\ M_\odot\,{\rm yr}^{-1}$ from the envelope on to the disk, however, the fragmentation time scale $t_{\rm frag}$ will exceed the migration time when the disk mass reaches $\sim 400\ {\rm M}_\odot$. After this time, the quiescent phase will become longer assuming that the disk mass increases with the stellar mass. Unlike the stellar evolution for the constant duration $\Delta t_{\rm q}$, the SMS may further contract during prolonged quiescent phases. The ionizing photon emissivity from the star would be enhanced by the contraction.

In order to verify our analytic expectation, we need to obtain realistic accretion histories realized in an atomic-cooling halo. The accretion rates can be derived by multidimensional hydrodynamic simulations which follow the dynamic process of accretion on to growing SMSs.

2.4.4 Metallicity effects on SMS growth

We have assumed that accreting gas is pristine. If the gas has been polluted by some metals, the gas thermal evolution for the direct collapse model will be changed by additional coolants of heavy elements and dust grains (Omukai, Schneider & Haiman 2008). If the gas temperature is reduced below 3000 K during the collapse phase of star formation, the resulting accretion rates will be smaller than the critical rate necessary for a bloating giant protostar, $\dot{M}_{*,\rm cr} = 0.04\ M_\odot\,{\rm yr}^{-1}$. In this case, the star would contract and start to emit a copious amount of UV photons. However, cooling by heavy elements and dust grains often operates only in the late stage of the collapse and the early accretion stage on to the protostar at high densities. The accretion rate will therefore be small only when the protostellar mass and luminosity are relatively low. In the later stage the accretion rate may significantly increase, which can trigger the abrupt expansion of the growing protostar and quench the stellar UV flux.

Other effects of varying metallicity can further modify the evolution. For instance, both the collapsing and accreting gas can fragment via gravitational and thermal instabilities (e.g., Katz, Sijacki & Haehnelt 2015, Inoue & Omukai 2015). Moreover, opacity of the accreting gas will be enhanced for higher metallicity. With the larger opacity, the radiation feedback of the star will more easily disrupt the accretion envelope, e.g., by radiation pressure exerting on dust particles contained in the gas (Hosokawa & Omukai 2009b). We naively expect that the formation of SMSs is suppressed if the metallicity is above some critical metallicity, but the detail of the evolution in such 'failed' cases is uncertain and remains to be studied in future work.

2.5 Conclusions

We have studied the evolution of supergiant protostars which grow via episodic accretion, which is expected in gravitationally unstable circumstellar disks forming in atomic-cooling halos (Regan, Johansson & Wise 2014, Inayoshi & Haiman 2014, Becerra et al. 2015). The protostellar evolution have been followed with various accretion histories which are controlled by free parameters to mimic repeating short bursts and long quiescent phases (see Table 2.1 and the top panels of Figure 2.1 and Figure 2.3). We fix the mean accretion rate of the models to 0.1 $M_\odot\,\mathrm{yr}^{-1}$ and consider different variabilities to examine potential impact of the episodic accretion.

The episodic accretion can qualitatively change the evolution of an accreting SMS, in contrast to the constant accretion case in which the stellar radius monotonically increases with growth of the stellar mass (equation 2.8). In the episodic accretion cases, the star can contract during the quiescent phases between the bursts. Along with the stellar contraction, stellar ionizing photon emissivity significantly increases due to a rapid rise of the effective temperature. Specifically, for a quiescent phase of length $\Delta t_\mathrm{q} \gtrsim 10^3$ yr, the emissivity exceeds $3 \times 10^{48}\ \mathrm{s}^{-1}$, which allows formation of an H II region. Consequently, UV feedback might hinder the mass accretion on to the protostar.

With a fixed duration of the quiescent phase Δt_q, the star can contract in an early epoch, e.g., for $M_* \lesssim 10^3\ \mathrm{M}_\odot$ in our model C with $\Delta t_\mathrm{q} \simeq 10^3$ yr (see Figure 2.3). With a longer Δt_q, however, the stellar contraction will continue until the star gets much more mass. This stellar behavior is well understood by comparing the duration of the quiescent phase to the surface thermal (or KH) time $t_\mathrm{KH,surf}$ defined by equation (2.9). As the surface KH time increases with growth of the stellar mass, the imbalance of the two time scales changes from $t_\mathrm{KH,surf} < \Delta t_\mathrm{q}$ to the opposite at some point. Before the point, the star contracts significantly in the quiescent phases because the inflating surface layer loses most of entropy before the next burst occurs. After the time scale inversion to $t_\mathrm{KH,surf} > \Delta t_\mathrm{q}$, the stellar contraction ceases and the stellar radius increases following the mass-radius relation in equation (2.8). The same time scale comparison using the global KH time t_KH instead of $t_\mathrm{KH,surf}$ severely overestimates the critical mass above which the star stops to contract. The overestimation stems from the inhomogeneous internal structure of the bloating star which is not taken into account in the definition of the global time t_KH. Since the mass distribution of the bloating star is very centrally condensed (Figure 2.1 and Figure 2.3), the global KH time provides a poor estimate for the thermal time.

Our calculations show that stellar radiation feedback may become important if the quiescent phase lasts longer than 10^3 yr. Such long intervals between accretion bursts are expected for an accretion disk around a growing SMS (Inayoshi & Haiman 2014). If the UV feedback halts the stellar mass growth, the final mass of the SMS is reduced and the mass of the remnant BH which is left behind after the death of the star is also reduced. We discuss that the stellar UV feedback may be effective and determine the final mass, by adopting a simple functional form with parameters (Table 2.1) to model the accretion histories, where the duration of quiescent phases is constant. In more realistic cases, the length of the quiescent phase can vary with time and the accretion histories need to be examined by hydrodynamical simulations for more correct estimation of the final mass. The stellar evolution and strength of the resulting UV radiation feedback for this case is studied as in Chapter 3.

Chapter 3

Primordial supermassive star formation via episodic accretion: II. Protostellar disk instability and radiation feedback efficiency

3.1 Overview

In Chapter 2, we examine the evolution of supermassive stars (SMSs) with rapid episodic accretion histories. Since we have used the parameterized accretion histories, we could not correctly judge whether or not the SMS realistically contracts and emits a copious amount of UV photons to cause radiation feedback. We here study the evolution of an accreting SMS and its UV emissivity with realistic variable accretion from a circumstellar disk. To correctly follow the circumstellar disk structure and evolution, at least a 2D simulation is necessary. First we perform a 2D hydrodynamical simulation to follow the protostellar accretion through the disk until the stellar mass exceeds 10^4 $\mathrm{M}_\odot$. The disk fragments by gravitational instability, forming many clumps that migrate inward to fall on to the central star. A resulting accretion history is highly time-dependent: short episodic accretion bursts are followed by prolonged quiescent phases. We show that the disk in the direct collapse model is more unstable and presents greater variability than that in normal Pop III cases. Next, we perform a stellar evolution calculation using the obtained accretion history. Irrespective of the variable accretion, the stellar radius monotonically increases with nearly constant effective temperature at $T_{\mathrm{eff}} \simeq 5000$ K as the stellar mass increases. The UV photon emissivity is too low to hinder accretion and UV feedback is ineffective. The insensitivity of stellar evolution to variable accretion is ascribed to short time scales of variability, $\lesssim 10^3$ yr, which are shorter than a surface thermal time scale of the bloating SMS. We argue that this evolution will continue until the SMS gravitationally collapses to produce a massive black hole by general relativistic instability after the stellar mass reaches $\gtrsim 10^5$ $\mathrm{M}_\odot$.

3.2 Numerical model

3.2.1 2D hydrodynamical simulations

Our numerical model and method for studying the gravitational collapse of primordial cores are presented in (Vorobyov, DeSouza & Basu 2013). We here briefly review the main concepts and appropriate modifications for the SMS formation. We follow the evolution of gravitationally unstable massive primordial cores from the prestellar stage into the star and disk formation stages. Our simulations are terminated once about 50 per cent of the initial mass reservoir has been accreted on to the star and disk system. Once the disk is formed, it occupies the innermost region of the numerical grid. The dynamics of both the disk and envelope are followed self-consistently on one global grid, which ensures accurate mass infall rates on to the star plus disk system. This self-consistency is an important prerequisite for studying gravitational instability and fragmentation of young circumstellar disks at all epochs.

We introduce a sink cell at the inner boundary of the computational domain with a radius of $R_{\rm sc} = 110$ AU, and allow matter to freely flow into the sink. The radius of the sink cell is chosen to accommodate the maximum radius of the growing central star. In the early prestellar phase, we monitor the mass accretion rate through the sink cell and introduce a central point mass object which represents the forming star. In the subsequent evolution, about 95 per cent of the accreted material is assumed to directly land on to the star. The rest material remains in the sink cell to keep its density equal to the mean density of gas in the innermost $10 - 20$ AU outside the sink cell.

We solve the mass and momentum transport equations written in a thin-disk approximation. A method of finite-differences is used with a time-explicit operator-split procedure described by Stone & Norman (1992) for their ZEUS-2D code. Advection is performed with the third-order piecewise parabolic scheme (Colella & Woodward 1984). Gravitational acceleration includes contributions from the central point mass star once formed, from the material in the sink cell ($r < R_{\rm sc}$), and from the self-gravitating circumstellar disk and envelope.

The equations of mass and momentum transport are closed by a barotropic equation of state for gas pressure P of the form

$$P_k = \mathcal{K} \rho^{\gamma_k} \prod_{i=1}^{k-1} \rho_{{\rm c},i}^{\gamma_i - \gamma_{i+1}} \quad \text{for } \rho_{{\rm c},k-1} \leq \rho < \rho_{{\rm c},k}, \tag{3.1}$$

where $\mathcal{K} = \mathcal{R}T/\mu\rho^{\gamma_1 - 1}$, $T = 8000$ K is the initial temperature of gas, $\mathcal{R}$ is the gas constant, and $\mu = 2.27$ is the mean molecular weight of the primordial gas. The equation is a piecewise fit to the detailed thermal and chemical evolution of a collapsing gas cloud in an atomic-cooling halo, which is calculated by Omukai, Schneider & Haiman (2008) using a one-zone model. In Figure 3.1, the red solid line depicts their exact solution and the red dashed line portrays the piecewise approximation used in our simulations. The five individual components of the approximation are distinguished by the index k as shown in Table 3.1. For each component k, Table 3.1 also shows the values of the associated polytrope indices γ_k and the mass and number densities, $\rho_{{\rm c},k}$ and $n_{{\rm c},k}$, at which the transitions between k and $k+1$ occurs (red dots in Figure 3.1). We note that when $k = 1$ the product term in (3.1) is unity, and the pressure reduces to $P_1 = \mathcal{K}\rho_1^{\gamma}$. Moreover, $\mathcal{K}$ is approximately equal to $c_{\rm s}^2 = \mathcal{R}T/\mu$ where $c_{\rm s}$ is the sound speed, because $\gamma_1 = 0.965 \approx 1.0$.

The form of the barotropic relation is modified in our simulations as

$$\mathcal{P}_k = \mathcal{K} \Sigma^{\gamma_k} \prod_{i=1}^{k-1} \Sigma_{{\rm c},i}^{\gamma_i - \gamma_{i+1}} \quad \text{for } \Sigma_{{\rm c},k-1} \leq \Sigma < \Sigma_{{\rm c},k}, \tag{3.2}$$

where $\mathcal{P}$ is the vertically integrated gas pressure. The transition surface density is related to the transition volume density through the instantaneous local scale height Z at each location in the disk by $\Sigma_{{\rm c},i} = 2Z\rho_{{\rm c},i}$. We calculate the scale height Z assuming a local hydrostatic balance in the gravitational field of both the star and the disk (Appendix A of Vorobyov & Basu 2009).

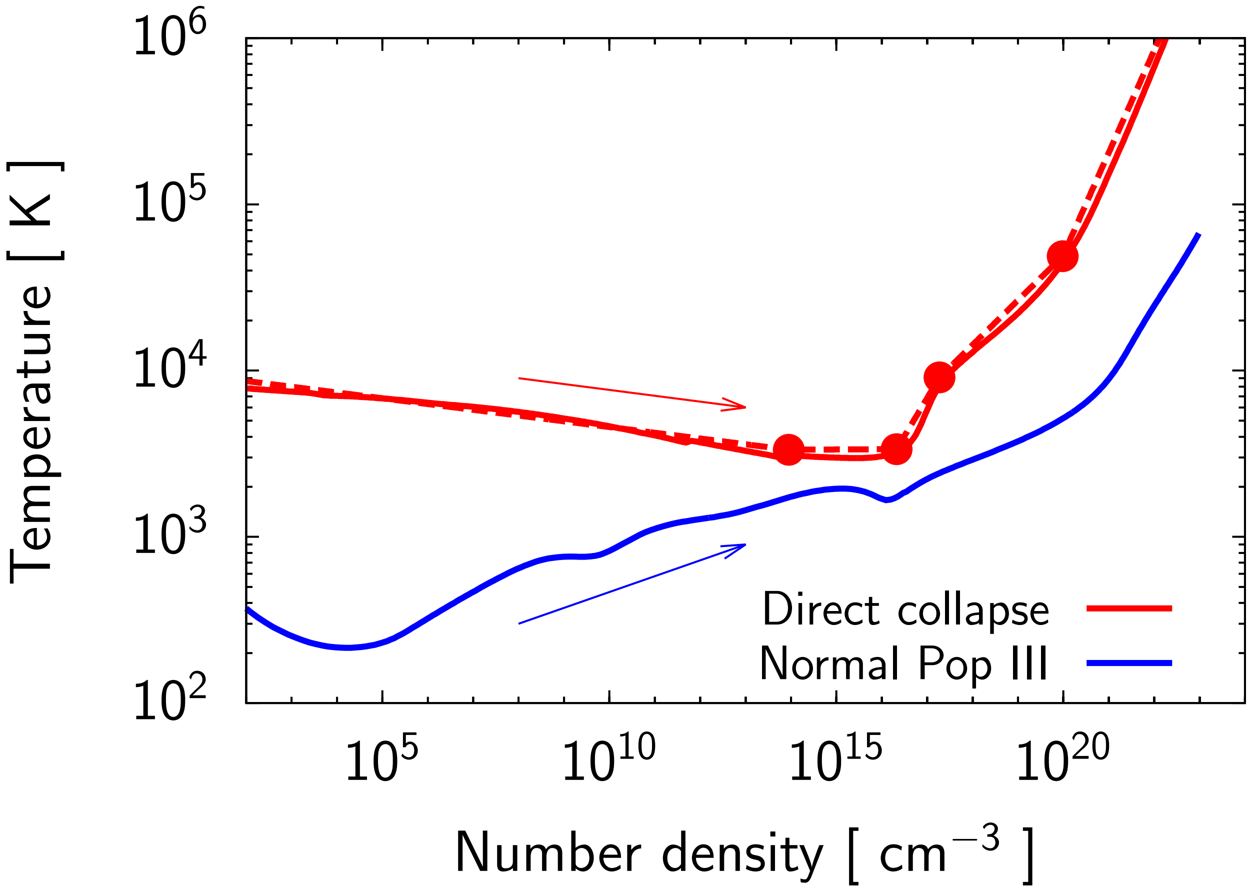

Fig. 3.1 The temperature evolution of collapsing primordial gas as a function of the hydrogen number density. The red line represents the evolution of gas irradiated by a strong UV background radiation corresponding to the direct collapse case (fig.5a of Omukai, Schneider & Haiman 2008: [M/H] = −6). The red dashed line depicts the approximate piecewise polytropic fit used in our simulations. The blue line represents the evolution of metal-free gas without UV background (Omukai et al. 2005). This figure is reproduced from Sakurai et al. (2016).

Table 3.1 Parameters of the barotropic relation. This table is taken from Sakurai et al. (2016).

k	γ_i	$\rho_{\rm c,i}$ (g cm^{-3})	$n_{\rm c,i}$ (cm^{-3})
1	0.965	3.38×10^{-10}	8.92×10^{13}
2	1.002	8.037×10^{-8}	2.12×10^{16}
3	1.456	7.089×10^{-7}	1.87×10^{17}
4	1.269	3.673×10^{-4}	9.69×10^{19}
5	1.614	—	—

The profiles of the initial gas surface density Σ and angular velocity Ω are

$$\Sigma = \frac{r_0\Sigma_0}{\sqrt{r^2+r_0^2}}, \tag{3.3}$$

$$\Omega = 2\Omega_0\left(\frac{r_0}{r}\right)^2\left[\sqrt{1+\left(\frac{r}{r_0}\right)^2}-1\right]. \tag{3.4}$$

The radial profile of Σ is an integrated form of a Bonnor-Ebert sphere. The profile of Ω is the expected differential rotation profile to accompany equation (3.3) (Basu 1997). We use the parameters of the central angular velocity $\Omega_0 = 7.22\ \mathrm{km\,s^{-1}\,pc^{-1}}$, the central gas surface density $\Sigma_0 = 7.63\ \mathrm{g\,cm^{-2}}$ and the radius of a central density plateau $r_0 = 0.154$ pc. They are chosen so that a gravitationally unstable core has the initial mass $M_\mathrm{c} = 26240\ \mathrm{M_\odot}$ and the ratio of rotational to gravitational energy $\beta = 1.96 \times 10^{-2}$. Although the initial cloud mass is lower than that assumed for the direct collapse model where a SMS exceeding $10^5\ \mathrm{M_\odot}$ may ultimately form, the mass is sufficient to follow the protostellar evolution for the first $\sim 10^5$ yr.

The numerical simulations are run on a grid of a polar coordinate (r, ϕ) with 512×512 spatial zones. The radial points are logarithmically spaced to increase a numerical resolution of the inner grid, where the disk forms and evolves. The innermost cell outside the central sink cell has a radius $R_\mathrm{sc} + 1.6$ AU. The radial and azimuthal resolutions are ~ 14 AU at a radius of $r = 1000$ AU and ~ 70 AU at $r = 5000$ AU. These resolutions are sufficient to fulfill the Truelove criterion which describes that the local Jeans length must be resolved with at least four numerical cells (Truelove et al. 1997). For a thin self-gravitating disk, the Jeans length can be written as (Vorobyov, DeSouza & Basu 2013)

$$R_\mathrm{J} = \frac{\overline{c_\mathrm{s}}^2}{G\overline{\Sigma}}. \tag{3.5}$$

With the mean surface density of $\overline{\Sigma} \simeq 500\ \mathrm{g\,cm^{-2}}$ and the mean temperature $\overline{T} \simeq 7500$ K, which are typical for our disk at $r = 1000 - 5000$ AU, the Jeans length is $R_\mathrm{J} \simeq 550$ AU and is resolved by ~ 40 grid zones at $r = 1000$ AU and ~ 8 grid zones at $r = 5000$ AU in each direction (r, ϕ).

3.2.2 Stellar evolution calculations

We use a stellar evolution code STELLAR which is originally developed by Yorke & Bodenheimer (2008) and is used in the study of Chapter 2. Since we have described the detail of the code in Section 2.2.1, here we briefly explain the main features of the code.

In the code, the basic equations of stellar evolution are solved with effects of mass accretion. We consider nuclear reactions up to helium burning (3α and $\{\mathrm{CNO}\} + \mathrm{He}$). Energy transport by convection is modeled by a mixing length theory.

We use a gray atmosphere boundary condition for the stellar surface layer where accreted gas accumulates. The accreted gas mass $\dot{M}_* \Delta t$ is added to the outermost grid cell in each time step, where $\dot{M}_*$ is the accretion rate and Δt is the time step of the calculation. Physical quantities of the accreted gas are assumed to be the same as those of the outermost grid point. This treatment approximates an extreme case in which accreting gas has time to adjust thermally to the stellar surface and slowly lands on to the star. This is not always the case, however, because the gas can accrete with more thermal energy. The additional energy is taken into account by parametrizing the fraction of accretion luminosity deposited in the stellar surface layer,

$$\eta \equiv \frac{L_{*,acc}}{L_\mathrm{acc}} = L_{*,\mathrm{acc}} \left(\frac{GM_* \dot{M}_*}{R_*} \right)^{-1}, \tag{3.6}$$

where $L_{*,\mathrm{acc}}$ is the part of the accretion luminosity which directly contributes to the stellar luminosity and affects the stellar internal structure. As shown in Hosokawa et al. (2013), the parameter η has a minor effect on stellar evolution for high accretion rates $\gtrsim 0.1\ M_\odot\,\mathrm{yr}^{-1}$ except the earliest accretion phases. We choose $\eta = 0.1$ in our calculations.

As the initial condition, we set a polytrope star of 2 $\mathrm{M}_\odot$ with a polytropic index $n = 1.5$, which approximates a fully convective star. Before calculation of stellar mass growth, we first relax the polytrope star to a fully converged stellar model. The stellar composition is set to be pristine with $X = 0.72$ and $Y = 0.28$. The accretion history is taken from the 2D hydrodynamical simulation of Section 3.2.1.

3.3 Results

3.3.1 Episodic accretion with self-gravitating disks

We describe the evolution of a circumstellar disk which forms as a result of the gravitational collapse of the massive primordial core. Figure 3.2 shows the time evolution of the gas surface density in the inner 20000×20000 AU^2 box. The total simulation box is about 100 times larger in area than displayed in Figure 3.2. The time shown in each panel is the elapsed time since the formation of the star which is schematically denoted by the red circles at the center. Evidently, the disk around the star is strongly gravitationally unstable and quickly forms giant spiral arcs. Within the arcs, gravitationally bound and pressure supported clumps form via fragmentation due to the gravitational instability.

We analyze the properties of the fragments in a post-process manner, using the method described in Vorobyov, DeSouza & Basu (2013). The algorithm is based on two conditions. The first one is that the fragment must be pressure supported with a negative pressure gradient with respect to the fragment center. The second condition dictates that the fragment must be held together by gravity, with a positive gradient of the gravitational potential from the fragment center where the potential well is deepest.

The top panel of Figure 3.3 shows the time evolution of the number of fragments in the disk. The number of fragments increases with time from a few tens just after the formation of the central star to more than a hundred by the end of the simulations. The increase is not steady but is characterized by both rises and drops, which implies that the fragments can be both created and lost. One of the loss channels is accretion of the fragments on to the star. The accretion occurs when the fragments lose the angular momentum due to gravitational interaction with other fragments and spiral arcs (e.g., Vorobyov, DeSouza & Basu 2013). Such accretion of the fragments causes the strong increase of the accretion rate featuring the episodic accretion.

The number of fragments and their formation rate is roughly 10 times greater than those for the normal Pop III case. The increase of the number of fragments is attributed to the specific density-temperature relation typical for the direct collapse case. The red line in Figure 3.1 demonstrates that there is a wide range of gas densities $\lesssim 10^{16}$ cm^{-3} for which the gas temperature decreases with increase of the density. A density increase by any compression therefore leads to a temperature decrease which promotes further compression and ultimately fragmentation.

The bottom panel of Figure 3.3 represents the normalized distribution function of fragment masses. The distribution is calculated using all fragments identified in the top panel. Since the time interval of sampling in the top panel is 500 yr, some long-lived fragments are duplicated and the distribution function is accordingly skewed. The fragments have various masses from a sub-solar mass to several hundred solar masses.

In our simulations, some of the fragments may be ejected out of the disk by multibody interactions. Several candidates of the escaping fragments are highlighted in Figure 3.2 by the yellow circles. Provided that they can acquire sufficient velocities to escape the gravitational pull of the star and

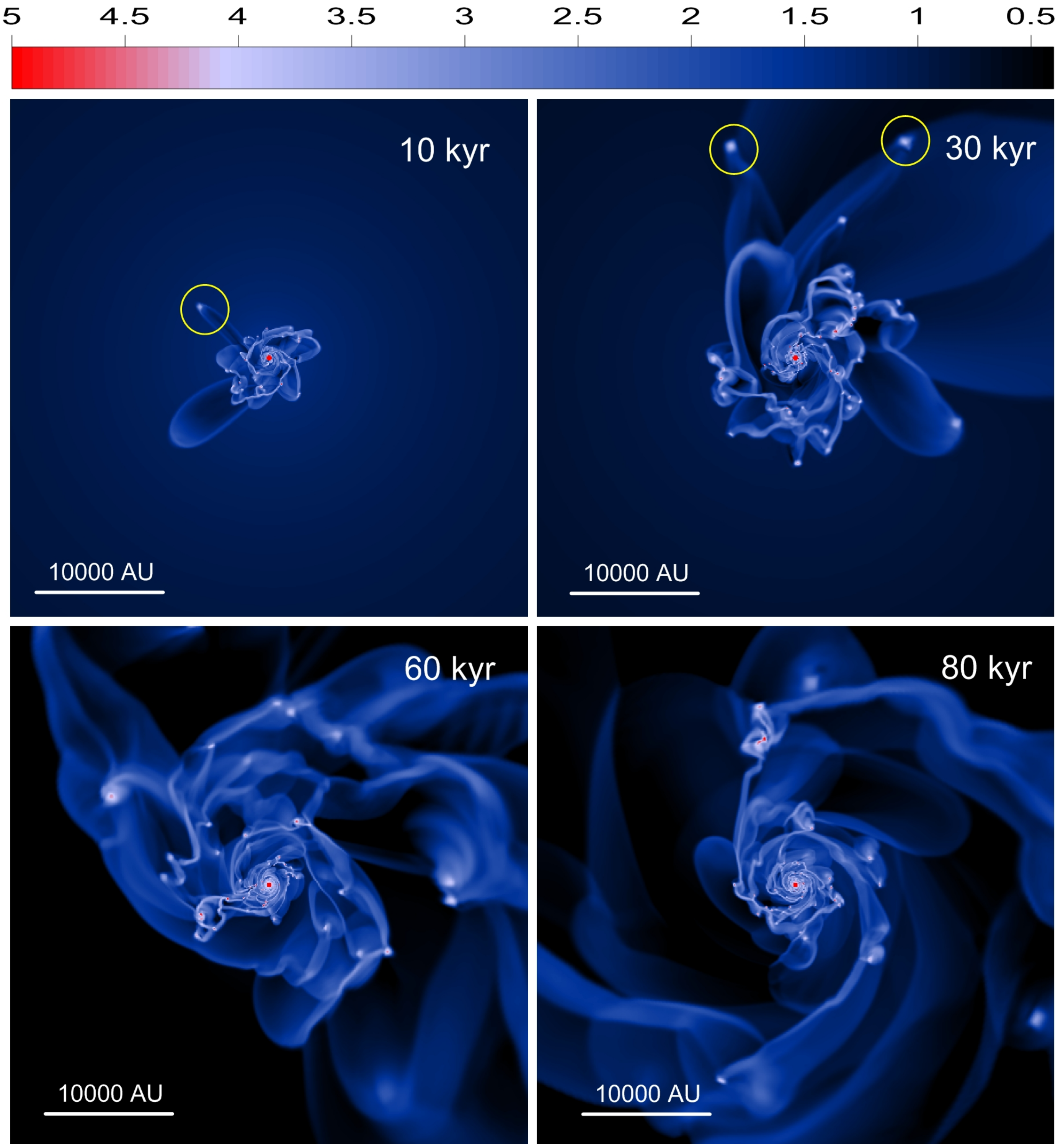

Fig. 3.2 Gas surface density of the disk around the rapidly growing protostar in the inner 20000×20000 AU^2 box. The star is schematically denoted as red circles in the center. The elapsed time from the formation of the star is shown in each panel. The yellow circles indicate the fragments which are ejected from the disk. The color bar shows dex values of the surface density in g cm^{-2}. This figure is reproduced from Sakurai et al. (2016).

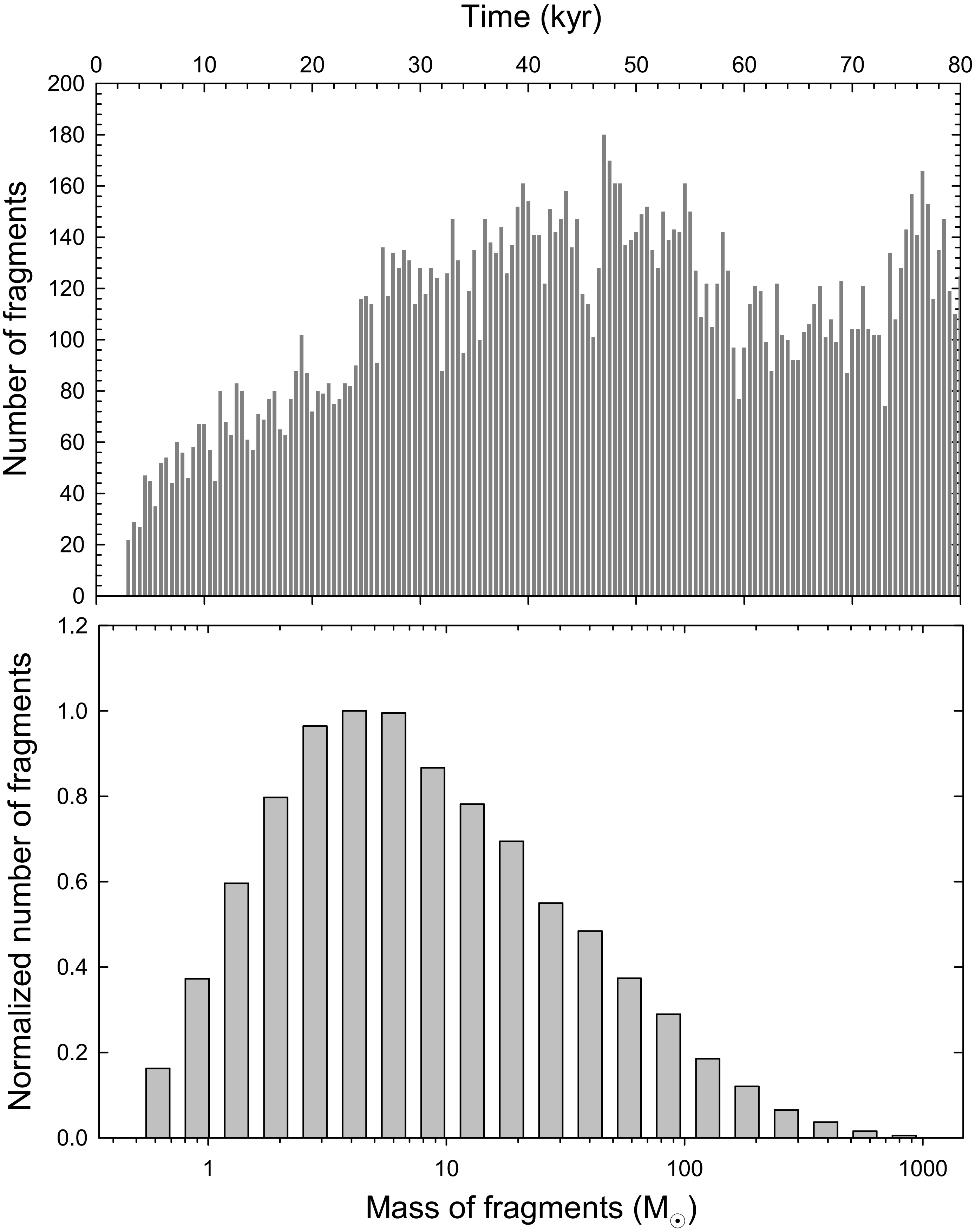

Fig. 3.3 Top: the number of fragments in the disk as a function of the elapsed time from the formation of the central protostar. Bottom: the distribution function of masses of the fragments at all times. This figure is reproduced from Sakurai et al. (2016).

disk system, they will become freely-floating primordial stars.

We compare the variable accretion histories for the direct collapse case with that for the normal Pop III case, focusing on the duration of quiescent phases of accretion $\Delta t_{\rm q}$. We define the quiescent phases for the direct collapse case as phases when the accretion rate is below the critical rate $0.04\ M_\odot\,{\rm yr}^{-1}$ above which the star becomes 'supergiant' (Section 1.2.1). For the normal Pop III case, the quiescent phases are defined as phases when the accretion rate falls below one tenth of the average value. The definition is analogous to that for the direct collapse case since the critical accretion rate $0.04\ M_\odot\,{\rm yr}^{-1}$ is $\sim 0.1\times$ the average accretion rate for the direct collapse case.

In Figure 3.4, we show the evolution of the accretion histories for the direct collapse case (top panel) and for the Pop III case (bottom panel) by the blue lines, with the threshold accretion rate $\dot{M}_{\rm th}$ below which the accretion is deemed quiescent (black dashed line). For each panel, we also show the time-averaged accretion histories with smoothing bins of $\Delta t_{\rm bin} = 1000$ and 100 yr (red and green lines). When averaging over $\Delta t_{\rm bin}$, all variations shorter than $\Delta t_{\rm bin}$ are blurred. Thus, if the accretion rate averaged over $\Delta t_{\rm bin}$ exceeds the threshold rate $\dot{M}_{\rm th}$, the duration of the quiescent phase $\Delta t_{\rm q}$ is less than $\Delta t_{\rm bin}$. For the direct collapse case, the typical duration of the quiescent phases is much smaller than 1000 yr in the early phase $\lesssim 0.06$ Myr, since the red line never falls below the black line and the green line seldom drops below it. The relatively long quiescent phases of $\Delta t_{\rm q} \sim 1000$ yr only appear in the late evolutionary stages $\gtrsim 0.06$ Myr, due to gradual depletion of the envelope mass and associated weakening of fragmentation in the disk. In contrast, for the Pop III case the quiescent phases are much longer $\Delta t_{\rm q} \gtrsim 10^3$ yr until the end of the simulation.

We attribute the difference of $\Delta t_{\rm q}$ to the difference of the time intervals of disk fragmentation. Since the disk in the direct collapse case is more unstable than that in the normal Pop III case, the disk fragmentation is also more efficient and the infalling rate of fragments is greater, resulting in the shorter duration of the quiescent phases. To see the difference of the disk gravitational stability, we use the Toomre Q parameter (Toomre 1964) which is an estimator of the gravitational instability. The Q parameter for the accretion stage of star formation is approximately given by $Q \sim \mathcal{O}(0.1-1) \times (T_{\rm disk}/T_{\rm env})^{3/2}$ (see equation 19 of Tanaka & Omukai 2014), where $T_{\rm disk}$ and $T_{\rm env}$ are temperatures of the disk and surrounding envelope. We can see that the disk is more gravitationally unstable at a smaller Q value when $T_{\rm disk}$ is smaller than $T_{\rm env}$. As is surmised from Figure 3.1, such a temperature imbalance can occur for the direct collapse case if the number density is $\lesssim 10^{16}\ {\rm cm}^{-3}$. In our 2D simulation, the number density at the boundary between the disk and envelope is $\sim 10^6$ to $10^9\ {\rm cm}^{-3}$ and $T_{\rm disk}$ is slightly smaller than $T_{\rm env}$. By contrast, the imbalance of the temperature is opposite for the normal Pop III case, where the temperature is an increasing function of the number density for $\gtrsim 10^5\ {\rm cm}^{-3}$. The disk in this case is thus less unstable, which explains the longer duration of the quiescent phases $\Delta t_{\rm q}$.

In Figure 3.5, we present the azimuthally averaged gas surface density and volume density as a function of radial distance from the star for two evolutionary times at 10 and 60 kyr. Whereas low mass fragments and spiral arcs are smoothed out by azimuthal averaging, the existence of massive fragments is apparent by the multiple peaks in the density distributions. The black circles indicate the position of the disk outer edge which is defined visually assuming that fragments form within the disk and not within the infalling parental core. We note that the application of a more sophisticated disk tracking method (Dunham, Vorobyov & Arce 2014) is difficult for the highly unstable and fragmenting disk. The black dotted lines are the least-square fits to the surface density profiles. The corresponding relations at 10 and 60 kyr by ${\rm g\,cm^{-2}}$ are

$$\Sigma = 10^{6.7\pm0.2}\left(\frac{r}{\rm AU}\right)^{-1.4\pm0.06}, \tag{3.7}$$

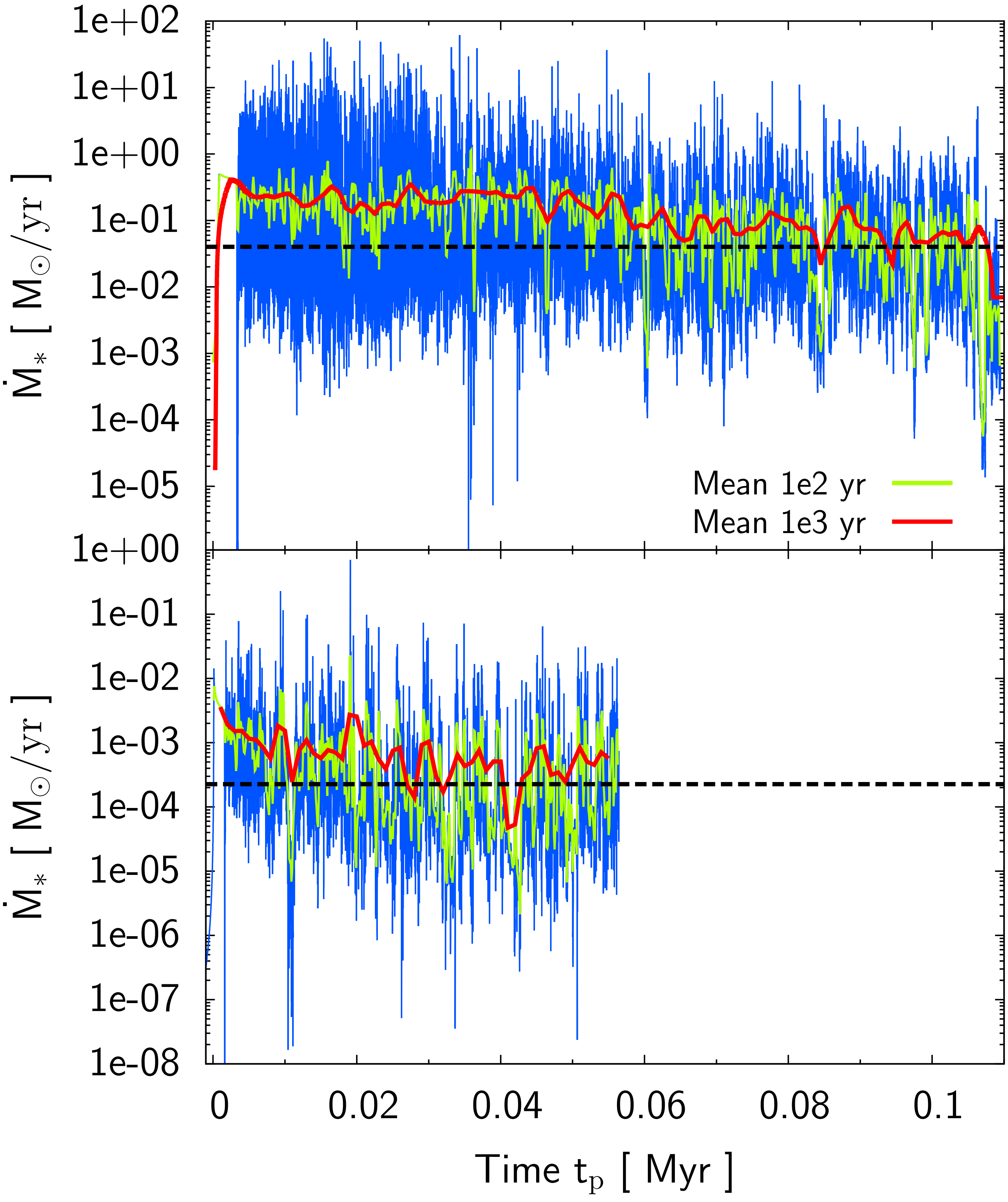

Fig. 3.4 Top: the accretion history for the direct collapse case in the 2D simulation. The time is the elapsed time from the formation of the protostar. The blue line represents the accretion history without time averaging. The red and green lines depict the time-averaged accretion histories with bins of $\Delta t_{\rm bin}$ = 1000 and 100 yr respectively. The black dashed line denotes the threshold accretion rate $\dot{M}_{\rm th}$ below which the accretion is in a quiescent phase (see text). Bottom: the accretion history for the Pop III case which is taken from the simulation of Vorobyov, DeSouza & Basu (2013). This figure is reproduced from Sakurai et al. (2016).

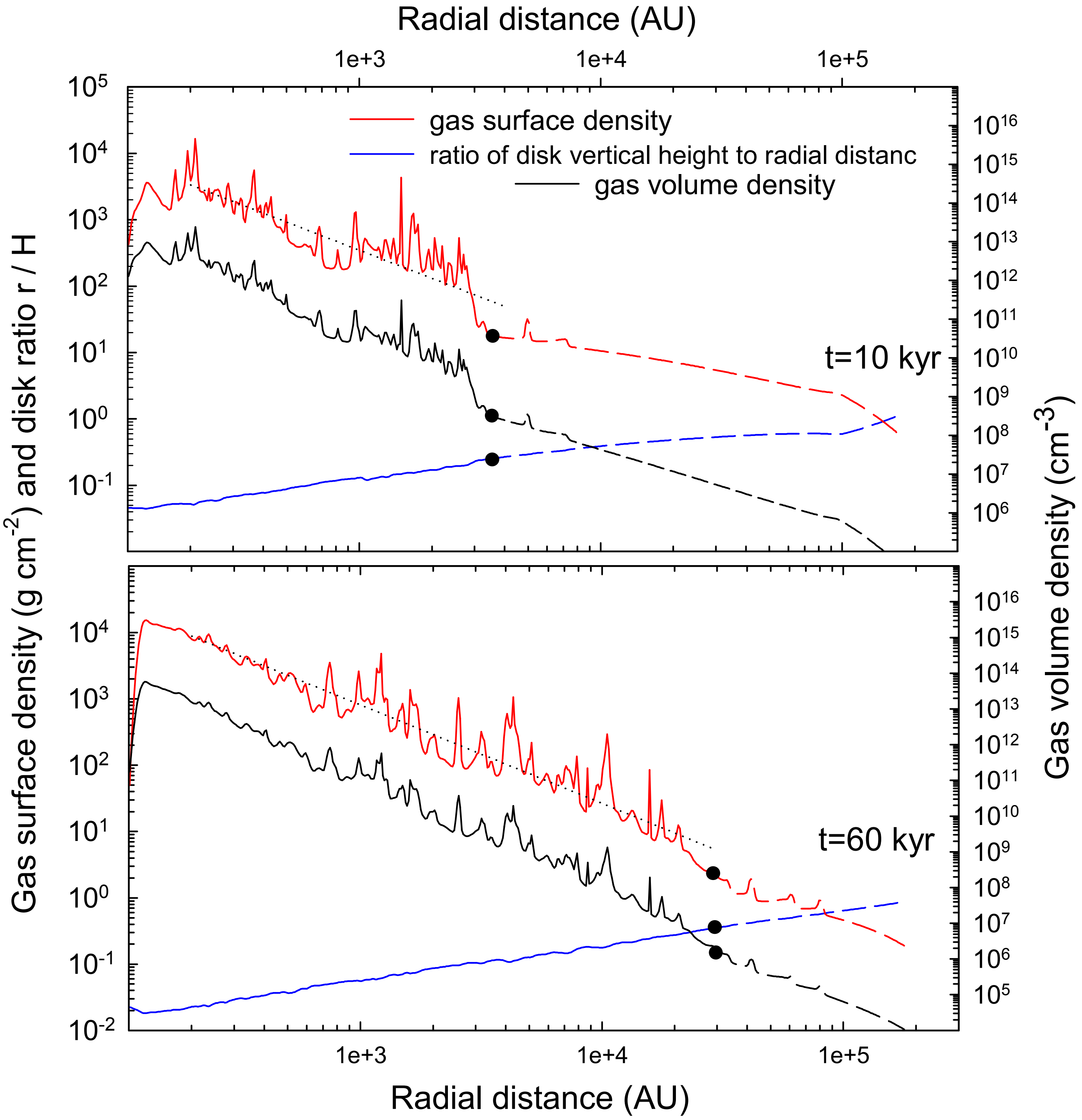

Fig. 3.5 Azimuthally averaged gas surface and volume density profiles (red and black lines) at two evolutionary times after the formation of the star. The black circles represent the position of the disk outer edge. The black dotted lines show the least-square fits to the gas surface density profiles, which follow approximately a power law relation of $r^{-1.5}$. The blue lines denote the local aspect ratio of the disk. The outside regions of the disk are depicted by the dashed lines. This figure is reproduced from Sakurai et al. (2016).

$$\Sigma = 10^{7.4\pm0.1}\left(\frac{r}{\mathrm{AU}}\right)^{-1.5\pm0.02} . \tag{3.8}$$

The surface density profiles follow approximately a power law relation $r^{-1.5}$ which is typical for self-gravitating disks around Pop III stars. The blue lines represent the ratio of disk vertical scale height to distance from the central star. This quantity apparently stays well below unity everywhere in the disk, justifying the assumption of the thin-disk approximation.

3.3.2 Stellar evolution via episodic mass accretion

We here consider the evolution of the central protostar via the variable mass accretion history obtained in the 2D hydrodynamical simulation (Section 3.3.1). The top panel of Figure 3.4 shows the accretion rate (blue line) used in the stellar evolution calculation. The mean accretion rate is $0.1-0.3\ M_\odot\,\mathrm{yr}^{-1}$, which is expected for the direct collapse model. The top panel of Figure 3.6 shows the evolution of the stellar mass and the stellar radius. Despite the frequent drops of the accretion rate below the critical rate $0.04\ M_\odot\,\mathrm{yr}^{-1}$, which could in principle allow stellar contraction, the protostellar radius increases almost monotonically until the end of the computation. The stellar radius finally reaches 100 AU which is only slightly below the sink radius 110 AU. We show in the bottom panel of Figure 3.6 the evolution of ionizing photon emissivity. We find that the ionizing photon emissivity remains insufficient for creating an H II region, since the effective temperature is fixed to ~ 5000 K which is too low to ionize gas. The temperature ~ 5000 K is determined due to the very sensitive temperature dependence of the H^- opacity. Overall, the evolution is similar to that with constant accretion rates of $\gtrsim 0.1\ M_\odot\,\mathrm{yr}^{-1}$ (black dashed line in Figure 2.1).

The absence of stellar contraction during the quiescent phases in our current simulation is attributed to long thermal time compared to the length of the quiescent phases Δt_q. In Chapter 2, we have found that, in order for the protostar to circumvent stellar contraction and remain to be supergiant, the length of quiescent phases Δt_q has to be shorter than the surface KH time $t_\mathrm{KH,surf}$ of equation (2.9). The surface KH timescale $t_\mathrm{KH,surf}$ is used instead of the usual global definition $t_\mathrm{KH} = GM_*^2/R_*L_*$, because mass distribution of the bloated protostar is highly inhomogeneous, namely, only a surface layer with a very small fraction of the total mass inflates to cover most of the stellar radius. (see Section 2.3.2.1 and Figures 2.5 and 2.6). The surface KH time is approximately written as

$$t_\mathrm{KH,surf} \simeq 10 t_\mathrm{KH} \simeq 1000\ \mathrm{yr} \left(\frac{M_*}{500\ \mathrm{M}_\odot}\right)^{1/2}. \tag{3.9}$$

Since the length of the quiescent phases in our simulation Δt_q is shorter than this time scale $t_\mathrm{KH,surf}$ in all epoch, the bloated surface layer does not have enough time to commence contraction by radiating away thermal energy. Even for the late evolutionary stage $\gtrsim 0.06$ Myr when the quiescent phases has long duration of $\Delta t_\mathrm{q} \sim 10^3$ yr, the star does not contract because $t_\mathrm{KH,surf}$ increases to $\gtrsim 1000$ yr with growth of the stellar mass.

To evaluate the strength of UV feedback, a critical value of ionizing photon emissivity $S_\mathrm{min} = \dot{M}/\mu m_\mathrm{H}$ is used (see Section 2.4.1), which is the value to ionize once all of the atoms accreting on to the star. S_min is the lower limit to form an H II region in spherical geometry since, in reality, additional UV photons are necessary to ionize recombined atoms. Although a H II region could expand into the polar directions from which little mass accretion occurs, the very low UV flux ensures that the envelope will be hardly affected by ionization. In the bottom panel of Figure 3.6, we also show the evolution of S_min, for which the averaged accretion history with $\Delta t_\mathrm{bin} = 1000$ yr is used. The UV emissivity is always much smaller than S_min and thus no significant H II region will emerge to halt the mass accretion.

3.4 Conclusion and Discussion

We have studied the evolution of a growing SMS via variable mass accretion caused by a self-gravitating circumstellar disk. The 2D hydrodynamical simulation gives evidence of strong dynamic

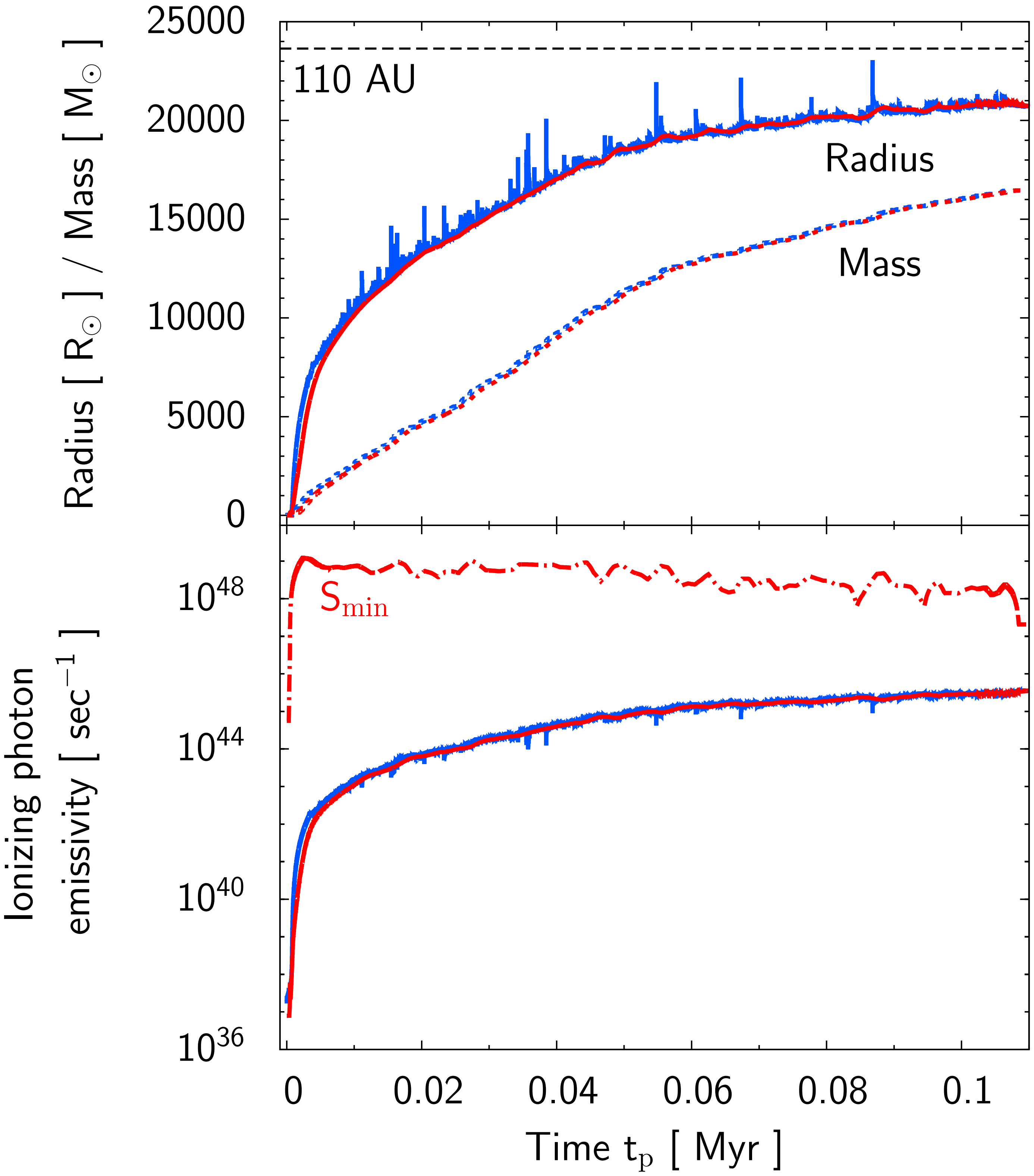

Fig. 3.6 The evolution of stellar mass and radius (top panel) and ionizing photon emissivity (bottom panel). The evolutions with the original accretion rate and with the time-averaged accretion rate of $\Delta t_{\rm bin} = 1000$ yr are shown by the blue and red lines respectively. The sink radius size 110 AU is denoted by the black dashed line. The critical ionizing photon emissivity above which an H II region will appear is plotted by the red dot-dashed line (see Section 2.4.1). This figure is reproduced from Sakurai et al. (2016).

features of the disk and stellar accretion; fragmentation easily occurs in the disk and the fragments then migrate inward to fall on to the star. The obtained accretion history is highly time-dependent, presenting a number of short accretion bursts followed by somewhat longer quiescent phases. Despite the high variability of the accretion rate, the stellar evolution resembles that for the constant accretion case, namely, the stellar radius monotonically increases with the growth of the stellar mass. The effective temperature keeps almost constant at $\simeq 5000$ K, at which the star emits the negligible amount of UV photons. The KH contraction during the quiescent accretion phases does not occur because their duration is short $\Delta t_{\rm q} \lesssim 1000$ yr. The duration is shorter than the local KH time scale for the inflating stellar surface layer of equation (3.9). In this situation, the surface layer can only insufficiently radiate away thermal energy during the short quiescent phases and thus the star does not commence the stellar contraction to leave the supergiant protostar stage.

3.4.1 Caveats to the numerical treatments

In the current work, we have simulated the evolution until the stellar mass reaches $\simeq 1.6 \times 10^4$ M$_\odot$ (top panel of Figure 3.6). The final mass is limited by our adopted initial conditions, in particular, the limited cloud mass of $\simeq 2.6 \times 10^4$ M$_\odot$. We could simulate a longer evolution up to higher stellar masses by assuming a higher initial cloud mass. We nevertheless focus on capturing variability during the early evolutionary stages of protostellar accretion, because the surface KH time scale is shorter when the stellar mass is low, $t_{\rm KH,surf} \sim 10^3$ yr$(M_*/10^3$ M$_\odot)^{1/2}$.

We note that with the adopted sink size 110 AU, the disk first appears only after the stelar mass reaches $\simeq 1000$ M$_\odot$. A test case with a 70 AU sink shows that the disk and resulting variability of the accretion appear earlier from $M_* \simeq 700$ M$_\odot$, at which $\Delta t_{\rm q}$ is still lower than 100 yr as in the case with a sink size 110 AU. Thus, we do not currently expect stellar contraction to occur in the early evolutionary stages, a fact which needs to be checked by further simulations. Note that the smaller sink has not beed adopted because the SMS radius is as large as $\gtrsim 100$ AU and would soon exceed the sink size.

The top panel of Figure 3.4 shows that the length of some quiescent phases becomes longer for $\gtrsim 0.06$ Myr due to gradual depletion of the accretion envelope, i.e., stabilization of the disk. For more realistic cases, where significantly more massive clouds form in atomic-cooling halos, the mass depletion would be postponed to even later evolutionary times.

We note possible dimensional effects in a realistic three-dimensional disk. Fragments which form in a 3D disk can interact with the central star and other fragments in a complex manner. Unlike in our 2D simulation where fragments simply move either inward or outward, dynamical interactions of fragments would induce more stochastic mass accretion. However, the resulting dynamics in our 2D simulation is overall consistent with that in 3D simulations, where most fragments migrate towards the star (Cha & Nayakshin 2011, Machida, Inutsuka & Matsumoto 2011, Greif et al. 2012). It will be necessary to perform three dimensional simulations to study explicitly the impact of fragmentation to SMS formation.

3.4.2 Analytical estimation of the length of quiescent phases

In order to examine whether $\Delta t_{\rm q}$ is sufficiently short for *all* evolutionary stages to suppress stellar contraction, we analytically estimate the duration of quiescent phases $\Delta t_{\rm q}$. We expect that $\Delta t_{\rm q}$ is controlled by two time scales: a fragmentation time scale $t_{\rm frag}$ and a migration time scale $t_{\rm mig}$. The former is the time scale for a fragment to form in a gravitationally unstable disk. The latter is the time scale for a newly formed fragment to migrate inward to fall on to the central star. If $t_{\rm frag} < t_{\rm mig}$, the length of quiescent phases will be typically in the range $t_{\rm frag} \lesssim \Delta t_{\rm q} \lesssim t_{\rm frag} + t_{\rm mig} \sim t_{\rm mig}$. In this case, there would be many fragments in the disk. The minimum duration time will be realized when fragments form at regular time intervals and migrate successively. Conversely, if $t_{\rm frag} > t_{\rm mig}$, the length will be $\Delta t_{\rm q} \sim t_{\rm frag} + t_{\rm mig} \sim t_{\rm frag}$.

We estimate the fragmentation time using the maximum growth rate $\omega_{\rm max}$ of gravitational instability in a linear theory (Shu 1992),

$$t_{\rm frag} = \frac{2\pi}{\omega_{\rm max}} = \frac{2\pi}{\Omega\sqrt{1-Q^2}} \sim \frac{2\pi}{\Omega}, \tag{3.10}$$

where Ω is the angular velocity and Q is the Toomre parameter. The rate $\omega_{\rm max}$ is the rate for the wavenumber $k_{\rm max} = \Omega^2/\pi G\Sigma$. In the last term, Q is assumed to be sufficiently small. For $t_{\rm mig}$, since fragments lose their angular momentum through the interaction with spiral arms in the simulation, we use the so-called Type I migration time scale (Tanaka, Takeuchi & Ward 2002, Inayoshi & Haiman 2014),

$$t_{\rm mig} = \frac{1}{4qC\mu}\left(\frac{H}{r}\right)^2 \frac{2\pi}{\Omega}, \tag{3.11}$$

where $q = M_{\rm f}/M_*$, $C = 1.160 + 2.828\alpha \sim 5.402$, $\mu = \pi\Sigma r^2/M_*$, $H = c_{\rm s}/\Omega$, $M_{\rm f}$ is a fragment mass, $\alpha \simeq 1.5$ is a power index of the surface density (see Figure 3.2). The mass of fragments is estimated to be

$$M_{\rm f} = \pi\lambda_{\rm max}^2\Sigma, \tag{3.12}$$

where $\lambda_{\rm max} = 2\pi/k_{\rm max}$.

To assess the two time scales, we assume $\Omega \sim 0.5\Omega_{\rm Kep}$ which is the value found in our simulation, where $\Omega_{\rm Kep} \sim \sqrt{GM(<r)/r^3}$ is the Kepler angular velocity and $M(<r)$ is the enclosed mass,

$$M(<r) = M_* + \int_{\rm r_0}^{r} \Sigma 2\pi r {\rm d}r. \tag{3.13}$$

The lower limit of the integration r_0 is the adopted sink radius 110 AU. We use $\Sigma = \Sigma_0(r/r_0)^{-1.5}$, where Σ_0 is the surface density at r_0. In the disk regions, $M(<r) \simeq M_*$ according to our simulation and thus the fragment mass and the two time scales are

$$M_{\rm f} = 14\ {\rm M_\odot}\left(\frac{\Sigma_0}{10^4\ {\rm g\,cm^{-2}}}\right)^3 \left(\frac{M_*}{10^4\ {\rm M_\odot}}\right)^{-2} \left(\frac{r}{10^3\ {\rm AU}}\right)^{3/2}, \tag{3.14}$$

$$t_{\rm frag} = 6.3\times10^2\ {\rm yr}\left(\frac{M_*}{10^4\ {\rm M_\odot}}\right)^{-1/2} \left(\frac{r}{10^3\ {\rm AU}}\right)^{3/2}, \tag{3.15}$$

$$t_{\rm mig} = 2.2\times10^4\ {\rm yr}\left(\frac{\Sigma_0}{10^4\ {\rm g\,cm^{-2}}}\right)^{-4} \left(\frac{T}{8000\ {\rm K}}\right) \left(\frac{M_*}{10^4\ {\rm M_\odot}}\right)^{5/2} \left(\frac{r}{10^3\ {\rm AU}}\right)^{1/2}. \tag{3.16}$$

The fragment mass of equation (3.14) is in good agreement with the typical mass $1-10\ {\rm M_\odot}$ (bottom panel ofFigure 3.3).

Since we get the specific formulae of the two time scales, we can now estimate the duration of quiescent phases $\Delta t_{\rm q}$, which is assessed within the disk $r < r_{\rm disk}$ where fragmentation occurs. For $r <\lesssim r_{\rm disk}$, we find that $t_{\rm frag} \lesssim t_{\rm mig}$ at least at 10 kyr and 60 kyr. If we assume that $t_{\rm frag} < t_{\rm mig}$ is always realized in the disk, the minimum length of quiescent phases $\Delta t_{\rm q,min}$ will be comparable to $t_{\rm frag}$. For the early evolutionary stages of $M_* \lesssim 10^4\ {\rm M_\odot}$ and $r \lesssim r_{\rm disk}$, we see $\Delta t_{\rm q,min} \sim t_{\rm frag} \lesssim$

10^3 yr, which is consistent with our rough estimate of $\Delta t_{\rm q}$ in Section 3.3.1. For $M_* \gtrsim 10^4$ $\mathrm{M_\odot}$, $\Delta t_{\rm q}$ can become even shorter since $t_{\rm frag} \propto M_*^{-1/2}$, if the disk continues to be unstable with an ample gas supply and the assumption of $Q \ll 1$ is valid in equation (3.10). Although the gas supply becomes limited for $M_* \gtrsim 10^4$ $\mathrm{M_\odot}$ in our simulation, it would be ample if we use a more realistic heavier initial cloud. Overall, we expect that $\Delta t_{\rm q} \lesssim 10^3$ yr $\lesssim t_{\rm KH,surf}$ and there will be no significant stellar contraction for any SMS mass, until the stellar mass reaches $\sim 10^5$ $\mathrm{M_\odot}$. At this point, the SMS is expected to collapse and leave a massive BH via general relativistic instability.

3.4.3 Stellar evolution of fragments and UV feedback

It is often suspected that fragments which form in the disk may become zero-age main sequence (ZAMS) stars before destruction. The ZAMS stars will emit UV photons and UV feedback can occur.

Several studies consider fragmentation and clump migration in a disk around a SMS by using analytical models (Lodato & Natarajan 2006, Inayoshi & Haiman 2014, Latif & Schleicher 2015). Inayoshi & Haiman (2014) and Latif & Schleicher (2015) show that fragments fall on to the central star before they become ZAMS stars when $M_* \lesssim 10^4$ $\mathrm{M_\odot}$. The rapid fall is attributed to the shorter migration time scale than the KH time scale of the fragments $t_{\rm KH} = GM_{\rm f}^2/R_{\rm f}L_{\rm f}$, where $R_{\rm f}$ and $L_{\rm f}$ are a radius and luminosity of fragments. Conversely, for $M_* \gtrsim 10^4$ $\mathrm{M_\odot}$, the groups argue that fragments can become ZAMS stars.

Following the previous works, we discuss whether UV feedback from fragments is plausible. We first estimate the KH time scale of the fragments. As seen in figure 4 of Hosokawa & Omukai (2009a), if the accretion rate of fragments $\dot{M}_{\rm f} \lesssim 10^{-2}$ $M_\odot\,\mathrm{yr}^{-1}$, the KH time scale $t_{\rm KH}$ is comparable to or larger than an accretion time scale $t_{\rm acc} = M_{\rm f}/\dot{M}_{\rm f}$ before the fragment reaches ZAMS. The lower limit of KH time is then estimated by the accretion time scale $t_{\rm acc}$ (Inayoshi & Haiman 2014)

$$t_{\rm KH} \gtrsim t_{\rm acc} \sim 10^4\ \mathrm{yr} \left(\frac{M_{\rm f}}{30\ \mathrm{M_\odot}}\right)\left(\frac{\dot{M}_{\rm f}}{0.003\ M_\odot\,\mathrm{yr}^{-1}}\right)^{-1}. \tag{3.17}$$

The accretion rate of fragments $\dot{M}_{\rm f}$ is

$$\dot{M}_{\rm f} = \frac{3}{2}\Sigma\Omega(f_{\rm H}R_{\rm H})^2, \tag{3.18}$$

where $R_{\rm H} = r(M_{\rm f}/3M_*)^{1/3}$ is the Hill radius and the factor $f_{\rm H}$ is $\mathcal{O}(1)$ (Goodman & Tan 2004). With $f_{\rm H} = 1$, the approximate form is derived

$$\dot{M}_{\rm f} = 3.6 \times 10^{-3}\ M_\odot\,\mathrm{yr}^{-1}\left(\frac{\Sigma_0}{10^4\ \mathrm{g\,cm^{-2}}}\right)^3\left(\frac{M_*}{10^4\ \mathrm{M_\odot}}\right)^{-3/2}. \tag{3.19}$$

Using equations (3.14) and (3.19), the KH time in equation (3.17) becomes

$$t_{\rm KH} \gtrsim 3.9 \times 10^3\ \mathrm{yr}\left(\frac{r}{10^3\ \mathrm{AU}}\right)^{3/2}\left(\frac{M_*}{10^4\ \mathrm{M_\odot}}\right)^{-1/2}. \tag{3.20}$$

The ratio of $t_{\rm mig}$ to $t_{\rm KH}$ is then calculated

$$\frac{t_{\rm mig}}{t_{\rm KH}} \lesssim 5.7\left(\frac{\Sigma_0}{10^4\ \mathrm{g\,cm^{-2}}}\right)^{-4}\left(\frac{M_*}{10^4\ \mathrm{M_\odot}}\right)^3\left(\frac{r}{10^3\ \mathrm{AU}}\right)^{-1}\left(\frac{T}{8000\ \mathrm{K}}\right). \tag{3.21}$$

We can see that the migration time $t_{\rm mig}$ becomes smaller than $t_{\rm KH}$ when $M_* \lesssim 10^4\ \mathrm{M}_\odot$. This discussion is roughly consistent with the models of the other groups: for $M_* \lesssim 10^4\ \mathrm{M}_\odot$, UV feedback from fragments will be ineffective. There are, however, other mechanisms to be considered in order to examine the fate of the fragments. For such mechanisms, there are tidal disruption of fragments by the central star, interactions between fragments and possibly ejection. To assess the effect of UV feedback from fragments more correctly, 3D simulations including radiation are necessary in future studies.

Chapter 4

Black hole growth via hyper-Eddington accretion under super-Eddington luminosity

4.1 Overview

We perform 1D radiation hydrodynamical simulations in order to solve accretion flows on to massive black holes (BHs) with a high rate. By assuming that photon trapping limits luminosity emerging from the central region to $L \leq L_{\rm Edd}$, a previous work of Inayoshi, Haiman & Ostriker (2016) (hereafter IHO16) has shown that an accretion flow settles to a 'hyper-Eddington' solution, which is a steady and isothermal ($T \simeq 8000\,{\rm K}$) Bondi profile with $\gtrsim 5000$ times the Eddington accretion rate $\dot{M}_{\rm Edd} \equiv L_{\rm Edd}/c^2$. In this work, we address the possibility that accreting gas with finite angular momentum forms a bright nuclear accretion disk, with super-Eddington luminosity ($1 \lesssim L/L_{\rm Edd} \lesssim 100$). Combining our simulations with an analytical model, we show that a transition to steady hyper-Eddington accretion still occurs, as long as the emerging luminosity keeps $L/L_{\rm Edd} \lesssim 35(M_{\rm BH}/10^4\,{\rm M}_\odot)^{3/2}(n_\infty/10^5\,{\rm cm}^{-3})(T_\infty/10^4\,{\rm K})^{-3/2}(r_\star/10^{14}\,{\rm cm})^{-1/2}$, where n_∞ and T_∞ are the ambient gas density and temperature, and $r_\star$ is the photosphere radius, at which radiation emerges. When the luminosity exceeds this value, mass accretion becomes episodic. Our results can be recovered in a toy model of an optically thick spherical shell, which is driven by radiation force into a collapsing medium. If the central source is dimmer than the above critical value, the shell expansion is halted and reversed by ram pressure of the collapsing medium plus shell gravity. Our results show that rapid unimpeded hyper-Eddington accretion is possible even if luminosity emerging from the central source far exceeds the Eddington limit, and that the accretion can be either steady or strongly episodic.

4.2 Simulation method

4.2.1 Setup of the simulations

We solve structures of spherical accretion flows on to a BH of mass $M_{\rm BH}$ by performing 1D hydrodynamical simulations which include radiative processes. Figure 4.1 represents important physical scales of the gas structure. The Bondi radius is

$$R_{\rm B} = \frac{GM_{\rm BH}}{c_\infty^2} = 1.98 \times 10^{18}\,{\rm cm}\ M_{\rm BH,4}T_{\infty,4}^{-1}, \tag{4.1}$$

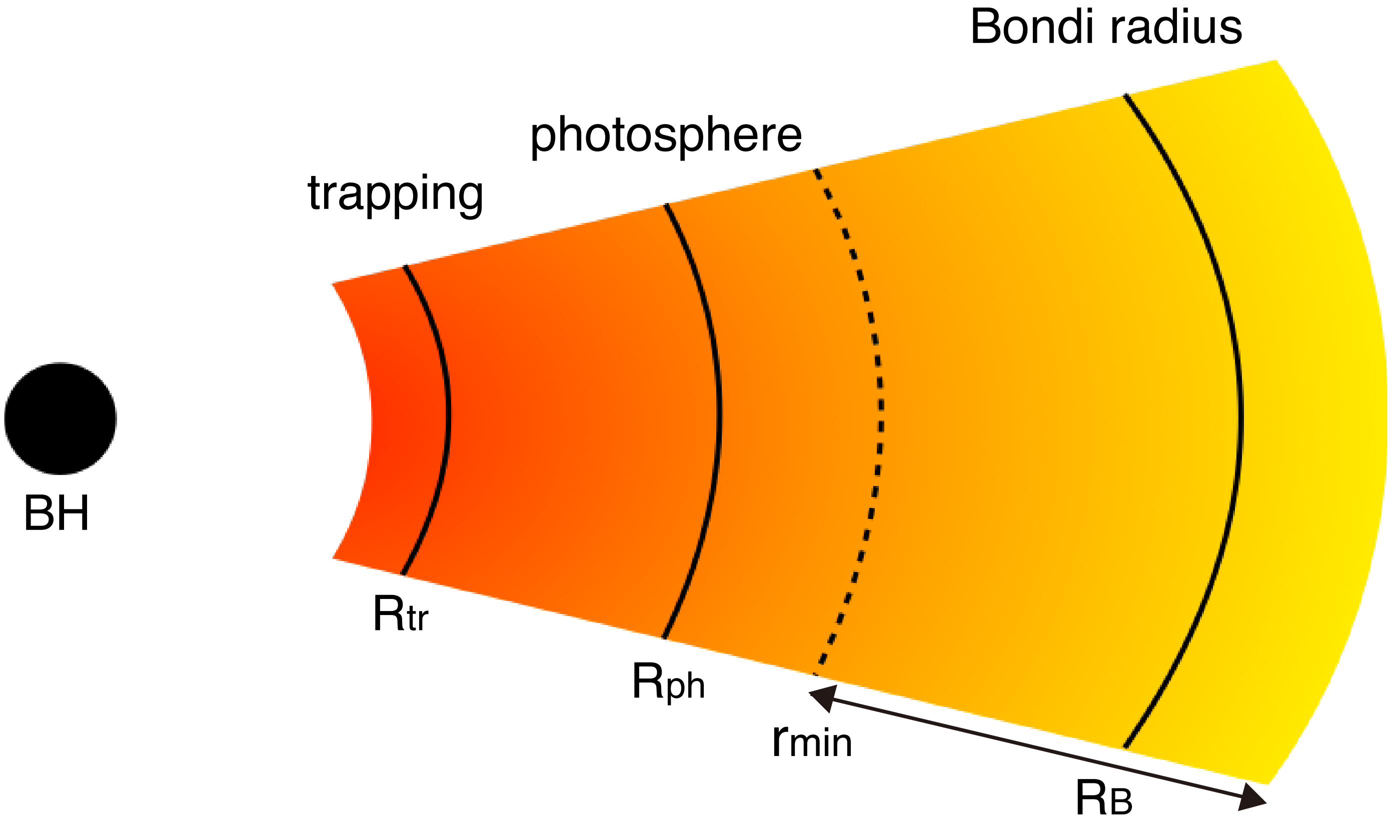

Fig. 4.1 Schematic picture of a spherically symmetric accretion flow on to a BH at a hyper-Eddington rate. The positions of the trapping radius $R_{\rm tr}$, the photosphere $R_{\rm ph}$ and the Bondi radius $R_{\rm B}$ are represented. Our simulations solve the structure of the accretion flow between $r_{\rm min}(\simeq 10^{-3}\,R_{\rm B}) \lesssim r \lesssim 10\,R_{\rm B}$. This figure is reproduced from Sakurai, Inayoshi & Haiman (2016).

within which the BH gravity overcomes the gas pressure and accretion begins. In this equations, $c_\infty = \sqrt{\frac{k_{\rm B}T_\infty}{\mu m_{\rm p}}}$ and T_∞ are a sound speed and gas temperature of ambient gas with the molecular weight for neutral gas $\mu = 1.23$. We use the normalizations of $M_{\rm BH,4} \equiv M_{\rm BH}/10^4\,{\rm M}_\odot$ and $T_{\infty,4} \equiv T_\infty/10^4\,{\rm K}$. A photosphere forms at $R_{\rm ph} \sim 10^{14-15}\,{\rm cm}$ (IHO16). The trapping radius is

$$R_{\rm tr} = \frac{\kappa_{\rm es}\dot{M}}{4\pi c} = 1.48\times10^{12}\,{\rm cm}\,M_{\rm BH,4}\dot{m}_3, \tag{4.2}$$

where $\kappa_{\rm es}$ is the electron scattering opacity and $\dot{M}$ is a mass accretion rate. We use the normalization $\dot{m}_3 \equiv (\dot{M}/\dot{M}_{\rm Edd})/10^3$, where $\dot{M}_{\rm Edd} \equiv L_{\rm Edd}/c^2$ and $L_{\rm Edd} \equiv 4\pi G M_{\rm BH}\mu_{\rm e} m_{\rm p} c/\sigma_{\rm T}$ are the Eddington accretion rate and Eddington luminosity.

It is desirable to resolve all these radii in the simulation to determine the structure of the flow self-consistently. This is, however, computationally prohibitive even with a logarithmically spaced grid, because both $R_{\rm tr}$ and $R_{\rm ph}$ are smaller than $R_{\rm B}$ by four-five orders of magnitude (see IHO16). In our simulations, therefore, we focus on the region between $10^{-3}\,R_{\rm B} \lesssim r \lesssim 10\,R_{\rm B}$, and examine whether hyper-Eddington accretion is realized without being impeded by radiation feedback. In this case, our simulation domain does not extend down to $R_{\rm tr}$ and $R_{\rm ph}$. Instead of resolving the small scales, we set the emergent luminosity from the inner region by hand, employing several different models of the radiation efficiency, where super-Eddington luminosity is allowed. Note that in this work, we simply assume that the disk is small enough to be embedded well within the innermost radius of the simulation box, from which radiation with $L > L_{\rm Edd}$ emerges.

4.2.2 Basic equations and numerical schemes

We use the hydrodynamical simulation code ZEUS (Stone & Norman 1992) in order to follow gas dynamics around a BH. For the spherically symmetric case, the continuity equation is

$$\frac{\partial \rho}{\partial t} + \frac{1}{r^2}\frac{\partial}{\partial r}(r^2 \rho v) = 0, \tag{4.3}$$

and the equation of motion is

$$\rho\left(\frac{\partial v}{\partial t} + v\frac{\partial v}{\partial r}\right) = -\frac{\partial p}{\partial r} - \rho\frac{\partial \Phi}{\partial r} + f_{\rm rad}, \tag{4.4}$$

where ρ is gas density, v is velocity of the flow, p is gas pressure, Φ is gravitational potential of the BH and $f_{\rm rad}$ is radiation force per volume. The gas pressure is assumed to be given by the equation of state $p = (\gamma - 1)\rho e$, where $\gamma = 5/3$ and e is specific energy density. We adopt a general relativistic correction for the gravitational potential for completeness, $\Phi = -GM_{\rm BH}/(r - R_{\rm Sch})$, although these corrections are practically negligible in our simulation domain. The energy equation is

$$\rho\left(\frac{\partial e}{\partial t} + v\frac{\partial e}{\partial r}\right) = -p\frac{1}{r^2}\frac{\partial}{\partial r}(r^2 v) - \Lambda + \Gamma, \tag{4.5}$$

where Λ is a cooling rate and Γ is a heating rate. The cooling rate Λ includes effects of collisional excitation of H, He, He^+ atoms and by the H free-free emission (Glover & Jappsen 2007):

$$\Lambda = \Lambda_{\rm H} + \Lambda_{\rm He} + \Lambda_{\rm He^+} + \Lambda_{\rm ff}. \tag{4.6}$$

Equation (4.5) is solved by an implicit method to stabilize the calculation (Anninos et al. 1997).

We treat a chemical reaction network composed of the six primordial species H, H^+, He, He^+, He^{++} and e^-. We set the number abundance of He nuclei relative to H nuclei to 8.33×10^{-2}. We include the chemical reactions of photoionization, collisional ionization and radiative recombination of H, He and He^+. The on-the-spot approximation is adopted, i.e., recombination photons are quickly absorbed as ionizing photons and recombinations to the ground state are ignored. The case B recombination coefficient is used. We solve the chemical reactions for the six species with a semi-implicit formulation (Anninos et al. 1997). The electron fraction is derived according to charge conservation.

The time step in the simulations is set to the minimum value among the Courant time, cooling time, and chemical time, following Whalen & Norman (2006). The Courant number is set to be less than 0.5. We set the cooling time and chemical time to the minimum value of

$$t_{\rm cool} \equiv 0.1\frac{\rho e}{|\Lambda - \Gamma|}, \tag{4.7}$$

$$t_{\rm chem} \equiv 0.01\frac{x_{\rm e} + 0.001 x_{\rm H}}{\dot{x}_{\rm e}}, \tag{4.8}$$

on the simulation grid, where $x_{\rm e}$ and $x_{\rm H}$ are electron and neutral hydrogen number fractions, respectively.

We solve the steady and spherically symmetric radiation transfer equations to compute the radiation force, the heating rates and photoionization rates. The assumption of steady states is valid because the cloud crossing time of photons $\sim \tau r/c$ is much shorter than the time step of the simulations. The transfer equation is

$$\frac{1}{r^2}\frac{\mathrm{d}}{\mathrm{d}r}(r^2 F_\nu) = 4\pi\eta_\nu - \rho\kappa_\nu c E_\nu, \tag{4.9}$$

where F_ν is radiation flux, η_ν is emissivity, κ_ν is opacity and E_ν is radiation energy density. The gas is optically thin against photons within ionized regions and thus in those regions we approximate $F_\nu \approx cE_\nu$.

We calculate the photoionization rates k_i and the heating rates Γ_i ($i =$H, He, He$^+$) in a photon-conserving manner (Whalen & Norman 2006)

$$k_i = \int_{\nu_i} \frac{4\pi\hat{J}_\nu}{h\nu}\sigma_i \mathrm{d}\nu, \tag{4.10}$$

$$\Gamma_i = n_i \int_{\nu_i} \frac{4\pi\hat{J}_\nu}{h\nu}\sigma_i E_{\mathrm{heat,i}} \mathrm{d}\nu, \tag{4.11}$$

where $\hat{J}_\nu$ is average intensity calculated to conserve the number of photons at each simulation grid, σ_i is a cross section for bound-free absorption of ionizing photons, ν_i is ionization energy, and $E_{\mathrm{heat,i}} = h(\nu - \nu_i)$ is excess energy of a photo-electron available for heating. We compute the radiation force due to electron scattering and bound-free transitions by

$$f_{\mathrm{rad,i}} = \frac{n_{\mathrm{e}}}{c}\int \sigma_{\mathrm{T}} F_\nu \mathrm{d}\nu + \frac{\Gamma}{c}. \tag{4.12}$$

We specify the radiation flux entering the simulation domain at its inner boundary by hand as follows. A radiation spectrum is assumed to be a power law of

$$F_{\nu,\mathrm{in}} \propto \left(\frac{\nu}{\nu_{\mathrm{min}}}\right)^{-\alpha} \quad (\nu_{\mathrm{min}} \le \nu \le \nu_{\mathrm{max}}), \tag{4.13}$$

where $h\nu_{\mathrm{min}} = 13.6\,\mathrm{eV}$ is the ionization energy of neutral hydrogen and $h\nu_{\mathrm{max}} \sim 30\,\mathrm{keV}$ is the maximum cut-off energy. We set the power-law index to $\alpha = 1.5$ (see IHO16). The normalization of the radiation flux is calculated by $L = \eta\dot{M}c^2$, where $\dot{M}$ is the mass flux through the innermost grid, η is radiative efficiency, and L is bolometric luminosity. We employ a simple model of the efficiency which mimics the photon trapping effect for a high accretion rate $\dot{m} \equiv \dot{M}/\dot{M}_{\mathrm{Edd}} \gg 1$ as

$$\eta_{f_{\mathrm{Edd}}} \equiv \frac{1}{10 + \dot{m}/f_{\mathrm{Edd}}}, \tag{4.14}$$

where $f_{\mathrm{Edd}} \equiv L_{\mathrm{max}}/L_{\mathrm{Edd}}$ with L_{max} being the maximum luminosity for $\dot{m} \to \infty$. As an illustration, in Figure 4.2 we represent the model luminosity as a function of $\dot{m}$ using equation (4.14). In this model, the efficiency becomes a constant at $\eta \simeq 0.1$ for low $\dot{m}$, while $\eta \to f_{\mathrm{Edd}}/\dot{m}$ for high $\dot{m}$. Since the accretion rates in our simulations do not decrease below $\dot{m} \approx 10^{-3}$, the critical value at which a transition to an advection-dominated accretion flow (ADAF) would be expected (Ichimaru 1977, Narayan & Yi 1994), we do not consider an ADAF. Note that IHO16 considered only the case of $f_{\mathrm{Edd}} = 1$, where the luminosity never exceeds the Eddington luminosity. We here relax their assumption and allow super-Eddington luminosities.

In addition to the models of the radiative efficiency in equation (4.14), we also consider a more realistic model of the efficiency which asymptotically approaches a logarithmic form for high $\dot{m}$ and

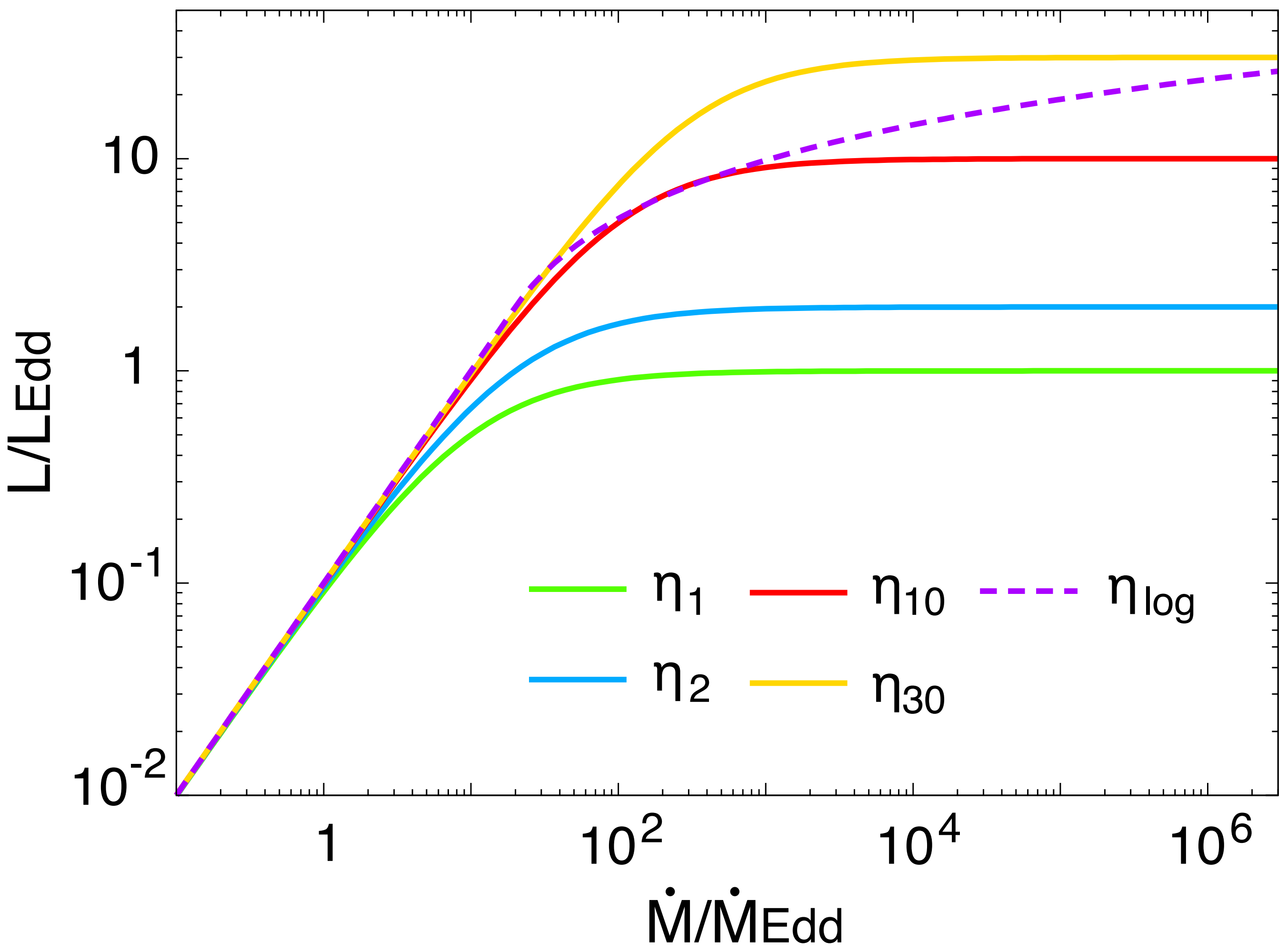

Fig. 4.2 Models of bolometric luminosity at the innermost grid $r_{\rm min}$, as a function of the accretion rate $\dot{M}/\dot{M}_{\rm Edd}$. The different lines correspond to the different models of the radiative efficiency, $\eta_{f_{\rm Edd}}$ with $1 \leq f_{\rm Edd} \leq 30$ (solid lines) and $\eta_{\log}$ (dashed line). This figure is reproduced from Sakurai, Inayoshi & Haiman (2016).

better describes the well-known behavior of the slim disk (Watarai et al. 2000),

$$\eta_{\log} = \begin{cases} 0.1 & (\dot{m} < 20) \\ \dfrac{2}{\dot{m}}\left[1 + \ln\left(\dfrac{\dot{m}}{20}\right)\right] & (\dot{m} > 20). \end{cases} \tag{4.15}$$

The prescription is motivated by simulations with $\dot{m} \gg 1$, which show that photon trapping do not totally suppress the luminosity emerging from the central region (Jiang, Stone & Davis 2014, Sądowski et al. 2014).

Spherical coordinates are set with a logarithmically spaced grid in the radial direction. We set the positions of the inner and outer boundary to $r_{\rm min}$ and $r_{\rm max}$. The i-th grid is written as $r_i = r_{\rm min} + \Delta r_0(\epsilon^{i-1} - 1)/(\epsilon - 1)$, where Δr_0 is a size of the inner-most grid and $\epsilon = \Delta r_{i+1}/\Delta r_i$ is a ratio between consecutive grids. With the given number of the grid cells N, $\Delta r_0 = (r_{\rm max} - r_{\rm min})(\epsilon - 1)/(\epsilon^N - 1)$. In this work, we set $N = 700$, $\epsilon 1.01$, $r_{\rm min} \sim 10^{-3}\, R_{\rm B}$ and $r_{\rm max} = 5000\, r_{\rm min}$ in order to calculate dynamics of gas accretion from outside the Bondi radius with sufficient resolution.

The 'outflow' boundary condition (BC) is adopted at the innermost grid (Stone & Norman 1992). In this BC, the innermost velocity $v(r_{\rm min})$ is normally set to $v(r_{\rm min} + \Delta r_0)$ to circumvent spurious reflection of wave energy at the boundary. However, when $L > L_{\rm Edd}$, using this BC artificially underestimates effect of radiation force on the innermost shell. This is because the velocity at $r_{\rm min}$, wherein the infalling gas would be significantly decelerated by radiation, is replaced by the velocity at $r_{\rm min} + \Delta r_0$, wherein deceleration is inefficient since radiation is partially absorbed by gas at $r_{\rm min}$ before reaching $r_{\rm min} + \Delta r_0$. To avoid this underestimate, we adopt an alternative inner BC: $v(r_{\rm min} + \Delta r_0)$ is set to $v(r_{\rm min})$ for $L > L_{\rm Edd}$.

4.3 Results of the simulations

Figure 4.3 shows time evolution of accretion rates for several models with the radiative efficiency $\eta_{f_{\rm Edd}}$ ($f_{\rm Edd} = 1, 2, 10$ and 30, solid lines) and $\eta_{\rm log}$ (dashed lines). The BH mass is set to $M_{\rm BH} = 2\times 10^4\,{\rm M}_\odot$, and an initially static neutral uniform gas is adopted with $n_\infty = 10^5\,{\rm cm}^{-3}$ and $T_\infty = 10^4\,{\rm K}$. The dotted line represents the evolution with no radiation, the accretion rate approaching the Bondi rate,

$$\frac{\dot{M}_{\rm B}}{\dot{M}_{\rm Edd}} = 7.3 \times 10^3\, M_{\rm BH,4} n_{\infty,5} T_{\infty,4}^{-3/2}, \tag{4.16}$$

where the Bondi rate is estimated for the isothermal case,

$$\dot{M}_{\rm B} = e^{3/2} \pi \rho_\infty R_{\rm B}^2 c_\infty, \tag{4.17}$$

and $n_{\infty,5} \equiv n_\infty/10^5\,{\rm cm}^{-3}$. With radiation on for the case $f_{\rm Edd} = 1$, the accretion rate is much lower than that in the case without radiation. The average rate is limited to $\sim 20\dot{M}_{\rm Edd}$ for $t < 10^5\,{\rm yr}$, where the luminosity from the central region is $\sim 0.7\,L_{\rm Edd}$. For $t \gtrsim 1.3 \times 10^5\,{\rm yr}$, the accretion rate becomes episodic and rises promptly to a higher value. This result is consistent with that shown in IHO16 (their figure 5). After the transition, the accretion rate gradually approaches the Bondi rate. The hyper-Eddington accretion is realized since the H II region is always confined inside the Bondi radius, i.e., $R_{\rm H\,II} \lesssim R_{\rm B}$ (see equation 1.7).

For moderately higher values of $1 < f_{\rm Edd} \leq 10$, the same transition to steady hyper-Eddington accretion is found as in $f_{\rm Edd} = 1$. Even in these cases, luminosity before the transition is confined to $\sim L_{\rm Edd}$. The transition time is delayed for higher $f_{\rm Edd}$ since radiation force is non-negligible, and contributes an outward-directed force on the infalling gas. After the transition, the luminosity exceeds $L_{\rm Edd}$. The hyper-Eddington accretion is yet maintained because ram pressure overcomes radiation force at the innermost region.

In the model with $\eta_{\rm log}$, the result is qualitatively the same since luminosity after the transition is $L \lesssim 20\,L_{\rm Edd}$ which is as small as in the case with $1 < f_{\rm Edd} \leq 10$.

For the highest value with $f_{\rm Edd} = 30$, the transition to the hyper-Eddington phase occurs, but behavior of the accretion rate differes f from the other cases after the transition. Namely, the accretion rate becomes unstable and begins to oscillate. In this case, radiation force with $L \simeq 30L_{\rm Edd}$ prevents a steady accretion flow. However, the radiation force does not suppress the net mass accretion and the time-averaged accretion rate still matches the Bondi rate. This result implies that the central BH grows rapidly even for $f_{\rm Edd} \gtrsim 30$. The critical luminosity to keep steady hyper-Eddington accretion is determined by comparing radiation force with ram pressure and gravity of the infalling gas (see Section 4.4).

In Figure 4.4, we show radial profiles of gas density, temperature, and a local mass inflow rate $\dot{M} = 4\pi r^2 \rho |v|$ for the model of $f_{\rm Edd} = 10$ at the five different times corresponding to the open circles in Figure 4.3. As IHO16 argued, the condition required for hyper-Eddington accretion is given by equation (1.7), which is derived from the condition that the size of the H II region $R_{\rm H\,II}$ is smaller than the initial Bondi radius $R_{\rm B,0}$. Figure 4.4(b) shows that the condition of $R_{\rm H\,II} < R_{\rm B,0}$ is satisfied for

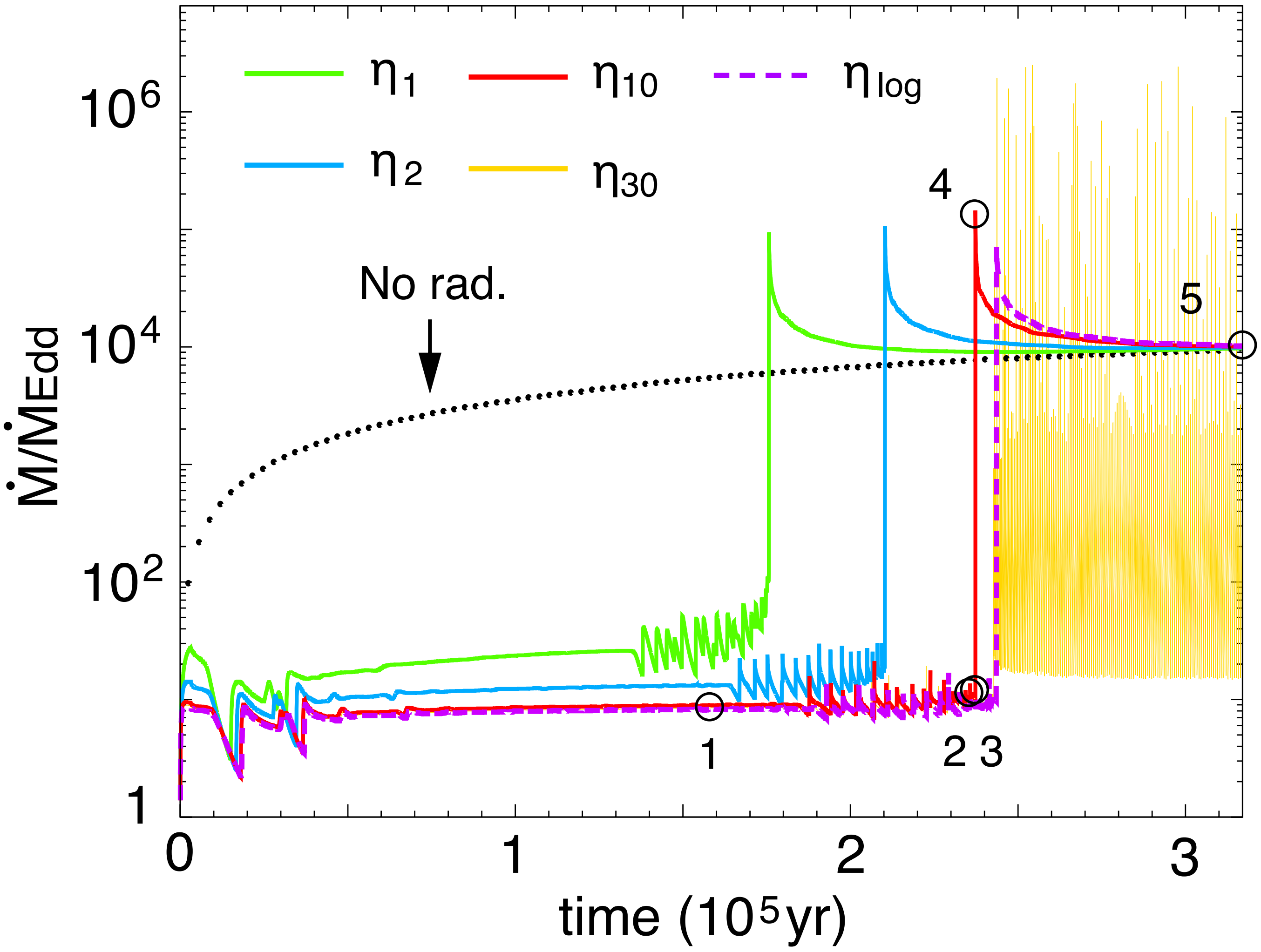

Fig. 4.3 Time evolution of accretion rates for the five different models with radiative efficiency represented in Figure 4.2. We adopt $M_{\rm BH} = 2 \times 10^4\,{\rm M}_\odot$,$n_\infty = 10^5\,{\rm cm}^{-3}$ and $T_\infty = 10^4\,{\rm K}$. The dotted line depicts the time evolution of the accretion rate in the absence of any radiation, which settles to the Bondi rate. Open circles mark five different times, at which radial profiles for the model of η_{10} are shown in Figure 4.4. This figure is reproduced from Sakurai, Inayoshi & Haiman (2016).

this case. We can explain the physical reason for the occurrence of the transition as follows. While gas accretion proceeds before the transition, the H II region expands to the radius of $R_{\rm H\,II}$ inside which radiation force and gas pressure suppress the accretion. Since $R_{\rm H\,II} < R_{\rm B,0}$, the accreting gas accumulates in the region $R_{\rm H\,II} \lesssim r \lesssim R_{\rm B}$ (line 1 in Figure 4.4a). Once the accumulating gas shell becomes sufficiently dense and massive, it begins to move inward due to the gravitational force of the central BH (line 2 and 3 in Figure 4.4a). At the same time, the H II region contracts and the accretion rate increases (line 4 in Figures 4.4 b and c). After the transition, the gas profile reaches a steady and isothermal Bondi profile with $\rho \propto r^{-3/2}$ and $T \simeq 8000\,{\rm K}$ (line 5 in Figure 4.4).

For the case of $f_{\rm Edd} = 30$, radial profiles of the gas properties are almost identical to those of $f_{\rm Edd} = 10$, except inside a narrow central H II region, where strong radiation force eventually blows the ionized gas outward. With the resulting decrease of the accretion rate and luminosity, ram pressure caused by rapid accretion from outside the H II region pushes the blown gas inward again, leading to episodic accretion. The result also shows that as long as $R_{\rm H\,II} < R_{\rm B,0}$, the time-averaged accretion rate will match the steady hyper-Eddington Bondi rate, even for $f_{\rm Edd} = 30$.

We further elucidate the effect of radiation force on the accretion flow with a super-Eddington luminosity. To this end, we perform a separate suite of simulations as an academic exercise, where we assume a steady and isothermal Bondi accretion flow as the initial condition and then turn on

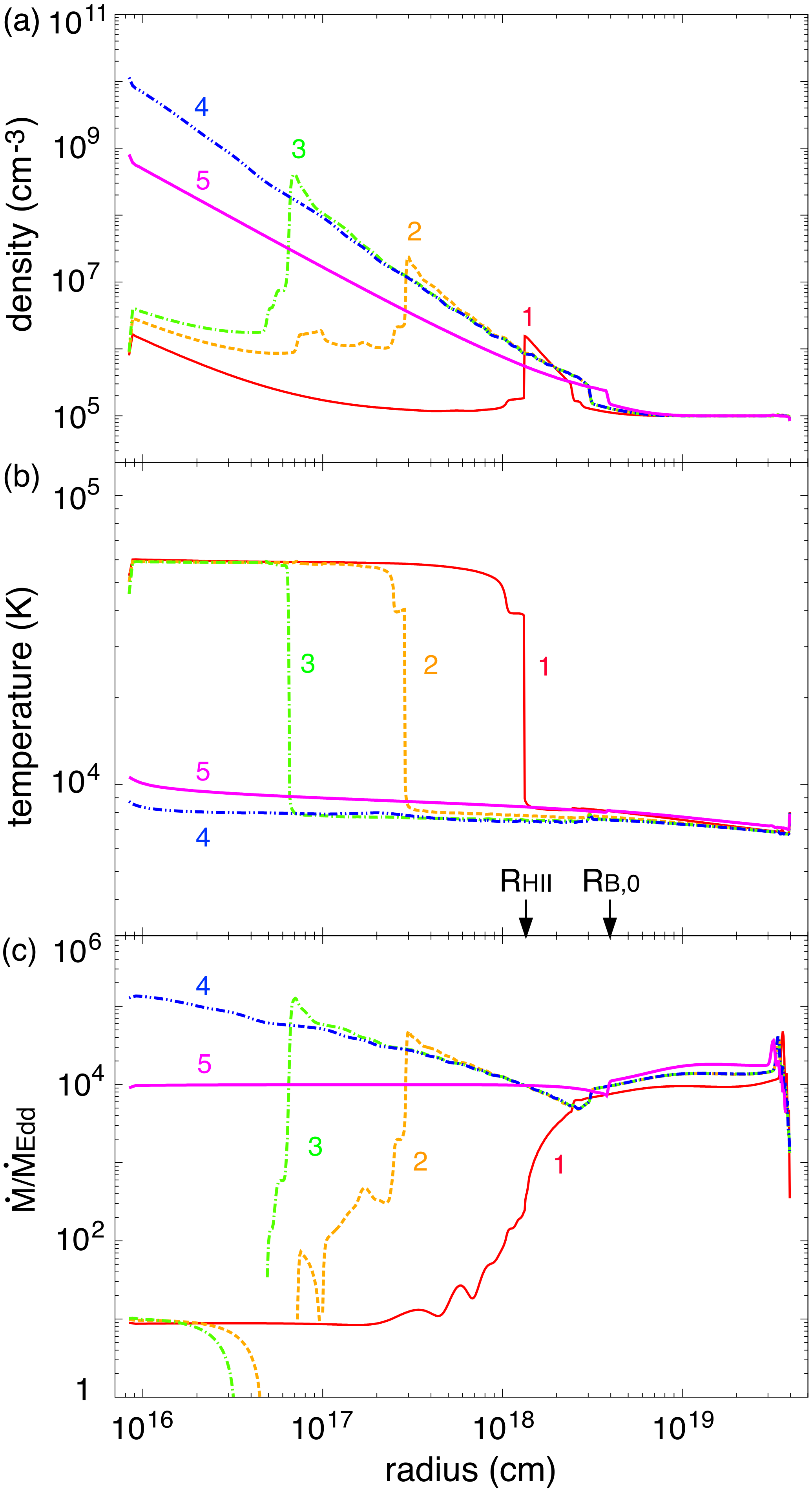

Fig. 4.4 Radial profiles of density, temperature and a local accretion rate for the model of η_{10} at the five different times shown by open circles in Figure 4.3. The five lines correspond to (1) $t = 1.58 \times 10^5$ yr (red), (2) 2.35×10^5 yr (orange), (3) 2.371×10^5 yr (green), (4) 2.373×10^5 yr (blue) and (5) 3.17×10^5 yr (magenta). In panel (b), we denote the initial Bondi radius $R_{\rm B,0}$ and the (initial) size of the H II region $R_{\rm H\,II}$. In this case, the condition which is required for steady hyper-Eddington accretion, $R_{\rm H\,II} \lesssim R_{\rm B,0}$, is satisfied (equation 1.7). Note that the size of the H II region in any epoch is estimated as the radius where gas temperature steeply rises with decreasing the radius from the center, namely, (1) $R_{\rm H\,II,1} = R_{\rm H\,II} \sim 1.4 \times 10^{18}$ cm, (2) $R_{\rm H\,II,2} \sim 3 \times 10^{13}$ cm, (3) $R_{\rm H\,II,3} \sim 6.5 \times 10^{16}$ cm, (4) $R_{\rm H\,II,4} < r_{\rm min} = 8 \times 10^{15}$ cm and (5) $R_{\rm H\,II,5} < r_{\rm min}$. This figure is reproduced from Sakurai, Inayoshi & Haiman (2016).

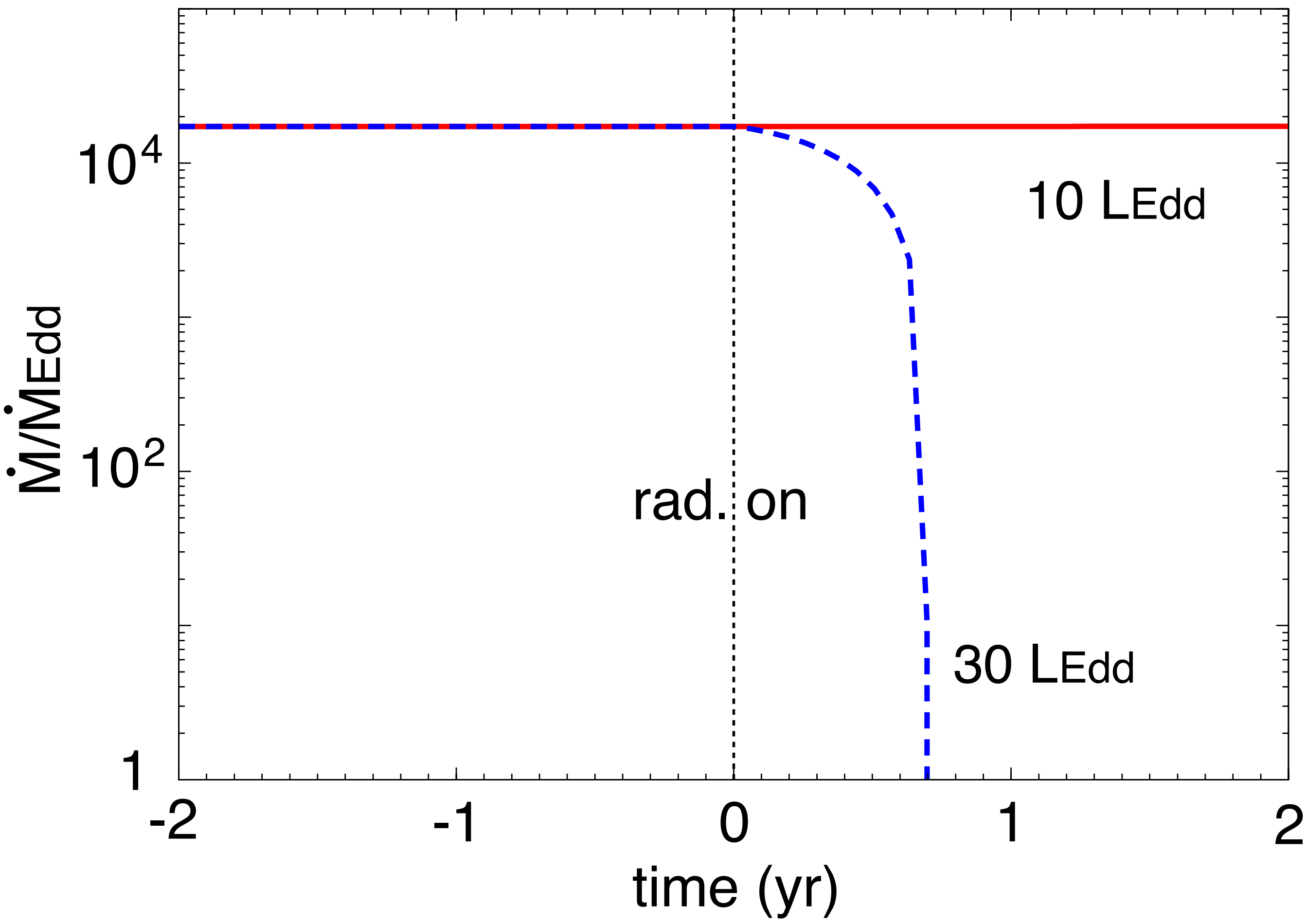

Fig. 4.5 Effect of radiation force on an initially steady and isothermal Bondi accretion flow with a constant luminosity source. At $t = 0$, the radiation is turned on with $L = 10\,L_{\rm Edd}$ (red solid) or $30\,L_{\rm Edd}$ (blue dashed). In the former case, the Bondi accretion rate is maintained, while in the latter cace, the accretion is blocked by radiation force. This figure is reproduced from Sakurai, Inayoshi & Haiman (2016).

the central source with constant luminosity which is independent of the accretion rate. Figure 4.5 shows two cases of $L = 10\,L_{\rm Edd}$ (red solid) and $30\,L_{\rm Edd}$ (blue dashed). For $L = 10\,L_{\rm Edd}$, the gas accretion does not change at all after the radiation is turned on at $t = 0$. By contrast, for $L = 30\,L_{\rm Edd}$, radiation force is strong enough to shut off the gas inflow. This behavior is different from the previous case of $f_{\rm Edd} = 30$ (see Figure 4.3), where accretion is episodic, rather than being shut off.

4.4 Analytical arguments

We have shown in Section 4.3 that a transition to a steady hyper-Eddington accretion occurs with $M_{\rm BH} = 2\times10^4\,{\rm M}_\odot$ and $n_\infty = 10^5\,{\rm cm}^{-3}$, as long as the maximum luminosity is $L/L_{\rm Edd} \equiv f_{\rm Edd} \lesssim 20$. For $f_{\rm Edd} \geq 30$, the steady accretion is replaced by highly variable episodic accretion, but the time-averaged rate remains close to the Bondi rate. In this section, we discuss the physical interpretation of these results. First, we consider conditions for the transition to occur with analytical arguments. Then, we consider a toy model of an optically thick spherical shell, driven by radiation force from a central source, to further justify the results of our simulations.

4.4.1 Conditions for hyper-Eddington accretion

As explained in Section 4.3, the transition to hyper-Eddington accretion occurs if the Bondi radius $R_\mathrm{B} \propto M_\mathrm{BH} T_\infty^{-1}$ is larger than the size of the H II region $R_\mathrm{H\,II}$. The latter quantity is estimated by a balance between photoionization and radiative recombination,

$$R_\mathrm{H\,II} = \left(\frac{3Q_\mathrm{ion}}{4\pi n_\infty^2 \alpha_\mathrm{B}} \right)^{1/3}, \tag{4.18}$$

where Q_ion is the average number of ionizing photons released per unit time and α_B is the case B recombination rate. Since we adopt the power-law spectrum with the index of -1.5, we get $Q_\mathrm{ion} = L/3h\nu_\mathrm{min}$. Using the fact that the luminosity L is restricted to $\sim L_\mathrm{Edd}$ before the transition, $R_\mathrm{H\,II} \propto L_\mathrm{Edd}^{1/3} n_\infty^{-2/3} \propto M_\mathrm{BH}^{1/3} n_\infty^{-2/3}$ and the transition condition of $R_\mathrm{B} > R_\mathrm{H\,II}$ is rewritten as equation (1.7), where the temperature inside the H II region is set to $6 \times 10^4\,\mathrm{K}$. For the evaluation of $R_\mathrm{H\,II}$, we here assume a constant density profile with n_∞ instead of the Bondi density profile, the latter of which is actually realized just before the transition. With the constant density profile, the resulting value of $R_\mathrm{H\,II}$ is larger by a factor of a few than the actual value. Thus, our assumption of a constant density profile is conservative with regard to the condition for the hyper-Eddington accretion.

After the transition, radiation luminosity emitted from the central source would be brighter than $\sim L_\mathrm{Edd}$ in certain directions (Ohsuga et al. 2005, Jiang, Stone & Davis 2014, Sądowski et al. 2014: e.g.,). In a standard picture of outflows driven by radiation force of $L > L_\mathrm{Edd}$, hyper-Eddington accretion seems unlikely to occur since radiation force due to electron scattering dominates the BH gravity. However, steady hyper-Eddington accretion can actually occur in our case, where all momentum of the radiation is essentially absorbed by neutral hydrogen at the boundary of the H II region within a short mean-free path. Although the radiation force exerted on the recombination shell near $R_\mathrm{H\,II}$ is actually larger than that on to ionized gas, the excess is only by a factor of $1/\tau_\mathrm{e}$, where $\tau_\mathrm{e} \sim n\sigma_\mathrm{T} R_\mathrm{H\,II} (\lesssim 1)$. Outside the H II region where rapid hyper-Eddington inflow can develop, the radiation has no effect. The inflow gas exerts strong inward ram pressure at the edge of the H II region, which can significantly exceed the BH gravity. In addition, the infalling gas can accumulate near $R_\mathrm{H\,II}$ and increase inward gravitational force. Thus, if the inward ram pressure plus the gravity exceeds the outward radiation force, the steady hyper-Eddington accretion can occur.

The stability condition after the transition is written as $\dot{M}_\mathrm{B}|v| > L/c$ at $r = r_\star$ where all radiation is absorbed. We here omit the contribution of gravity to simplify the argument. Since the inflow velocity is $|v| = (2GM_\mathrm{BH}/r)^{1/2}$ at $r \geq r_\star$, we get

$$f_\mathrm{Edd} = \frac{L}{L_\mathrm{Edd}} \lesssim 11\, M_\mathrm{BH,4}^{3/2} n_{\infty,5} T_{\infty,4}^{-3/2} r_{\star,15}^{-1/2}, \tag{4.19}$$

with $r_{\star,15} = r_\star/10^{15}\,\mathrm{cm}$. As a conservative estimate, we set $r_\star = r_\mathrm{min} (= 8 \times 10^{15}\,\mathrm{cm})$. With $M_\mathrm{BH,4} = 2$, $n_{\infty,5} = 1$ and $T_{\infty,4} = 1$, hyper-Eddington accretion remains to be stable as long as $f_\mathrm{Edd} \lesssim 10$. The estimate agrees with our simulation results represented in Section 4.3. In practice, radiation would emerge from a photosphere located at a smaller radius, $R_\mathrm{ph} (< r_\mathrm{min})$. Although the photosphere is not resolved in our simulations, if we use $r_\star = R_\mathrm{ph} \simeq 10^{14}\,\mathrm{cm}$ which is shown in figure 11 of IHO16, we find the critical luminosity of $f_\mathrm{Edd} \lesssim 100$. This critical luminosity is discussed further in Section 4.4.2 using a simple toy model.

We summarize the necessary conditions for the hyper-Eddington accretion in Figures 4.6 and 4.7. The conditions of equations (4.19) (solid line) and (1.7) (dashed line) are shown in the $f_\mathrm{Edd} - M_\mathrm{BH}$

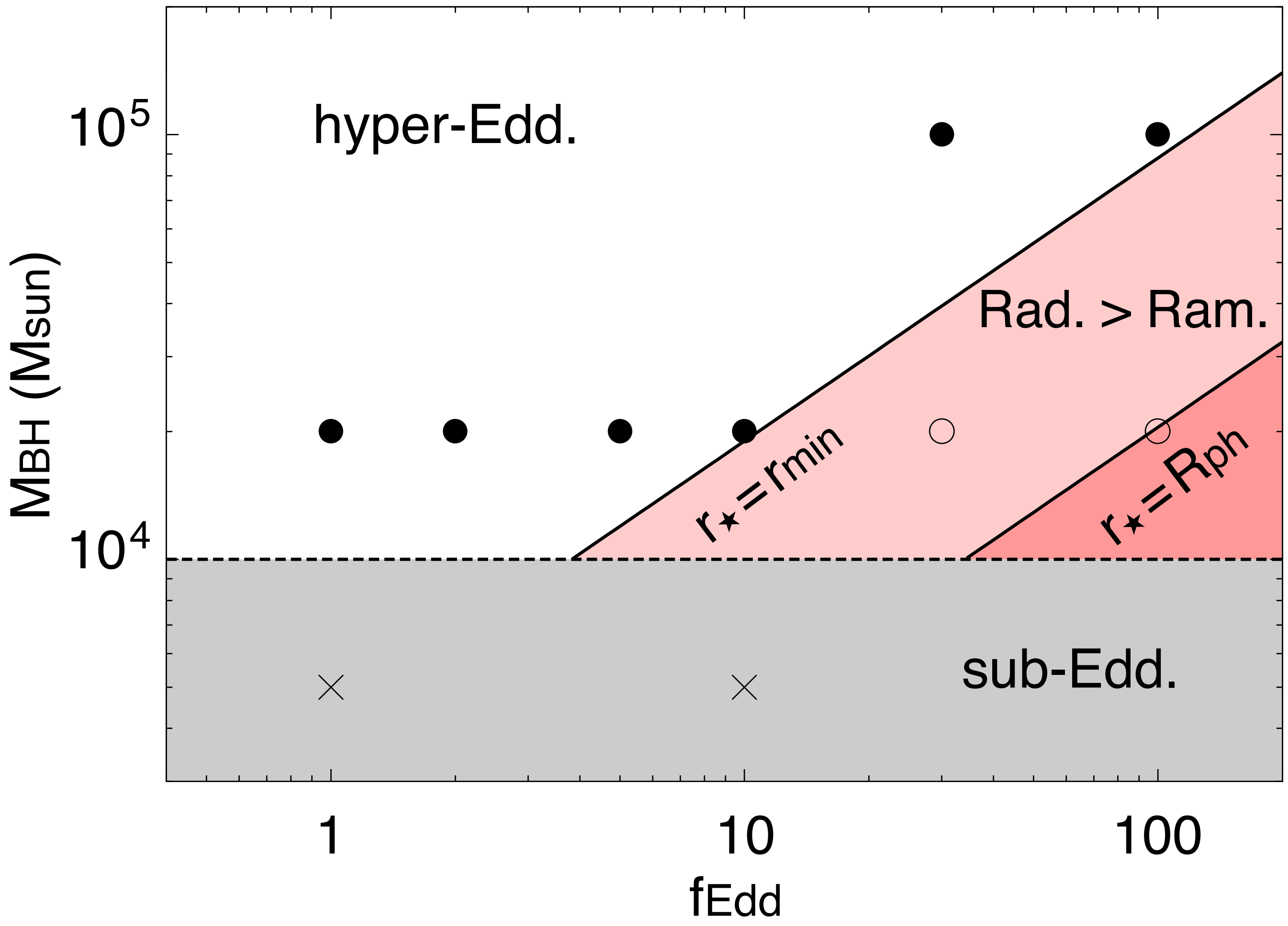

Fig. 4.6 Summary of three different accretion regimes for different values of $f_{\rm Edd}$ and $M_{\rm BH}$. Dashed and solid lines represent the conditions given by equation (1.7) and (4.19) with $n_\infty = 10^5\,{\rm cm}^{-3}$ and $T_\infty = 10^4\,{\rm K}$, respectively. For the solid lines, we denote two cases with the central radiation emerging from $r_\star = r_{\rm min}$, the inner boundary of our simulations, or from $r_\star = R_{\rm ph}$, the expected location of the photosphere. The different symbols denote simulation runs in which steady hyper-Eddington accretion is realized (filled circles), gas accretion becomes strongly episodic by radiation force (open circles), and no transition to hyper-Eddington accretion is realized due to radiation heating and ionization (crosses). This figure is reproduced from Sakurai, Inayoshi & Haiman (2016).

and $f_{\rm Edd} - n_\infty$ planes, respectively. For the solid lines, either $r_\star = r_{\rm min}$ or $r_\star = R_{\rm ph}$ are adopted. In the parameter regions below the dashed lines, hyper-Eddington accretion is not realized due to radiation heating and ionization (cross; sub-Edd.). For the region between the solid and dashed lines, hyper-Eddington accretion could occur but a steady state is not realized because radiation force dominates ram pressure (open circle; Rad. ¿ Ram.). Only in the region above those lines, steady hyper-Eddington accretion is achieved (filled circle; hyper-Edd.).

4.4.2 1D momentum-driven shell model

To understand the physics which allows hyper-Eddington accretion, we consider a model of a geometrically thin, but optically thick spherical shell around a point source, which is driven by radiation force into a rapidly collapsing medium (King 2003, Kasliwal, Lovelace & Houck 2005). The luminosity L from the central source is assumed constant, and the equation of motion for the shell is

$$\frac{\mathrm{d}}{\mathrm{d}t}(M_{\rm sh}\dot{R}_{\rm sh}) = \frac{L}{c} - \dot{M}(|v| + \dot{R}_{\rm sh}) - \frac{GM_{\rm BH}M_{\rm sh}}{R_{\rm sh}^2}, \tag{4.20}$$

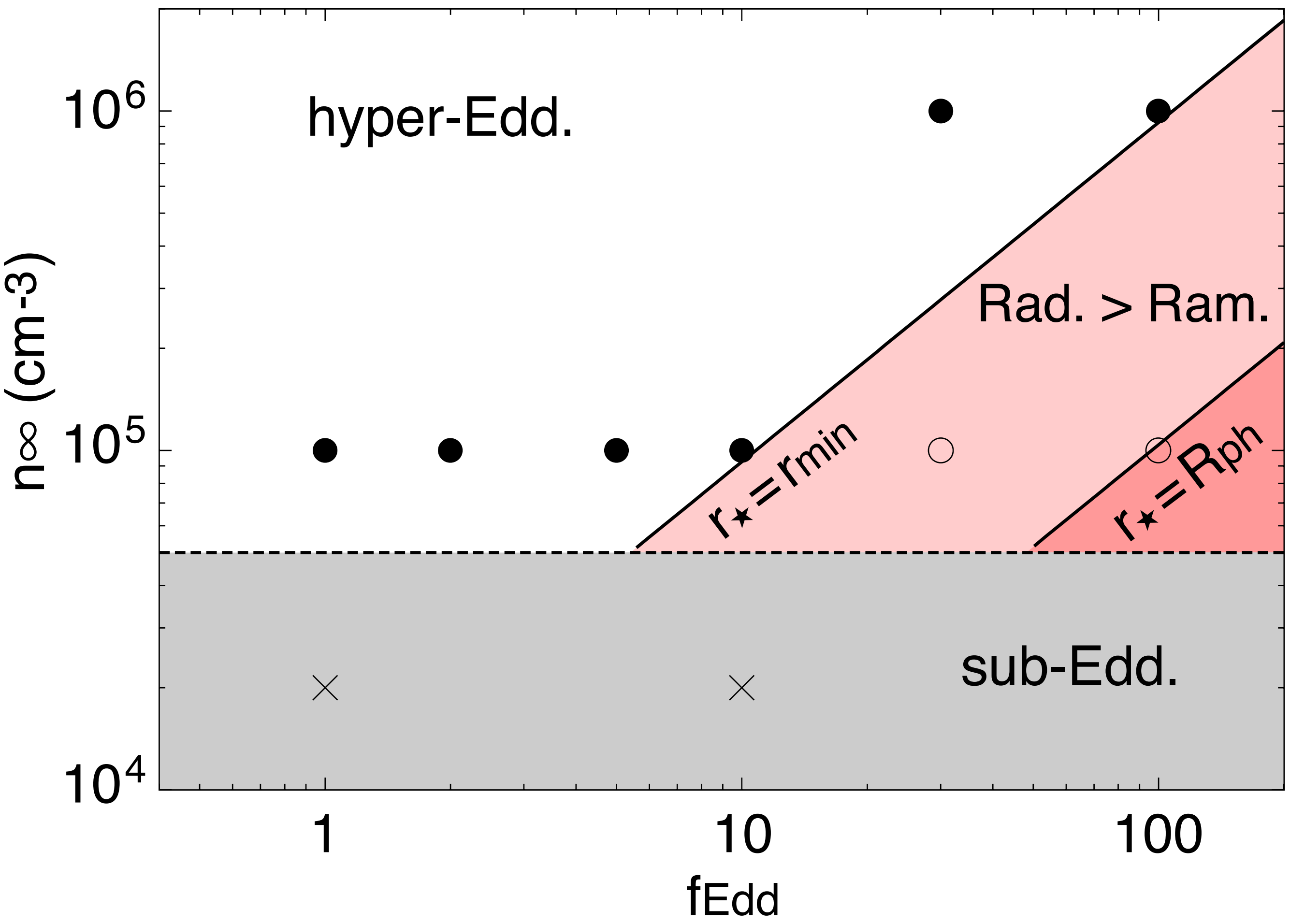

Fig. 4.7 Three different accretion regimes are shown for different values of $f_{\rm Edd}$ and n_∞, where we use $M_{\rm BH} = 2 \times 10^4\,{\rm M}_\odot$ and $T_\infty = 10^4\,{\rm K}$. See Figure 4.6 for the explanation of the lines and symbols. This figure is reproduced from Sakurai, Inayoshi & Haiman (2016).

where $M_{\rm sh}$ is mass of the shell, $R_{\rm sh}$ is distance of the shell from the central point, and $\dot{M}$ and v are an accretion rate and velocity of the gas inflow just outside the shell. The terms on the right-hand side (RHS) correspond to the outward radiation force exerted on the shell, and the inward forces by ram pressure of the rapid inflow and the BH gravity. We assume that (i) the shell is optically thick to ionizing radiation and absorbs all incident radiation with momentum L/c, and that (ii) the whole cloud is effectively optically thin to recombination radiation.

In this model, we omit the contribution of photon scattering which would actually contribute to radiation pressure force. If the recombination radiation is efficiently scattered by the neutral shell, i.e., if condition (ii) is invalid, then the radiation is trapped inside the neutral shell just outside the H II region. Multiple scattering events inside the shell would increase the total radiation pressure force to $\simeq \tau_{\rm scat} L/c$, wherein $\tau_{\rm scat}$ is an effective optical depth to scattering. In our case, H I Rayleigh scattering is negligible, but Ly α scattering can be important owing to the high optical depth at the line center, $\tau_{{\rm Ly}\alpha} \sim 10^{10} - 10^{12}$. However, before Ly α radiation pressure affects a motion of the shell, the Ly α photons will be converted to $2S \rightarrow 1S$ continuum photons and $\sim 1\,{\rm eV}$ photons ($\rm H^-$ free-bound transition), to which the neutral shell is optically thin. We therefore expect that the scattering is not significant and our condition (ii) holds, with an effective scattering opacity $\tau_{\rm scat}$ a factor of a few. Nevertheless, future works are needed to examine the effect of the trapping of Ly α radiation, the conversion to lower energy continuum photons and the escape of these photons from the cloud.

The mass growth rate of the shell is

$$\frac{\mathrm{d}M_{\mathrm{sh}}}{\mathrm{d}t} = \dot{M}\left(1 + \frac{\dot{R}_{\mathrm{sh}}}{|v|}\right), \tag{4.21}$$

and the initial shell mass is

$$M_{\mathrm{sh},0} = \int_0^{R_{\mathrm{sh},0}} 4\pi r^2 \rho(r)\mathrm{d}r, \tag{4.22}$$

where the subscript 0 indicates the initial value. For simplicity, we consider two extreme cases of the density profile, namely, a constant density profile $\rho(r) = \mathrm{const.}$ and the Bondi profile $\rho(r) \propto r^{-3/2}$. The corresponding initial masses are

$$M_{\mathrm{sh},0} = \begin{cases} \dfrac{4}{3}\pi R_{\mathrm{sh},0}^3 \rho_\infty & \text{for } \rho(r) = \rho_\infty \\ \dfrac{8}{3}\pi R_{\mathrm{B}}^{3/2} R_{\mathrm{sh},0}^{3/2} \rho_\infty & \text{for } \rho(r) = \rho_\infty \left(\dfrac{r}{R_{\mathrm{B}}}\right)^{-3/2} \end{cases}. \tag{4.23}$$

We here adopt $\dot{M} = \dot{M}_{\mathrm{B}}$, $|v| = (2GM_{\mathrm{BH}}/r)^{1/2}$ (free-fall velocity), $\dot{R}_{\mathrm{sh},0} = 0$, $M_{\mathrm{BH}} = 2 \times 10^4\,\mathrm{M}_\odot$, $n_\infty = 10^5\,\mathrm{cm}^{-3}$ and $T_\infty = 10^4\,\mathrm{K}$.

First of all, we consider time evolution of a dense shell which initially locates at $R_{\mathrm{sh},0} = R_{\mathrm{H\,II}} (\simeq 1.4 \times 10^{18}\,\mathrm{cm})$ before the transition to hyper-Eddington accretion, with luminosity from the source $L \simeq L_{\mathrm{Edd}} (f_{\mathrm{Edd}} \simeq 1)$. The shell corresponds to that represented in Figure 4.4(a) (phase 1). Figure 4.8 shows three cases, wherein ram pressure of the inflowing gas and BH gravity on the accumulated mass are both included (red), and wherein either the gravity (blue) or the ram pressure (green) are artificially excluded. Solid (dashed) lines correspond to the case of constant (Bondi) initial density profiles. As this figure shows, the shell radius contracts when both ram pressure and gravity are incorporated. By contrast, when either of the inward forces are turned off, the shell continues to expand and never falls on to the center. Although the expansion velocity of the shell is slower for the cases with heavier masses (dashed), the choice of the initial shell mass does not change the qualitative behavior of the shell. Overall, it is the combination of the ram pressure and gravity that overcomes the radiation force and yields hyper-Eddington accretion. The role of the ram pressure is somewhat more important for triggering the hyper-Eddington accretion, which can be seen from the fact that the shell expands more rapid without ram pressure (green) than without gravity (blue).

Next, in Figure 4.9 we show time evolution of a shell initially located at $R_{\mathrm{sh},0} = r_{\mathrm{min}} (= 8 \times 10^{15}\,\mathrm{cm})$, for the cases $f_{\mathrm{Edd}} = 1$ (red), 10 (green) and 30 (blue). These correspond to the cases after the hyper-Eddington accretion is achieved in our simulations. The initial shell mass is estimated assuming a constant density profile, and the effects of both ram pressure and gravity are included. Figure 4.9(a) clearly shows that for $f_{\mathrm{Edd}} \lesssim 10$ the shell shrinks within 20 yr, corresponding to the case that the hyper-Eddington accretion continues after the transition. The result of this shell evolution is in excellent agreement with our simulations and analytical arguments in Section 4.4.1. In Figure 4.9(b), we also show the case for the initial shell radius $R_{\mathrm{sh},0} = R_{\mathrm{ph}} (\simeq 10^{14}\,\mathrm{cm})$, with $f_{\mathrm{Edd}} = 100$ (red), 200 (green), and 300 (blue). For $f_{\mathrm{Edd}} \lesssim 100$, the shell contracts, which is again in agreement with the results of the analytical arguments shown in Figure 4.6 and Figure 4.7.

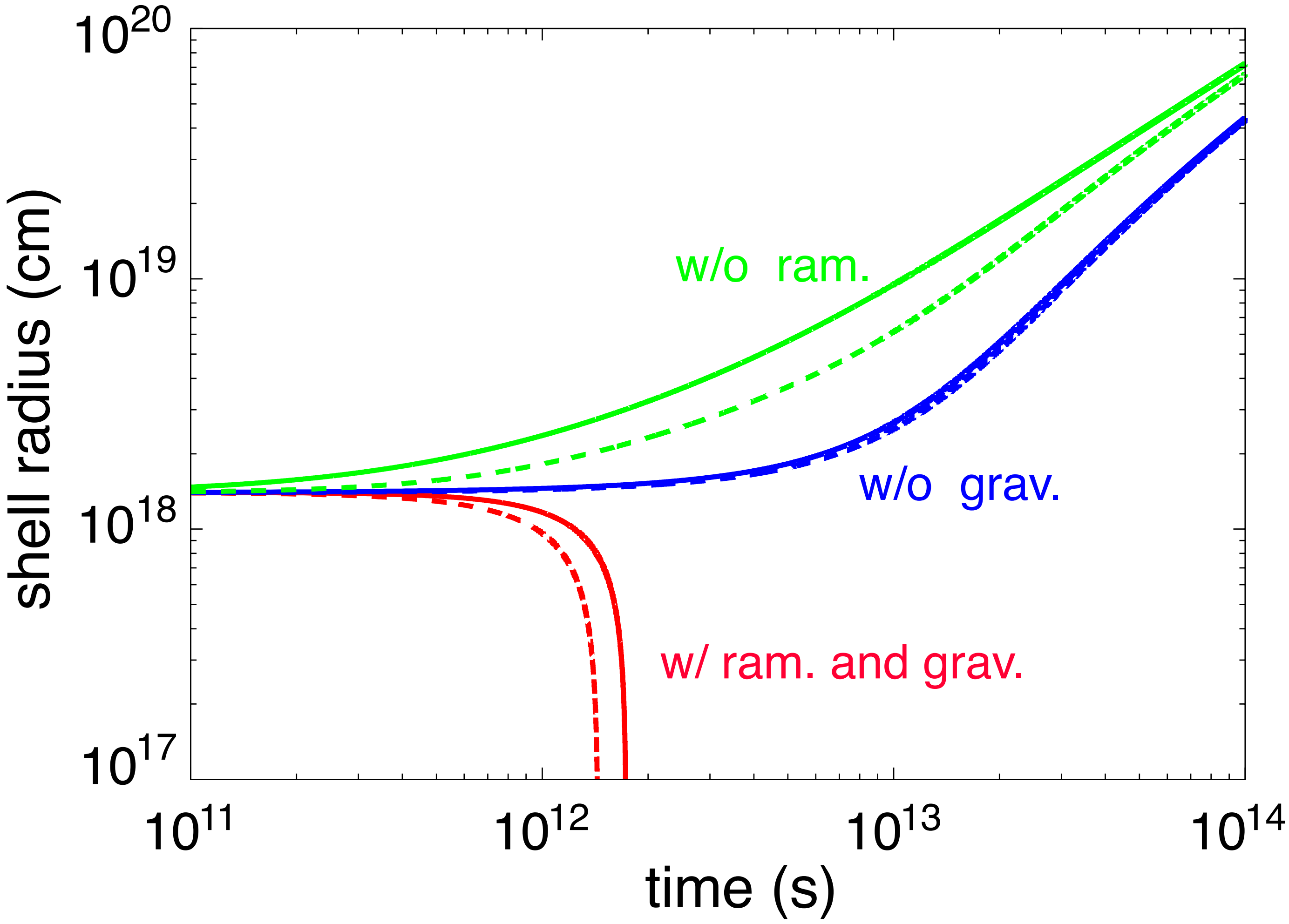

Fig. 4.8 Time evolution of a geometrically thin, optically thick shell, which is driven by radiation force of a central source into a rapidly collapsing cloud. The evolution is computed from a toy model described as equation (4.20) which incorporates the outward radiation force (first term of RHS of equation 4.20) as well as the inward forces of ram pressure and gravity on the shell (second and third terms of RHS of equation 4.20), initially located at $R_{\mathrm{sh},0} = R_{\mathrm{H\,II}}(\simeq 1.4 \times 10^{18}\,\mathrm{cm})$. Each line corresponds to the case with both ram pressure and gravity (red), and with either ram pressure (green) or gravity (blue) artificially turned off. For each case, the initial density profile is assumed to be either constant (solid) or to follow the Bondi profile (dashed) (see equation 4.23). We adopt $f_{\mathrm{Edd}} = 1$, $\dot{M} = \dot{M}_{\mathrm{B}}$, $M_{\mathrm{BH}} = 2 \times 10^4\,\mathrm{M}_\odot$, $n_\infty = 10^5\,\mathrm{cm}^{-3}$ and $T_\infty = 10^4\,\mathrm{K}$. The shell corresponds to that shown in phase 1 in Figure 4.4(a). This figure is reproduced from Sakurai, Inayoshi & Haiman (2016).

4.5 Summary and discussions

We have performed 1D radiation hydrodynamical simulations in order to solve spherically symmetric accretion flows on to massive BHs with a high rate. Our setup extends simulations in the earlier work (IHO16), by allowing the central luminosity to exceed the Eddington luminosity ($1 \lesssim L/L_{\mathrm{Edd}} \lesssim 100$). The setup of the super-Eddington luminosity is motivated by the possibility of gas accreting with finite angular momentum through a bright nuclear disk which is fed at rates well in excess of the Eddington accretion rate (e.g., Ohsuga et al. 2005, Jiang, Stone & Davis 2014, McKinney et al. 2014, Sądowski et al. 2014).

It is found that a transition to a stable hyper-Eddington accretion phase occurs when the two

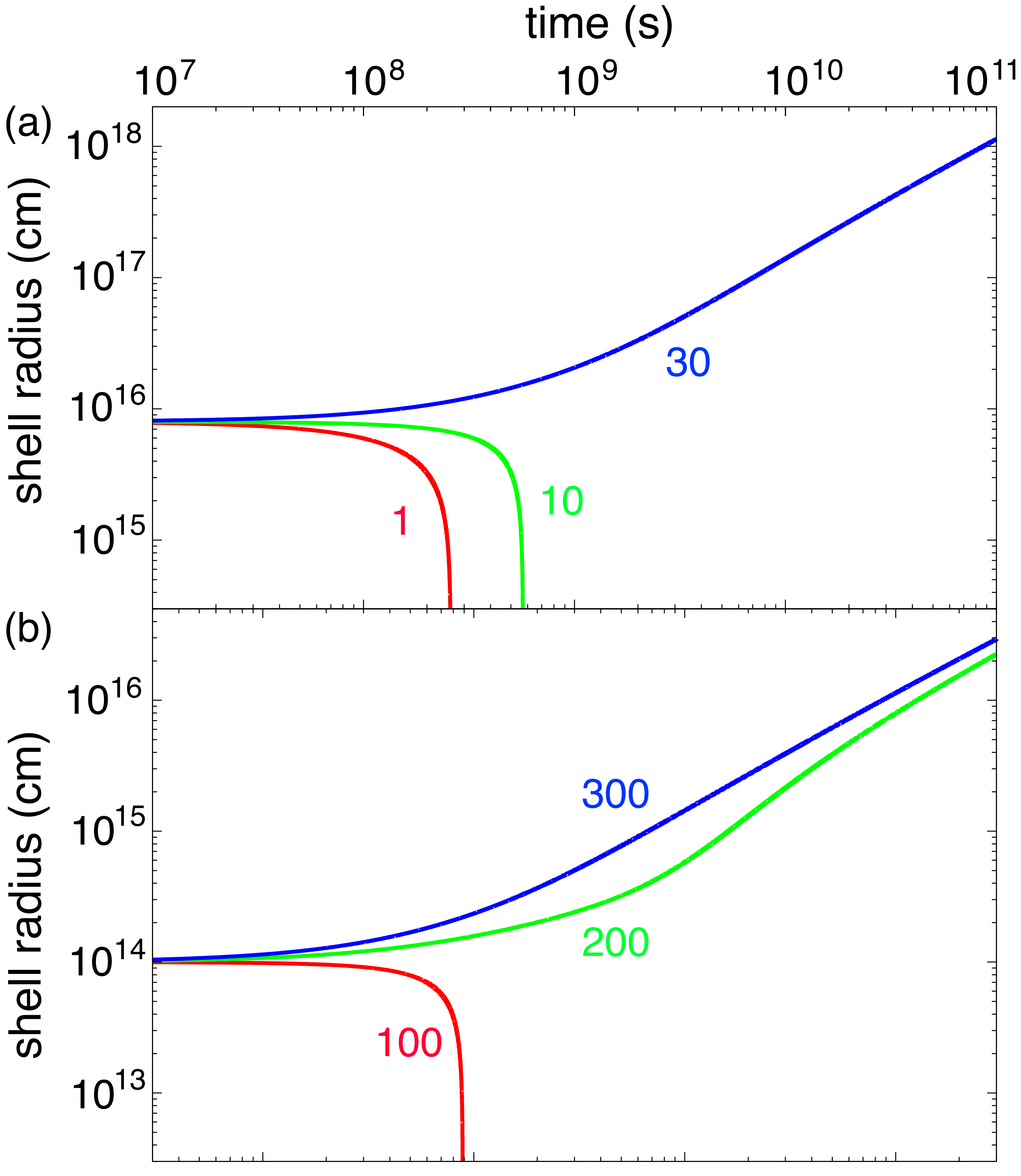

Fig. 4.9 Same as Figure 4.8, but for different values of $R_{\rm sh,0}$ and $f_{\rm Edd}$. The radii of the initial shell and the luminosity are set to (a) $R_{\rm sh,0} = r_{\rm min} (= 8 \times 10^{15}\,{\rm cm})$ and $f_{\rm Edd} = 1$ (red), 10 (green) and 30 (blue), and to (b) $R_{\rm sh,0} = R_{\rm ph} (\simeq 10^{14}\,{\rm cm})$ and $f_{\rm Edd} = 100$ (red), 200 (green) and 300 (blue). The mass of the initial shell is calculated with a constant density profile, and the effects of ram pressure and gravity are both incorporated. This figure is reproduced from Sakurai, Inayoshi & Haiman (2016).

conditions are satisfied. One is

$$\dot{M} \gtrsim 5000\,\dot{M}_{\mathrm{Edd}} = 5000\,L_{\mathrm{Edd}}/c^2, \tag{4.24}$$

(see equation 1.7). The condition is identical to that found in IHO16 who assume that photon trapping effectively limits the luminosity emerging from the central source to $\lesssim L_{\mathrm{Edd}}$. The other new condition determines whether the hyper-Eddington accretion is steady or highly episodic. We find that a steady state is preserved as long as radiation luminosity from the central source is below a critical value,

$$\frac{L}{L_{\mathrm{Edd}}} \lesssim 11 \left(\frac{M_{\mathrm{BH}}}{10^4\,\mathrm{M}_\odot}\right)^{3/2} \left(\frac{n_\infty}{10^5\,\mathrm{cm}^{-3}}\right). \tag{4.25}$$

The condition corresponds to the requirement that ram pressure of the collapsing medium plus BH gravity of the accumulated shell mass at the boundary of the H II region dominate over radiation force, i.e., $\dot{M}|v| \gtrsim L/c$. When the luminosity exceeds this critical value, then a steady hyper-Eddington phase cannot be realized, and the accretion instead becomes episodic. Still, the time-averaged accretion rate matches the unimpeded Bondi rate $\dot{M}_{\mathrm{B}}$, if the condition of equation (4.24) is satisfied. We summarize the three distinct types of accretion flows which are determined by the above two conditions, in Figures 4.6 and 4.7. In this work, we also present a physical interpretation of our simulation results, which can be recovered with a toy model of an optically thick spherical shell, driven by radiation into a collapsing cloud.

For a radiation spectrum, we have assumed a power law with an index of $\alpha = 1.5$ over a frequency range of $13.6\,\mathrm{eV} \leq h\nu \leq 30\,\mathrm{keV}$ (equation 4.13). In this case, all radiation can contribute to ionization of neutral gas. In realistic cases, however, a spectrum of an accretion disk around a BH would have lower energy photons with $h\nu < 13.6\,\mathrm{eV}$ which can escape not ionizing the accreting gas (e.g., Tanaka & Menou 2010). Thus, when assuming a realistic spectrum with a fixed total luminosity, a transition to hyper-Eddington accretion is more likely to occur than in our case.

In our simulations, we do not resolve the photosphere and trapping radius located at small radii. If the accreting gas has a finite angular momentum, a compact accretion disk would form around the central BH. Anisotropic radiation and/or outflows/jets from the center would break the spherical symmetry of the gas inflow, at least in the inner regions. Fully self-consistent treatments of such an accretion flow with an anisotropic bright source of $L > L_{\mathrm{Edd}}$ at the central region, embedded in a nearly spherical inflow at large radii, require multidimensional radiation hydrodynamical simulations.

Chapter 5

Black hole formation via runaway collision in primordial star clusters

5.1 Overview

The formation of massive BHs in the first star clusters via runaway stellar collision is studied. In previous works, first star clusters which can experience the runaway stellar collision process are supposed to be formed in atomic-cooling halos (Table 1.3) which are slightly metal-enriched by supernovae. Although the collision process in first star clusters is previously examined by Katz, Sijacki & Haehnelt (2015), they consider a cluster in a mini-halo and focus on one realization. In order to elucidate whether the runaway stellar collision is prevalent in the early universe, specifically in star clusters within atomic-cooling halos which are more massive than mini-halos, we here consider statistics of atomic-cooling halos and study the collision processes in the clusters. First of all, we identify star-forming gas clouds in protogalactic halos of mass $\gtrsim 10^7\,\mathrm{M}_\odot$, which are deemed as atomic-cooling halos and are assumed to be slightly metal-enriched, by performing cosmological hydrodynamical simulations. We then use them to generate the initial conditions for star clusters of masses $\sim 10^5\,\mathrm{M}_\odot$. We next perform a series of direct-tree hybrid N-body simulations to examine runaway stellar collisions in the star clusters. In all the star clusters but one, runaway collisions occur within a few million years, and the mass of the central massive star which undergoes runaway collisions reaches $\sim 400 - 1900\,\mathrm{M}_\odot$. Such very massive stars collapse after their lifetimes and leave intermediate-mass BHs (IMBHs). The diversity of the final masses can be explained by the differences of the parent cloud properties such as virial mass, central gas density and central gas velocity dispersion. Finally, the IMBH mass to cluster mass ratios are discussed, which are compared with the observed BH to bulge mass ratios in the present-day Universe.

5.2 Numerical methods

We performed the simulations in the following three-step manner. First, we run cosmological hydrodynamical simulations of early galaxy formation. The output is used to locate a number of proto-galactic halos that host a star-forming gas cloud. Then, we replace the gas cloud with a star cluster, assuming that numerous stars with a wide range of masses form in the cloud. We set positions and velocities of the stars by adopting a few simple models. The realizations which are generated in this manner serve as the initial conditions for star cluster evolution simulations. Finally, direct-tree hybrid N-body simulations are performed to follow the stellar dynamics.

Table 5.1 Host halo properties, generated star cluster properties and main results of the star cluster simulations, where we use fiducial model parameters, $\alpha_{\rm sfe} = 6.32 \times 10^{-4}$, $m_{\rm min} = 3\,{\rm M}_\odot$, $m_{\rm max} = 100\,{\rm M}_\odot$, $\beta = 2.35$, $Q = 0.5$ and $m_{\rm DM} = 1.87\,{\rm M}_\odot$. The overlines denote that the values are averaged over 3 realizations. This table is taken from Sakurai et al. (2017).

	z	$R_{\rm vir}$ (pc)	$M_{\rm vir}$ ($10^7\,{\rm M}_\odot$)	$\overline{M}_{\rm cl}$ ($10^4\,{\rm M}_\odot$)	$\overline{N}$ (10^3)	$\overline{r}_{\rm c}$ (pc)	$\overline{\rho}_{\rm c}$ (${\rm M}_\odot\,{\rm pc}^{-3}$)	$\overline{t}_{\rm rh}$ (Myr)	$\overline{t}_{\rm rc}$ (kyr)	$\overline{\epsilon}_{\rm sfe}$ (%)	$M_{\rm DM}$ ($10^7\,{\rm M}_\odot$)	$N_{\rm DM}$ (10^7)	$\overline{m}_{\rm max,f}$ (${\rm M}_\odot$)	$\overline{N}_{\rm coll}$
A	19.7	281	4.03	16.4	19.9	0.401	6.45×10^5	19.7	528	5.91	4.79	2.56	929	11.7
B	19.6	276	2.97	13.0	15.7	0.387	5.82×10^5	12.6	783	6.12	3.78	2.02	409	4.67
C	19.7	208	2.03	12.1	14.7	0.380	8.36×10^5	9.67	67.1	10.1	6.60	3.53	1330	18.3
D	14.9	321	2.60	11.7	14.1	0.357	9.75×10^5	13.6	8.93	7.16	5.67	3.03	971	13.7
E	17.1	264	1.47	4.76	5.76	0.224	1.16×10^6	4.42	2.98	8.15	3.25	1.74	773	9.67
F	16.5	312	2.01	9.00	10.8	0.662	7.05×10^5	15.0	3.62	8.67	5.13	2.74	1100	14.0
G	16.9	242	1.99	12.5	15.0	0.353	1.01×10^6	10.1	4.25	9.48	4.17	2.23	1660	25.0
H	11.7	541	4.22	7.70	9.32	0.276	1.08×10^6	10.8	0.807	5.55	5.25	2.81	964	15.0

Notes 1: Halo properties when the central gas density is $n_{\rm H} = 10^7\,{\rm cm}^{-3}$; column 2: redshift, column 3: virial radii and column 4: virial masses.

Notes 2: Generated star cluster properties; column 5: total stellar mass, column 6: total number of star particles, column 7: core radii, column 8: core density, column 9: half-mass relaxation time (equation 5.3), column 10: relaxation time at the center (equation 5.4), column 11: global SFE $\epsilon = M_{\rm cl}/M_{\rm gas}(< R_{\rm cl})$, wherein $M_{\rm gas}(< r)$ is enclosed gas mass in the original halo data, column 12: total mass of DM and column 13: total number of DM particles. The core radius and density are computed using the method of Casertano & Hut (1985). We calculate the values $r_{\rm c}$, $\rho_{\rm c}$ and $t_{\rm rh}$ using bound particles.

Notes 3: Results in the hybrid N-body simulations; column 14: maximum mass of the star which forms via runaway collision and column 15: number of the collisions to the runaway collision star.

5.2.1 Cosmological simulations

We employ the parallel N-body/SPH code Gadget-2 (Springel 2005), modified as in Hirano et al. (2014) so that primordial gas cloud formation processes can be followed (see also Yoshida et al. 2003, Yoshida, Omukai & Hernquist 2008). The initial condition of the simulations is set at $z_{\rm ini} = 99$ with a box size $10\,h^{-1}$ Mpc employing the MUSIC software (Hahn & Abel 2011). We adopt cosmological parameters from the latest Planck data (Ade et al. 2016: last column of their table 4). We choose the box size to be sufficiently large to locate ~ 10 halos of virial mass $\sim 10^7 - 10^8\,{\rm M}_\odot$ at redshift $z = 10 - 20$ (Reed et al. 2007). A dark matter (DM) only simulation with $N = 512^3$ is first run, and then a friends-of-friends halo finder is run to identify dark halos at $z = 10$. Next, zoom-in simulations are performed for the selected target halos with a high spatial resolution. A mass resolution of $m_{\rm DM} \sim 1\,{\rm M}_\odot$ is achieved with the multilevel zoom-in technique. The resolution is determined by considering that the DM particle mass will become smaller than the minimum stellar mass in the star cluster simulations (Section 5.2.3), which is $m_{\rm min} = 3\,{\rm M}_\odot$ in the fiducial model (Section 5.2.2). The zoom-in simulations are performed including SPH particles and switching off radiative cooling other than atomic hydrogen cooling. We omit molecular hydrogen cooling to prevent gas cloud formation in early mini-halos. We stop the SPH simulations when the target halos gravitationally collapse, and the central gas density becomes $n_{\rm H} \sim 10^7\,{\rm cm}^{-3}$. The simulations are run for eight halos in total whose basic properties are listed in Table 5.1 (column 2-4).

5.2.2 Generation of star cluster plus DM distributions

The initial conditions for the stellar dynamics simulations are directly generated from the outputs of the cosmological zoom-in simulations. A snapshot for each target halo is exported at density of the central gas $n_{\rm H} \sim 10^7\,{\rm cm}^{-3}$. The density corresponds to a critical density of cloud fragmentation when metallicity is $Z \sim 10^{-4}\,Z_{\odot}$ (figure 5 of Omukai, Schneider & Haiman (2008)). It is expected that the cloud would be already gravitationally unstable and yield multiple stars. However, in the zoom-in simulations we do not resolve formation of individual stars, and thus we adopt the following simplified model to locate stars within the parent gas cloud.

We choose a fraction of the SPH particles as 'stars'. A sampled star particle is re-assigned the mass and velocity, while the position is kept the same as that of the original SPH particle. The following five physical parameters are used to determine the sample probability and to compute the stellar mass and velocity: local star formation efficiency (SFE) $\alpha_{\rm sfe}$ which is non-dimensional and controls global SFE, the minimum and maximum stellar mass $m_{\rm min}$ and $m_{\rm max}$, an power-law index β of an initial mass function (IMF) ${\rm d}N/{\rm d}m \propto m^{-\beta}$ and a virial ratio Q (the ratio of the total kinetic energy to the total gravitational energy for the stars). We compute the probability of replacing an SPH particle i with a stellar particle according to the local SFE (Fujii & Portegies Zwart 2015) defined by

$$\epsilon_{{\rm loc},i} = \max\left(\alpha_{\rm sfe}\sqrt{\frac{n_{{\rm H},i}}{1\,{\rm cm}^{-3}}}{\rm e}^{-r_i/R_{\rm cl}}, 1.0\right) \times \frac{m_{{\rm gas},i}}{\overline{m}_{\rm s}}, \tag{5.1}$$

wherein r_i is a SPH particle distance from the maximum density point (cloud center), $R_{\rm cl}$ is a cluster radius which is defined as the radius where the enclosed gas mass is equal to that of DM, $m_{{\rm gas},i}$ is mass of a SPH particle and $\overline{m}_{\rm s}$ is the average stellar mass for the specified IMF. This equation is based on the star formation law of Schmidt (1959), $\dot{\rho}_{\rm star} \propto t_{\rm ff}^{-1}$, where the star formation rate $\dot{\rho}_{\rm star}$ is proportional to the inverse of free-fall time $t_{\rm ff} \propto n_{\rm H}^{-1/2}$. The factor of $m_{{\rm gas},i}/\overline{m}_{\rm s}$ is necessary to guarantee that the stellar mass does not exceed the gas mass after the replacement of the SPH particles to the star particles. The exponential cutoff is employed to set a finite cluster size, but the selection of the value for $R_{\rm cl}$ does not affect the resulting cluster distribution. In order to assign the velocity to individual star particles, we rescale the SPH particle velocity

$$\boldsymbol{v}_{\rm star} = \sqrt{\frac{Q}{T/|W|}}(\boldsymbol{v}_{\rm SPH} - \overline{\boldsymbol{v}}), \tag{5.2}$$

wherein $\boldsymbol{v}_{\rm SPH}$ is the velocity of the SPH particle with the cloud's bulk velocity subtracted, $\overline{\boldsymbol{v}} = \sum_{\rm replaced} m_{\rm star}\boldsymbol{v}_{\rm SPH}/\sum m_{\rm star}$, $m_{\rm star}$ is stellar mass, T is kinetic energy $\sum_{\rm replaced} m_{\rm star}\boldsymbol{v}_{\rm SPH}^2/2$ and W is gravitational energy of the stars. Adopting the fiducial virial ratio $Q = 0.5$, we can achieve a marginally stable cluster. For each sample, three realizations are generated with different random number seeds to select star particles. In total, 24 simulations are performed for our fiducial model. We further perform additional simulations to investigate the effect of model parameters, which will be discussed in Section 5.3.2.

We keep the DM distribution essentially the same as in the original output of the cosmological simulations. We practically split DM particles so that all DM particles have the same mass $m_{\rm DM}$, for which we choose the minimum DM particle mass in the cosmological simulation. The splitting is performed to avoid artificial mass segregation of DM particles when the hybrid N-body simulations are run (Section 5.2.3). In the process of the splitting, we randomly distribute the daughter particles in a sphere with a radius of the mean separation of the DM particle. The daughter particles retain the same velocity as the parent particle. In addition, DM halo's bulk velocity is subtracted and the velocities of the particles are rescaled so that a DM virial ratio becomes 0.5, as in equation (5.2). This prevents the outer part of the DM halo from evaporating in our star cluster simulations.

The fiducial parameters for generation of the initial condition are set to $\alpha_{\rm sfe} = 6.32 \times 10^{-4}$, $m_{\rm min} = 3\,{\rm M}_\odot$, $m_{\rm max} = 100\,{\rm M}_\odot$, $\beta = 2.35$, $Q = 0.5$ and $m_{\rm DM} = 1.87\,{\rm M}_\odot$. We show the resulting star cluster/DM global properties in Table 5.1. The value of the star formation efficiency $\alpha_{\rm sfe}$ is manually chosen so that the particle number in model A becomes about $\sim 2 \times 10^4$. Note that the value of $\alpha_{\rm sfe}$ is just an indicator of the amount of the star formation. By this choice, the global SFE (column 10 in Table 5.1) becomes $\epsilon_{\rm sfe} \sim 0.06 - 0.1$, which is almost consistent with the value of ~ 0.1 found in the hydrodynamical simulations of star clusters within atomic-cooling halos (Kimm et al. 2016). We set Q to 0.5, but this does not necessarily mean that the system is virialized because not all the star particles are bound. We assume the Salpeter mass function throughout this work. Although the minimum stellar mass is set to $m_{\rm min} = 3\,{\rm M}_\odot$, stars with lower masses of $< 1\,{\rm M}_\odot$ may exist in real clusters. Choosing a smaller $m_{\rm min}$ makes the number of star particles very large and computing time of the hybrid N-body simulations impractically long. We examine the effect of varying $m_{\rm min}$, as well as the other parameters, in Section 5.3.2.

5.2.3 Direct-tree hybrid N-body simulations

We perform the stellar dynamics simulations using the hybrid N-body code BRIDGE (Fujii et al. 2007). In the code, orbits of the star particles are followed by a direct method in a dynamically consistent manner with DM particles, motions of which are computed by a tree method. The current version of the code employs the sixth-order Hermite integrator for the direct integration (Nitadori & Makino 2008). Efficient parallelization is realized with the NINJA scheme (Nitadori, Makino & Abe 2006). We use the PHANTOM-GRAPE library (Tanikawa et al. 2013) to speed up the gravitational force computation.

We allow a pair of stars to collide and merge when its separation $d \equiv |\boldsymbol{r}_1 - \boldsymbol{r}_2|$ is less than the sum of the stellar radii $R_{*,1} + R_{*,2}$, i.e., $d < R_{*,1} + R_{*,2}$. The merger criterion or the so-called 'sticky-sphere' approximation is well tested by Gaburov, Lombardi & Portegies Zwart (2010), who found that the criterion gives $\sim$ 75 per cent accurate results when compared to the results of hydrodynamical simulations of stellar three-body interactions.

We use the stellar radii of the fitting formula from Tout et al. (1996) for the non-evolving zero-age main-sequence stars with $Z = 0.02$. The formula which is valid for stellar mass of $\leq 100\,{\rm M}_\odot$ is extrapolated to larger stellar mass, resulting in possible underestimations of the radii, especially for very massive stars. For instance, the stellar radii for stellar mass 100, 200, 500 and $1000\,{\rm M}_\odot$ from the formula in Tout et al. (1996) are 17, 28, 54 and $87\,R_\odot$, respectively, while the radii from the interior structure calculations for massive stars in Ishii, Ueno & Kato (1999) are 18, 40, 160 and $3000\,R_\odot$ and those from Yungelson et al. (2008) are 14, 27, 66 and $129\,R_\odot$. Note that stellar radii are generally smaller for lower metallicity stars (e.g., Baraffe & El Eid 1991, Baraffe, Heger & Woosley 2001). Although a stellar radius model for $Z = 10^{-4}\,Z_\odot$ could be technically constructed as in Katz, Sijacki & Haehnelt (2015), we use the Tout's fitting formula for the solar metallicity for simplicity. The effect of adopting a different model of stellar radii is examined in Section 5.3.2.

We present parameters for the N-body simulations in Table 5.2, where η is an integration accuracy parameter (see equation 16 of Nitadori & Makino 2008), Δt is a tree time step, $L_{\rm box}$ is a box size in the simulations, $n_{\rm crit}$ is the maximum group size in GRAPE calculation (Makino 1991), θ is a tree opening angle and $\epsilon_{\rm cl}$ and $\epsilon_{\rm DM}$ are softening lengths for calculating gravity of stars and

Table 5.2 Parameters for the hybrid N-body simulations. This table is taken from Sakurai et al. (2017).

η	Δt (yr)	$L_{\rm box}$ (pc)	$n_{\rm crit}$	θ	$\epsilon_{\rm cl}$ (pc)	$\epsilon_{\rm DM}$ (pc)
0.11	1.16×10^3	1024/2048	512	0.5	0	0.0313

DM respectively. We choose the accuracy parameter η so that errors of the total energy during the simulations do not exceed 0.04 per cent. The box size of the simulations $L_{\rm box}$ is set to 1024 or 2048 pc, which is chosen to encompass all the particles during the simulations. We check convergence of the results with varying Δt, $L_{\rm box}$ and $\epsilon_{\rm DM}$. We stop the simulations at $t = 3\,{\rm Myr}$, when the central massive star is considered to end its life.

5.3 Results

We summarize the properties of the eight halos in Table 5.1. The virial masses are $\sim (1.5\text{–}4)\times 10^7\,{\rm M}_\odot$ and the formation redshifts are $z = 11 - 20$. In Figure 5.1, we represent the gas distribution of Halo B (top panels) and G (bottom panels), respectively. In Halo B the features of turbulent motions are seen in the gas distribution, whereas in Halo G the gas appears dynamically relaxed, and is nearly spherical. We also show the generated stellar distributions in the right-hand panels of Figure 5.1. Most of the stars reside within the central few parsec region, but a small number of stars are found in the outer region.

5.3.1 Fiducial models

The initial stellar mass in the clusters ranges from $\sim 5 \times 10^4\,{\rm M}_\odot$ to $\sim 1.6 \times 10^5\,{\rm M}_\odot$ for our fiducial models (see Table 5.1).

In Figure 5.2, we show time evolution of the cluster core radii. The core radii are computed following the procedure of Casertano & Hut (1985). The core contracts quickly within $\sim$ a million years due to the short crossing time $t_{\rm cr} \equiv r_{\rm h}/\sigma \lesssim 0.1\,{\rm Myr}$ of the cluster systems with a typical half-mass radius $r_{\rm h} \sim 1\,{\rm pc}$ and three-dimensional velocity dispersion $\sigma \sim 10\,{\rm km\,s^{-1}}$.

In Figure 5.2, the evolution of $r_{\rm h}$ is also plotted. The radii $r_{\rm h}$ remain roughly constant with time, suggesting that the runaway collision is triggered by core collapse and not driven by cold collapse of the entire cluster because of the initially non-equilibrium configuration.

Core-collapse time $t_{\rm cc}$, which we define by the time when the core radius has its minimum, ranges from $\lesssim 0.1$ to $\sim 2.7\,{\rm Myr}$ in our 24 simulations. When the times $t_{\rm cc}$ are rewritten in terms of the half-mass relaxation time $t_{\rm rh}$ (Table 5.1),

$$t_{\rm rh} = \frac{0.651\,{\rm Gyr}}{\ln(\gamma N)} \frac{1\,{\rm M}_\odot}{\overline{m}_{\rm s}} \left(\frac{M_{\rm cl}}{10^5\,{\rm M}_\odot}\right)^{1/2} \left(\frac{r_{\rm h}}{1\,{\rm pc}}\right)^{3/2}, \tag{5.3}$$

wherein $M_{\rm cl}$ is cluster mass and γ is ~ 0.015 for a system with a wide mass spectrum (Giersz & Heggie 1996, Gürkan, Freitag & Rasio 2004), it is found that $t_{\rm cc}$ ranges from $\lesssim 0.01$ to $\sim 0.2\,t_{\rm th}$.

It is expected that the core-collapse time $t_{\rm cc}$ is proportional to the central relaxation time-scale (Gürkan, Freitag & Rasio 2004, Fujii & Portegies Zwart 2014: see Table 5.1),

$$t_{\rm rc} = \frac{0.065\sigma_{\rm c}^3}{G^2 \overline{m}_{\rm s} \rho_{\rm c} \ln \gamma N}, \tag{5.4}$$

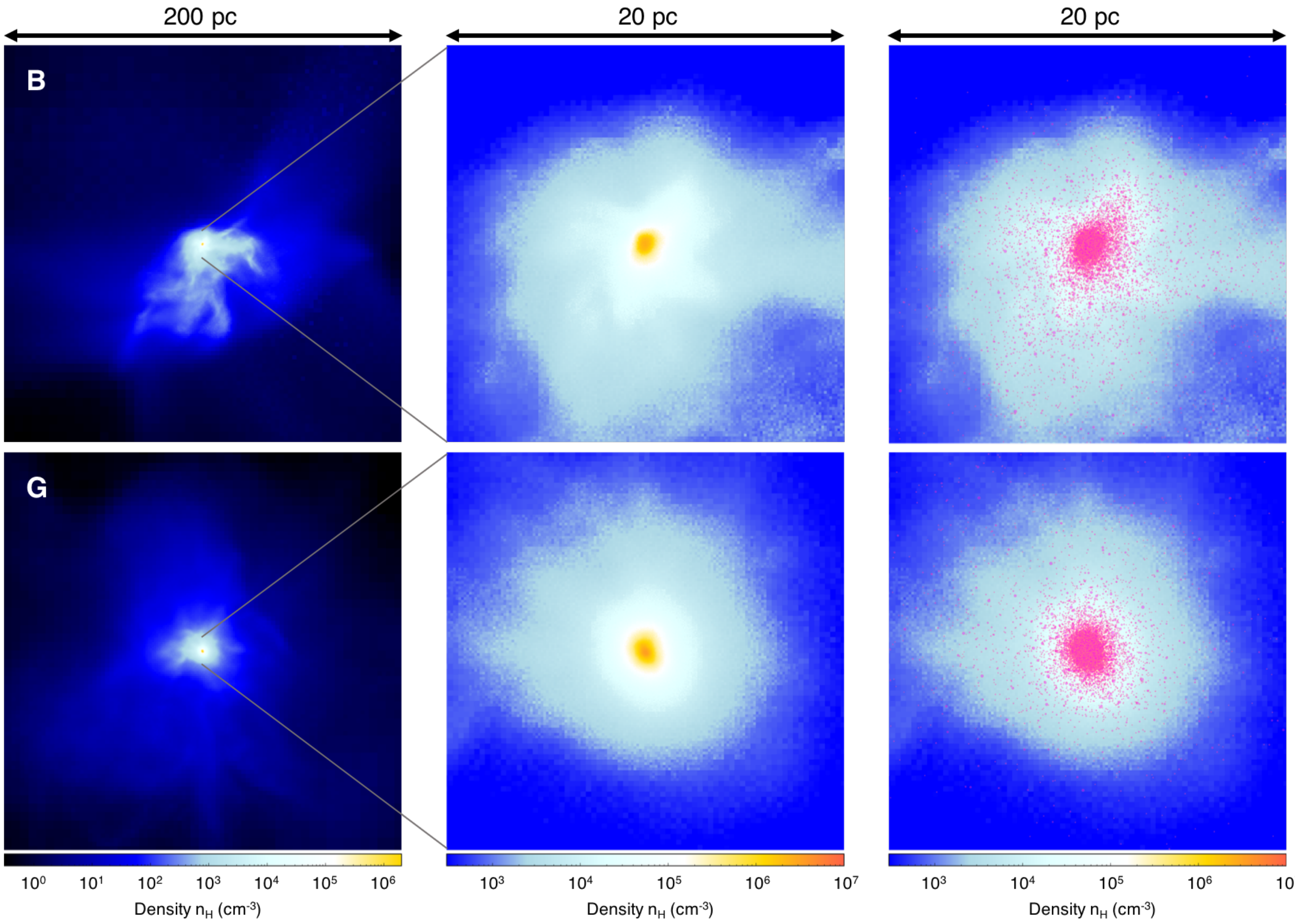

Fig. 5.1 The projected gas density distributions are plotted for Halo B (top panels) and G (bottom panels). The region size is 200 pc (left-hand panels) and 20 pc (middle and right-hand panels). The generated stellar distributions (magenta dots) are also compared on the right-hand panels. This figure is reproduced from Sakurai et al. (2017).

wherein σ_c is the three-dimensional velocity dispersion at a cluster center, which we compute using central 20 stars. We find that t_{cc} ranges from ~ 2 to $200\, t_{rc}$. In contrast to the result found in Fujii & Portegies Zwart (2014), significant scatter is found in the ratio of t_{cc}/t_{rc} even though $m_{max}/\overline{m}_s$ is fixed. This scatter could be attributed to the variation in the compactness of the initial stellar distribution.

In Table 5.1, we show the final stellar mass $m_{max,f}$ and the number of stellar collisions N_{coll} by $t = 3\, M_\odot$. In all the runs, runaway collision occurs with $N_{coll} \sim 5-25$ and the final mass of the stars exceeds the threshold mass $\sim 300\, M_\odot$ for gravitational collapse (Heger et al. 2003, Yoon, Dierks & Langer 2012, Spera & Mapelli 2017); remnants would be IMBHs of similar masses. Figure 5.3 shows time evolution of the mass of the central star which undergoes runaway collisions. The analytical model of the mass evolution from Portegies Zwart & McMillan (2002) is also shown:

$$m = m_{seed} + 4 \times 10^{-3}\, M_{cl} f_c \ln\Lambda \ln\left(\frac{t}{t_{cc}}\right), \tag{5.5}$$

wherein m_{seed} is seed mass of a star which starts a runaway process, f_c is a fraction of binaries which contribute to collisions and $\ln\Lambda$ is a Coulomb logarithm. This equation is derived by integration of a mass growth rate, which is essentially an average mass increase per collision times an average collision rate of binaries. In our simulations, the rate of mass accumulation via collisions is well described by the model.

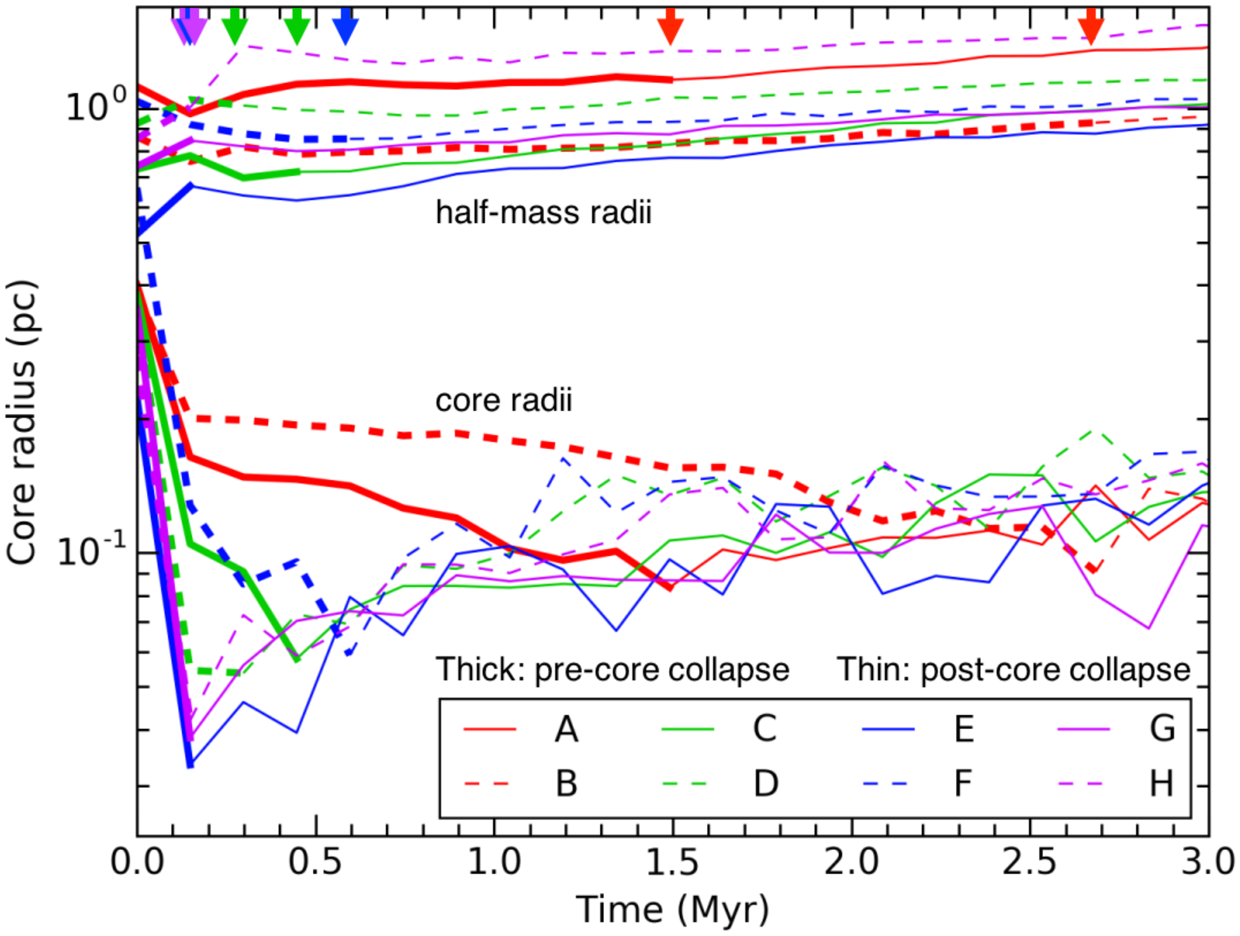

Fig. 5.2 Time evolution of the core radii and the half-mass radii in the eight models A to H. The thick lines represent pre-core-collapse phases, while the thin lines denote post-core-collapse phases. The arrows indicate the core-collapse time which is defined as the time when the core radius is smallest. This figure is reproduced from Sakurai et al. (2017).

5.3.2 Model parameter dependence

We examine how the initial configuration and the values of the model parameters (Section 5.2.2) affect the results. To this end, models with different parameter values or with different setups are considered: models without DM particles (AnoDM), with smaller stellar radii (Arad), with different values of mass limits for the same Salpeter IMF (Amax and Amin) and with different SFE parameter values $\alpha_{\rm sfe}$ (Asfe1, Asfe2 and Asfe3). We summarize the adopted parameter values and the resulting initial properties of the star clusters in Table 5.3.

First, we compare model A and AnoDM. The existence of a DM halo clearly has minor impact on the runaway growth of the stars. This result is expected since the characteristic time of dynamical friction between stars and DM is long. We derive the dynamical friction time $t_{\rm df}$ by considering frictional force on a star of mass m and velocity v in a matter field with a density profile $\rho(r)$ (Binney & Tremaine 2008), and by using the equation of angular momentum change (Fujii & Portegies Zwart 2014), as

$$t_{\rm df} = \frac{0.186 v^3}{G^2 m \ln \Lambda'} \int_0^{r_{\rm ini}} \frac{{\rm d}r}{r\rho}, \tag{5.6}$$

wherein $\Lambda' \simeq 0.1\,N$ (Giersz & Heggie 1994) and $r_{\rm ini}$ is an initial radial position of the star. Adopting

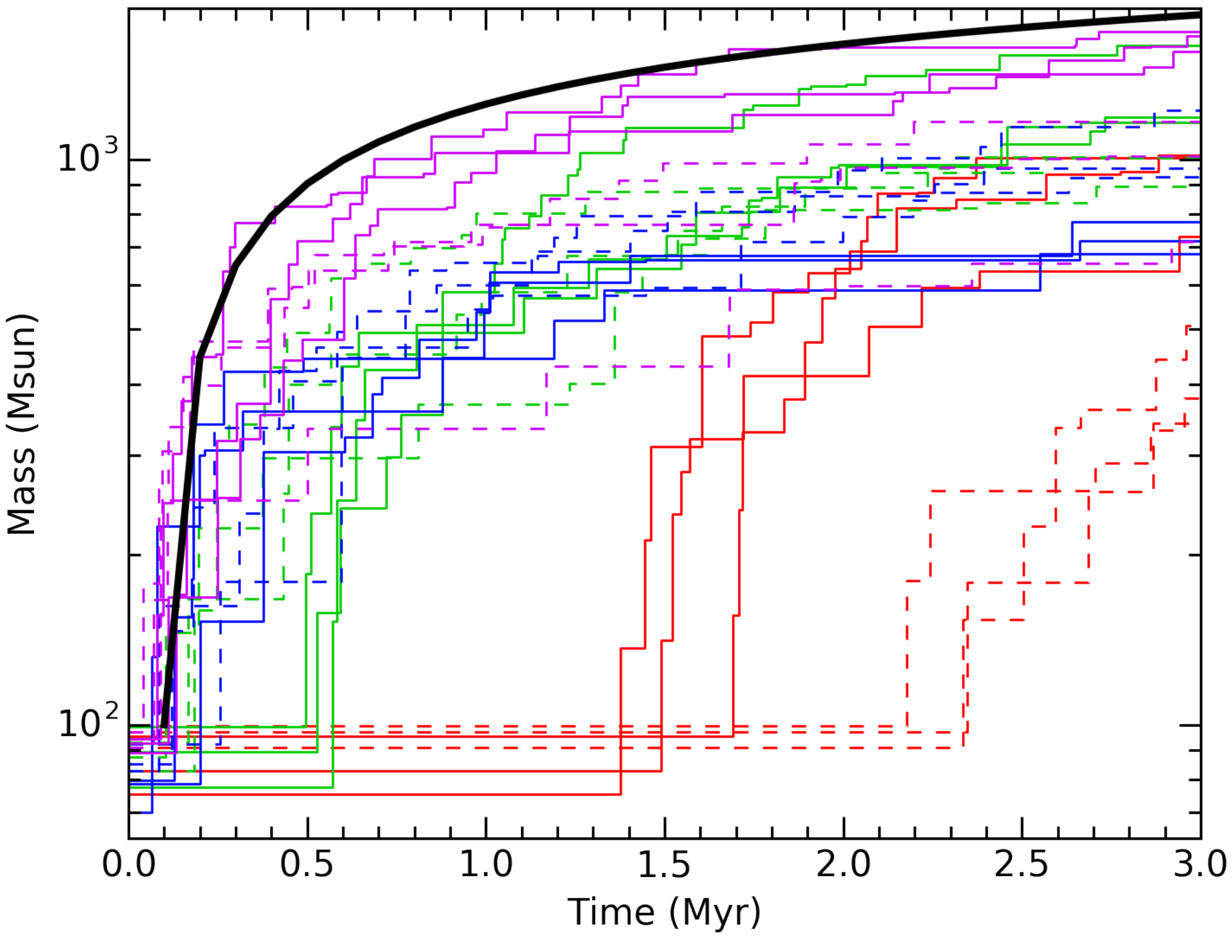

Fig. 5.3 Time evolution of masses of the stars which undergo runaway collisions at the cluster center. We plot the analytical expression of equation (5.5) (black line) for the model G with $m_{\mathrm{seed}} = 100\,\mathrm{M}_{\odot}$, $M_{\mathrm{cl}} = 1.25 \times 10^5\,\mathrm{M}_{\odot}$, $t_{\mathrm{cc}} = 0.1\,\mathrm{Myr}$ and $f_{\mathrm{c}} \ln \Lambda = 1$. The types of the lines and colors are the same as in Figure 5.2. This figure is reproduced from Sakurai et al. (2017).

Table 5.3 Star cluster models with different parameter values. We describe the main difference from the fiducial model in the last column. The values of M_{DM} and N_{DM}, when DM is included, are the same as in the corresponding fiducial model and are not shown in this table. We note that the initial stellar distributions in model AnoDM and Arad are exactly the same as in our fiducial model A. Unless mentioned, the values are computed by averaging over three realizations. This table is taken from Sakurai et al. (2017).

	$\overline{M}_{\mathrm{cl},4}$ ($10^4\,\mathrm{M}_{\odot}$)	$\overline{N}_3$ (10^3)	$\bar{r}_{\mathrm{c}}$ (pc)	$\bar{\rho}_{\mathrm{c},5}$ ($\mathrm{M}_{\odot}\,\mathrm{pc}^{-3}$)	$\bar{t}_{\mathrm{rh}}$ (Myr)	$\bar{t}_{\mathrm{rc}}$ (kyr)	$\bar{\epsilon}_{\mathrm{sfe}}$ (%)	$\overline{m}_{\mathrm{max,f}}$ ($\mathrm{M}_{\odot}$)	$\overline{N}_{\mathrm{coll}}$	Notes
A	16.4	19.9	0.401	6.45×10^5	19.7	528	5.91	929	11.7	fiducial model (Table 5.1)
AnoDM	16.4	19.9	0.401	6.45×10^5	19.7	528	5.91	915	10.7	no DM
Arad	16.4	20.0	0.400	6.30×10^5	19.5	553	5.90	958	9.00	half radii for stars, 1 realization
Amax	16.5	18.6	0.394	7.31×10^5	17.2	157	5.95	1510	11.0	$m_{\mathrm{max}} = 200\,\mathrm{M}_{\odot}$, 1 realization
Amin	16.6	53.3	0.401	7.94×10^5	44.6	1040	5.99	980	12.0	$m_{\mathrm{min}} = 1\,\mathrm{M}_{\odot}$, no DM, 1 realization
Asfe1	28.5	34.5	0.509	5.47×10^5	48.3	511	10.3	1060	14.5	$\alpha_{\mathrm{sfe}} = 1.26 \times 10^{-3}$, 2 realizations
Asfe2	8.56	10.4	0.359	4.47×10^5	12.7	351	3.09	602	5.67	$\alpha_{\mathrm{sfe}} = 3.16 \times 10^{-4}$
Asfe3	1.75	2.10	0.361	8.51×10^4	8.61	144	0.629	186	1.67	$\alpha_{\mathrm{sfe}} = 6.32 \times 10^{-5}$

the inner part of the Navarro-Frenk-White DM halo density profile $\rho \propto r^{-1}$ with normalization $\rho_0 \sim 7 \times 10^{-20}\,\mathrm{g\,cm^{-3}}$ at 1 pc, which is obtained directly from our simulation, and adopting $v = 10\,\mathrm{km\,s^{-1}}$, $r_{\rm ini} = 1\,\mathrm{pc}$, $m = 100\,\mathrm{M_\odot}$ and $N = 3 \times 10^7$, we get $t_{\rm df} \sim 7\,\mathrm{Myr}$, which is several dozen to hundred times longer than $t_{\rm cc}$. Hence, the DM dynamical friction has little effect on the stellar dynamics.

Next, model A and Arad are compared which differ from each other in stellar radius calculation. In model Arad, stellar radii for given stellar masses are half times smaller than in model A. The difference causes only modest impact on the results. In specific, the number of collisions in model Arad becomes slightly smaller, but the final stellar mass $m_{\rm max,f}$ is almost the same.

In model Amax, where we set a larger maximum mass limit of the Salpeter IMF $m_{\rm max}$, we can see a more direct effect: the runaway growth of the massive star at the center is accelerated. By contrast, setting a smaller $m_{\rm min}$ (model Amin) has minor effect on the runaway process. These results are totally reasonable since mainly massive stars undergo the runaway collision process via mass segregation/concentration towards the cluster center.

Changing the values of the SFE parameter $\alpha_{\rm sfe}$ notably alters the results. Adopting a higher SFE (model Asfe1) accelerates runaway collision because an initially denser cluster forms, while setting a smaller $\alpha_{\rm sfe}$ results in smaller $m_{\rm max,f}$ and $N_{\rm coll}$ (Asfe2 and Asfe3). In model Asfe3, there are actually few collisions, and the runaway collision does not occur due to the small cluster mass (see the small value of the second term in equation 5.5).

5.4 Summary and discussions

We have performed simulations for evolution of star clusters and explored IMBH formation via runaway collisions. The star cluster formation sites are found in realistic cosmological simulations. Runaway stellar collisions commence quickly within 3 Myr, and very massive stars of $m_{\rm max,f} \sim 400 - 1900\,\mathrm{M_\odot}$ form (Figure 5.3), which is consistent with the results of Katz, Sijacki & Haehnelt (2015). The final mass $m_{\rm max,f}$ exceeds $\sim 300\,\mathrm{M_\odot}$ in all our fiducial models, and therefore IMBHs will be left in the clusters after the lifetime of the stars (Heger et al. 2003). The IMBHs could be seeds for the formation of SMBHs observed at $z \gtrsim 6$, which are supposed to grow via gas accretion or merger. Provided that Eddington accretion is sustained with radiative efficiency 10 per cent, a seed BH of mass $1000\,\mathrm{M_\odot}$ grows to as massive as $\sim 10^9\,\mathrm{M_\odot}$ in $\sim 0.6\,\mathrm{Gyr}$. We conclude that formation of IMBHs in dense star clusters offers a viable mechanism for seeding the high-z SMBHs.

5.4.1 Correlation between the final mass and halo properties

We examine the origin of the diversity of $m_{\rm max,f}$ (see Table 5.1) found in our simulations by searching correlations between $m_{\rm max,f}$ and several halo properties. Relevant physical quantities will be the halo virial mass $M_{\rm vir}$, gas velocity dispersion at the center $\sigma_{\rm c,gas}$ and average gas density of central core region $\overline{\rho}_{\rm c,gas}$. We naively expect that the cluster mass scales with the halo mass $M_{\rm cl} \propto M_{\rm vir}$ and the star cluster density scales with the central gas density $\rho_{\rm c} \propto \overline{\rho}_{\rm c,gas}$. We also expect $\sigma_{\rm c} \propto \sigma_{\rm c,gas}$ by dynamical consideration. We here essentially assume that the bulk properties of the star clusters come from those of the parent gas clouds. With these scalings and the fact that the core-collapse time $t_{\rm cc}$ scales with the relaxation time $t_{\rm rc}$, we can rewrite equation (5.5) using $M_{\rm vir}$, $\overline{\rho}_{\rm c,gas}$ and $\sigma^3_{\rm c,gas}$ as

$$m_{\rm max,f} \propto M_{\rm vir} \ln(\mathrm{const.} \times \overline{\rho}_{\rm c,gas}/\sigma^3_{\rm c,gas}), \tag{5.7}$$

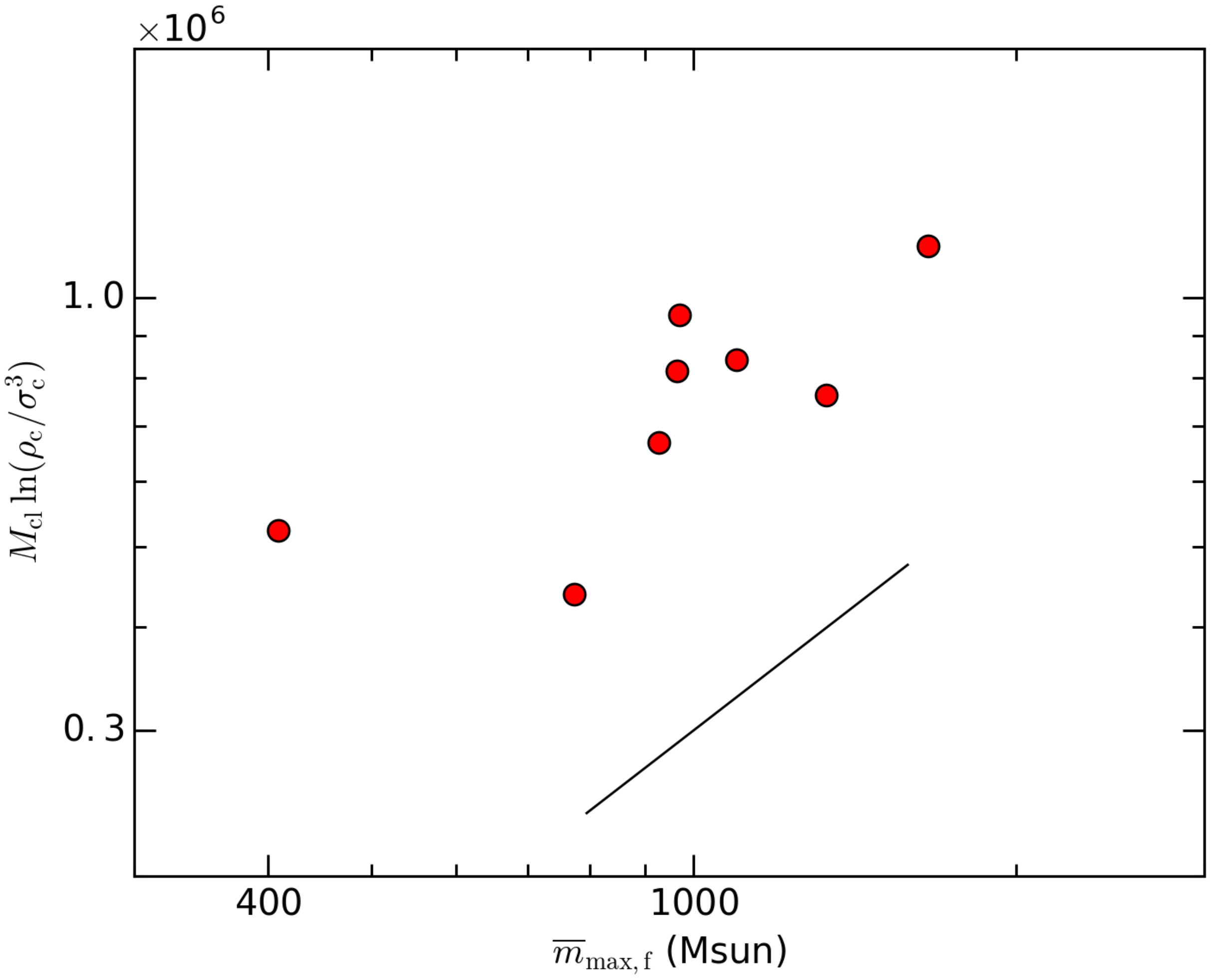

Fig. 5.4 Correlation between $m_{\rm max,f}$ and $M_{\rm cl}\ln(\rho_{\rm c}/\sigma_{\rm c}^3)$. The units of $M_{\rm cl}$, $\sigma_{\rm c}$ and $\rho_{\rm c}$ are $\mathrm{M}_\odot$, $\mathrm{km\,s^{-1}}$ and $\mathrm{M_\odot\,pc^{-3}}$, respectively. The solid line is $\propto m_{\rm max,f}$. This figure is reproduced from Sakurai et al. (2017).

where we use $t = 3\,\mathrm{Myr}$. The logarithmic dependence of $\sigma_{\rm c}$ and $\rho_{\rm c}$ comes from the integration of the mass growth rate via stellar collisions $\propto t^{-1}$ over a time interval between $t_{\rm cc} \propto t_{\rm rc} \propto \sigma_{\rm c}^3$ and $t = 3\,\mathrm{Myr}$ (Portegies Zwart & McMillan 2002). In Figure 5.4, we show the correlation between $m_{\rm max,f}$ and $M_{\rm cl}\ln(\rho_{\rm c}/\sigma_{\rm c}^3)$ for our fiducial models. It is found that $m_{\rm max,f}$ is correlated with the halo properties with moderate scatter, as in equation (5.7).

As a reference, in Figure 5.5, we also show a simpler correlation, namely, a correlation between $m_{\rm max,f}$ and $M_{\rm cl}$. The scatter of the correlation is larger than that from equation (5.7).

A simple redshift dependence of $m_{\rm max,f}$ is also derived as follows. In the derivation, we use the cosmological scaling of halo properties and redshift as in, for instance, equation (18)-(20) of Ahn & Shapiro (2007), i.e., $M_{\rm vir} \propto (1+z)^{-3/2}$ with virial temperature $T_{\rm vir} \sim 8000\,\mathrm{K}$, $\overline{\rho}_{\rm c,gas} \propto (1+z)^3$ and $\sigma_{\rm c,gas} \propto \sigma_{\rm gas} \sim (GM_{\rm vir}/r_{\rm t})^{1/2} \propto M_{\rm vir}^{1/3}(1+z)^{1/2}$. From these scalings, we get

$$m_{\rm max,f} \propto (1+z)^{-3/2}\ln(1+z). \tag{5.8}$$

In Figure 5.6, we show the correlation between $m_{\rm max,f}$ and the cluster formation redshift z. Again, it is found that the actual dependence is consistent with the above scaling (dashed line) although there is substantial scatter. In spite of these interesting correlations, we argue that, in order to determine more accurate correlations, simulations with a large number of samples are necessary.

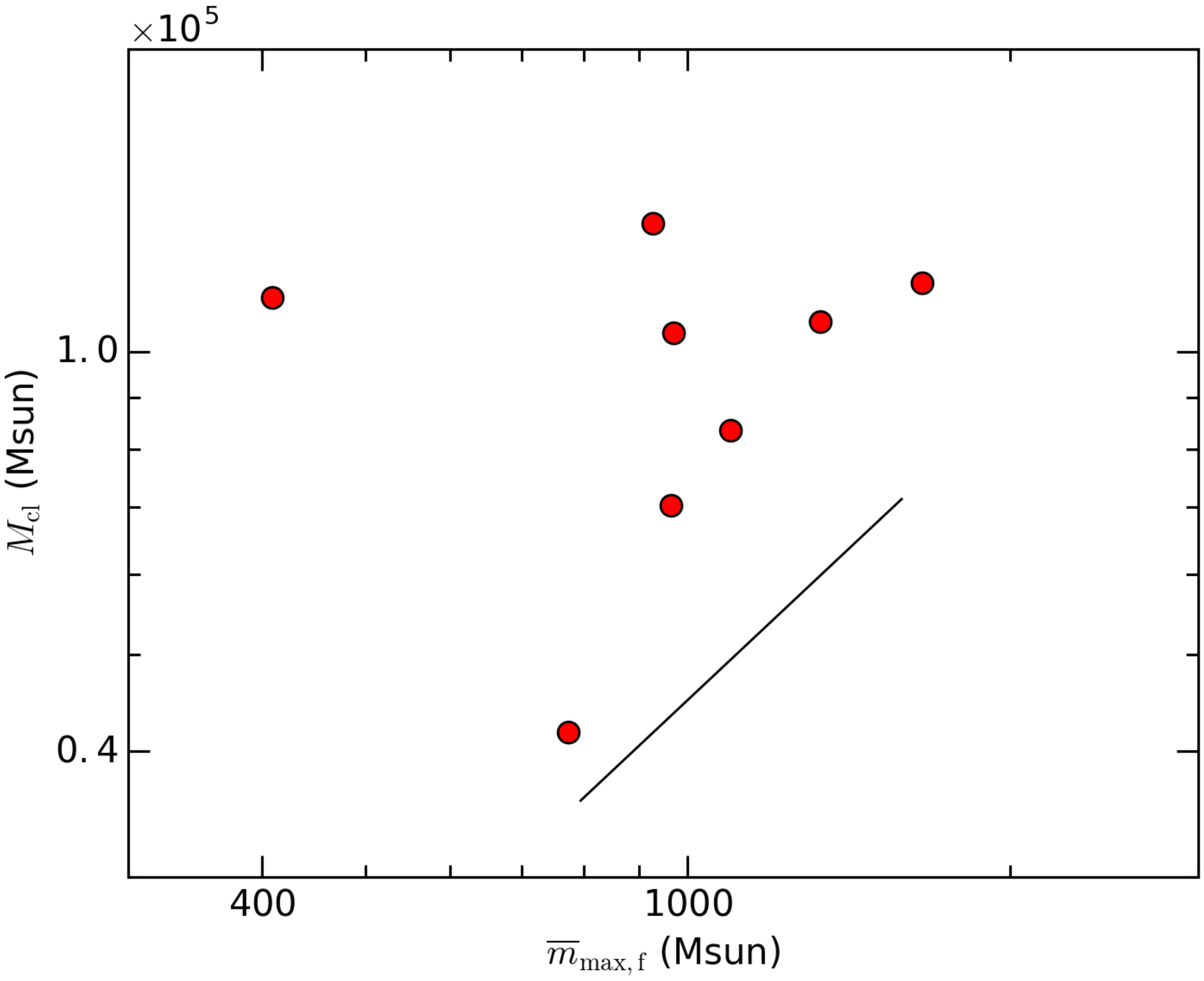

Fig. 5.5 Correlation between $m_{\rm max,f}$ and $M_{\rm cl}$. The solid line is $\propto m_{\rm max,f}$.

5.4.2 Cluster mass-IMBH mass relation

For galaxies and their central BHs, there is a well-known relation between SMBH mass and bulge mass (Magorrian et al. 1998, Merritt & Ferrarese 2001). Although the objects and mass scales are different, we compare the IMBH mass with the cluster mass in our simulations. Figure 5.7 shows the relation between the cluster mass $\overline{M}_{\rm cl}$ and the final mass $m_{\rm max,f}$ of the runaway collision stars which would collapse and leave IMBHs with little mass loss. Our simulation data are located in the left-hand bottom portion of the figure. The lower dotted line denotes the well-known Magorrian relation for SMBHs (from equation 10 of Kormendy & Ho 2013), while the upper dashed line represents the BH mass-cluster mass relation (see equation 16 and figure 3 of Portegies Zwart & McMillan 2002). The latter relation is specifically given by

$$m_{\rm max,f} = 30 + 8 \times 10^{-4} M_{\rm cl} \ln \Lambda_{\rm cl}, \tag{5.9}$$

with $\Lambda_{\rm cl} = \min(M_{\rm cl}/{\rm M}_\odot, 10^6)$. Our simulation results agree with this relation, namely, about one percent of the cluster mass contributes to the mass of the central massive star. Comparing the simulation data with the observational data, we find that the primordial star clusters forming in early atomic-cooling halos may be similar to present-day star clusters, but with smaller masses. We also find that the ratio of central BH mass to galaxy (cluster) mass is slightly higher than that found for local SMBHs, possibly reflecting the different formation mechanism.

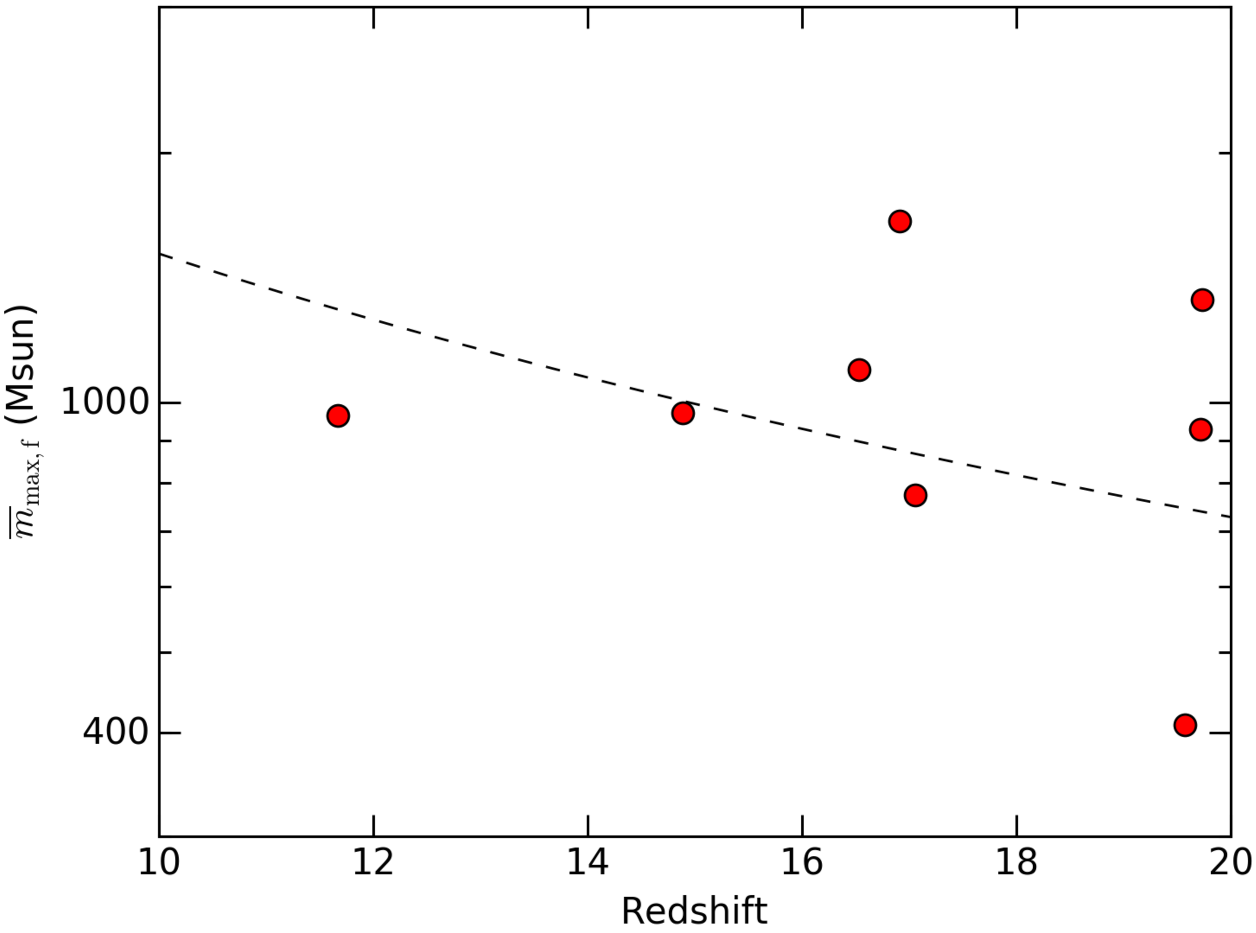

Fig. 5.6 Correlation between redshift z and $m_{\mathrm{max,f}}$ is shown. The dashed line represents a relation of $\propto (1+z)^{-3/2}\ln(1+z)$ (equation 5.8). This figure is reproduced from Sakurai et al. (2017).

5.4.3 Model uncertainties

In this work, the most significant uncertainty lies in the generation process of the initial conditions for star clusters (Section 5.2.2). First, the epoch when a entire gas cloud would be replaced by a star cluster is not trivial. We assume that the cluster forms when density of the gas cloud reaches $n_{\mathrm{H}} \sim 10^7\,\mathrm{cm}^{-3}$. We use the density value by noting that efficient cooling and fragmentation of gas by OH cooling occur in a cloud with metallicity $\gtrsim 10^{-4}\,Z_{\odot}$ (Chiaki, Yoshida & Hirano 2016). Although protostellar formation will occur at much higher density $\gtrsim 10^{20}\,\mathrm{cm}^{-3}$, a lower density threshold for 'star cluster' formation is adopted to trace the global structure of the parent cloud. We also note that starburst in star clusters does not occur instantaneously but can last for over a million years (Kimm et al. 2016). Successive star formation can promote runaway collisions by supplying newly formed stars to the cluster, or delayed star formation may actually prevent the growth of the central star. Moreover, a newly born star cluster is not necessarily virialized with $Q = 0.5$, and could have somewhat anisotropic velocity structure. Finally, the SFE will be controlled by stellar evolution itself through various feedback effects. Self-consistent treatment of the star cluster formation and evolution is beyond the scope of this work. However, direct cosmological simulations which couple star formation and stellar dynamics as well as DM halo assembly will elucidate many of the above issues.

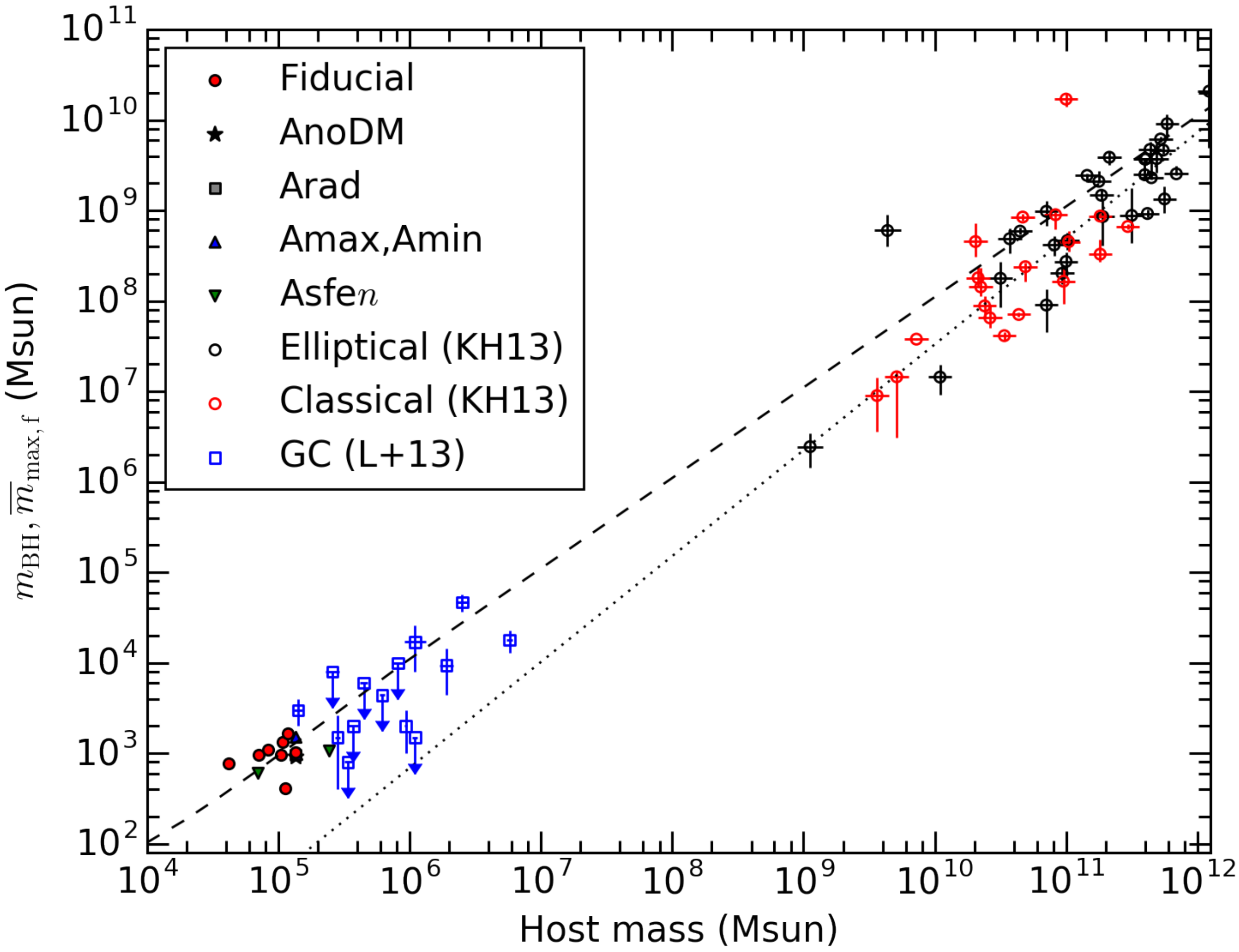

Fig. 5.7 Correlation between $\overline{M}_{\rm cl}$ and $\overline{m}_{\rm max,f}$ for the models in Table 5.1 and Table 5.3. We exclude the model Asfe3 because the massive star of mass $\overline{m}_{\rm max,f} \lesssim 300\,{\rm M}_\odot$ would end its life as a pair instability supernova (Heger et al. 2003). We also over-plot the observational data for elliptical and classical bulges (Kormendy & Ho 2013) and globular clusters (Lützgendorf et al. 2013). The analytical expressions of the BH mass-cluster mass relation (equation 5.9; dashed line) and the Magorrian relation (equation 10 of Kormendy & Ho 2013; dotted line) are also represented. This figure is reproduced from Sakurai et al. (2017).

In our hybrid N-body simulations, several physical processes are not incorporated. First of all, the collision rate is likely to be affected by stellar evolution through the stellar radius evolution and mass loss. As we have already investigated in Section 5.3.2, the uncertainty in the stellar radii of main sequence stars modestly affects our results. When post-main sequence evolution is taken into account, the collision can be enhanced during the giant phases of the stars. We expect that stellar wind and mass loss are not significant over a short time of $\sim 3\,{\rm Myr}$, assuming that the stellar metallicity is as low as $\lesssim 10^{-4}\,Z_\odot$ (Baraffe, Heger & Woosley 2001, Muijres et al. 2012, Katz, Sijacki & Haehnelt 2015). Next, binary evolution increases the merger rate via tidal interaction (Hurley, Tout & Pols 2002), and can promote runaway collisions. In this case, formation of massive stars can occur even faster than in our simulations. Moreover, primordial binaries may delay core collapse of the star clusters by binary heating (Rasio, Fregeau & Joshi 2001), or may accelerate the core collapse by enhancing mass segregation because of the effectively increased mass (Heggie, Trenti & Hut 2006). Finally, the stellar collision condition and outcome may not be as simple as those we have adopted (Section 5.2.3). Effects of tidal interaction can increase the rate of close encounters (Fregeau et al. 2004: and references therein), whereas mass loss during binary collision would reduce the mass of the collision product (Glebbeek et al. 2009). Rejuvenation of stars by collisional mixing lengthens the lifetime of the collision products. An encounter of a pair of stars with high velocities which satisfy our merger condition could actually just pass through each other depending on the impact parameter and the stellar envelope thickness. Most of such stars which once escape merger are in tight binary orbits, and therefore they may eventually merge at later time. Stellar-gas interaction may enhance core collapse if dynamical friction or mass increase by accretion is effective. We estimate a dynamical friction time scale of equation (5.6) for gas to be $t_{\rm df} \sim 0.2\,{\rm Myr}$, adopting an isothermal sphere profile $\rho = \rho_0 (r/r_0)^{-2}$ with $\rho_0 \sim 2 \times 10^{-18}\,{\rm g\,cm^{-3}}$ at $r_0 = 1\,{\rm pc}$ which we derive from the halo data, and using $m = 100\,{\rm M_\odot}$, $v = 10\,{\rm km\,s^{-1}}$, $r_{\rm ini} = 1\,{\rm pc}$ and $\ln \Lambda' \sim 10$. We also estimate an accretion time scale defined by $t_{\rm acc} = m/\dot{m}_{\rm B}$, wherein m is a typical stellar mass and $\dot{m}_{\rm B}$ is the Bondi accretion rate of equation (4.17). For $m = 10\,{\rm M_\odot}$, and using gas temperature $\sim 10^4\,{\rm K}$ and density $n_{\rm H} \sim 10^7\,cm^{-3}$ which are indicated in Kimm et al. (2016), we get $t_{\rm acc} \sim 1\,{\rm Myr}$. Both $t_{\rm df}$ and $t_{\rm acc}$ are within 3 Myr and the presence of gas may accelerate the core collapse of the star clusters.

5.4.4 Fate of IMBHs in star clusters

The formation of very massive stars via runaway collision in dense star clusters has been successfully shown and the stars will undergo direct gravitational collapse to leave IMBHs. Thus, the runaway stellar collision is a promising initial process of seeding the formation of SMBHs. However, there still remains an important question, i.e., it is unclear whether an IMBH in a star cluster can actually grow to be an SMBH within about a billion years. It is possible that either lack of gas supply or the radiation feedback from the accreting IMBH suppresses its growth (Milosavljević, Couch & Bromm 2009, Park & Ricotti 2012). In this case, the IMBHs would be left in star clusters or within galaxies in the present-day Universe, as suggested in some observational studies (Maccarone et al. 2007, Pasham, Strohmayer & Mushotzky 2014, Kızıltan, Baumgardt & Loeb 2017). Further studies are warranted to research the fate of the early IMBHs and their observational signatures.

Chapter 6

Conclusion

In this thesis, we study three seed BH formation models, namely, the direct collapse model, the super-Eddington accretion model, and the runaway stellar collision model. We examine the validity of these models in realistic situations. As far as we examined, all the three models are viable to produce seed BHs which may subsequently grow to the observed high-redshift SMBHs via gas accretion and BH mergers.

In Chapter 2, we first consider the direct collapse model. We study the efficiency of UV feedback by stellar radiation for an accretion phase of SMS formation, where we consider rapid episodic accretion of a mean rate $\sim 0.1\,M_{\odot}\,\mathrm{yr}^{-1}$. We focus on the difference of the evolution of the rapidly accreting protostars between constant accretion cases and episodic accretion cases. We first construct analytic functions of the episodic accretion histories using parameters which specify the durations of burst and quiescent phases, and the accretion rates during those phases. By calculating the stellar evolution with the parameterized accretion histories, we find that the episodically accreting supergiant protostar can significantly contract during prolonged quiescent phases which last longer than $10^3\,\mathrm{yr}$. The stellar contraction results in an increase of the effective temperature and UV feedback due to an emission of a significant amount of ionizing photons. This result is contrasted with those of the stellar evolution via constant rapid accretion, where the accreting supergiant protostar continues to be bloated and keeps its low surface temperature of $\sim 5000\,\mathrm{K}$.

In Chapter 3, we examine a highly gravitationally unstable accretion disk around a SMS by a 2D hydrodynamical simulation. We calculate a more realistic episodic accretion history by following the dynamics of fragments within the disk. We find that such a disk is more unstable and more frequently forms fragments with a typical number of fragments $\mathcal{O}(100)$, than a disk for a normal Pop III star formation case. We also compute stellar evolutions with the obtained accretion history in a post-process manner to investigate the efficiency of the stellar UV feedback. It is found that, even with the highly variable accretion history, the accreting protostar continues to be largely bloated and keeps the low effective temperature of $\sim 5000\,\mathrm{K}$ as found in the constant accretion cases. With a small amount of stellar UV photons emitted, UV feedback would be ineffective and the protostar would continue to grow until its mass reaches $\sim 10^5\,\mathrm{M}_{\odot}$ at which it collapses to produce a remnant BH.

In Chapter 4, we next consider the super-Eddington accretion model. We examine a BH accretion flow at a high rate with a super-Eddington luminosity source from the central region, which is assumed to be a nuclear accretion disk around the BH. We focus on the flow at large scales where BH gravity is comparable to gas pressure, near the Bondi radius. We examine whether a stable hyper-Eddington accretion flow is maintained in this high luminosity case. To this end, we perform 1D radiation hydrodynamics simulations with radiation from the central source, which is modeled by analytical functions with a parameter specifying the maximum luminosity that can exceed the

Eddington luminosity. It is found that the stable hyper-Eddington accretion is achieved even with at most 100 times the Eddington luminosity, when the two conditions are satisfied: the initial H II region is smaller than the Bondi radius and the ram pressure is stronger than the radiation force. Analytical results based on these two conditions can explain our simulations. To see the role of ram pressure, gas gravity and radiation force in detail, we model a motion of an optically thick gas shell just outside the H II region, which is driven by radiation force from the central source toward a rapid gas accretion flow. We find that both ram pressure and gas gravity are important to overcome the radiation force.

In Chapter 5, finally, we work on the runaway stellar collision model. In order to elucidate whether the runaway collision and IMBH formation are prevalent within first star clusters, we examine dynamics of the clusters which are identified in star-forming gas clouds within atomic-cooling halos. Firstly, the atomic-cooling halos are identified by performing cosmological SPH simulations. By replacing the SPH particles to star particles, assuming local star formation efficiency and an initial mass function, we then generate initial stellar distributions within star clusters. Using the star cluster initial conditions, we perform direct N-body simulations with stellar collisions and mergers. It is shown that the runaway stellar collisions occur in almost all star clusters and the massive stars form with a mass range of $\sim 400 - 1900\,\mathrm{M}_{\odot}$, which would gravitationally collapse to leave IMBHs at the end of their lifetimes. The final masses likely become larger with larger virial mass, larger central gas density and smaller velocity dispersion of the host halos. We also find that the ratio of IMBH mass to cluster mass in our simulations is nearly 1 per cent, which is consistent with the local star cluster observations.

Although we show that all the models are viable for formation of a seed BH, it remains still uncertain whether the seed grows to a SMBH. As future works, we will study processes of the seed BH growth in the context of the three models we have considered in this thesis. Intriguingly, an IMBH formed in a first star cluster (Chapter 5) can grow by subsequent mergers with stars and other BHs, possibly causing tidal disruption events and gravitational wave events. The event rates may be enhanced by the existence of an accretion disk, which exserts dissipative force on intruding stars (Just et al. 2012, Kennedy et al. 2016). The events may be observed, e.g., by a X-ray telescope like SwiftBAT and by gravitational-wave telescopes like LISA and DECIGO. Thus, by further studying the growth of the seed BH, we can compare the theoretical models with observations, which will lead to further understanding for origin of the high-redshift SMBHs.

References

Ade P. A. R. et al., 2016, A&A, 594, A13

Agarwal B., Dalla Vecchia C., Johnson J. L., Khochfar S., Paardekooper J.-P., 2014, MNRAS, 443, 648

Ahn K., Shapiro P. R., 2007, MNRAS, 375, 881

Alexander T., Natarajan P., 2014, Science, 345, 1330

Alvarez M. A., Wise J. H., Abel T., 2009, ApJ, 701, L133

Anninos P., Zhang Y., Abel T., Norman M. L., 1997, New Astronomy, 2, 209

Bañados E. et al., 2017, arXiv:1712.01860

Bachetti M. et al., 2014, Nature, 514, 202

Baraffe I., El Eid M. F., 1991, A&A, 245, 548

Baraffe I., Heger A., Woosley S. E., 2001, ApJ, 550, 890

Basu S., 1997, ApJ, 485, 240

Becerra F., Greif T. H., Springel V., Hernquist L. E., 2015, MNRAS, 446, 2380

Begelman M. C., 1978, MNRAS, 184, 53

Begelman M. C., 1979, MNRAS, 187, 237

Binney J., Tremaine S., 2008, Galactic Dynamics: Second Edition. Princeton University Press

Boley A. C., Lake G., Read J., Teyssier R., 2009, ApJ, 706, L192

Bromm V., Clarke C. J., 2002, ApJ, 566, L1

Bromm V., Loeb A., 2003, ApJ, 596, 34

Casertano S., Hut P., 1985, ApJ, 298, 80

Cha S.-H., Nayakshin S., 2011, MNRAS, 415, 3319

Chiaki G., Yoshida N., Hirano S., 2016, MNRAS, 463, 2781

Ciotti L., Ostriker J. P., 2001, ApJ, 551, 131

Colella P., Woodward P. R., 1984, Journal of Computational Physics, 54, 174

Cseh D. et al., 2014, MNRAS, 439, L1

De Rosa G. et al., 2014, ApJ, 790, 145

DeSouza A. L., Basu S., 2015, MNRAS, 450, 295

Devecchi B., Volonteri M., Colpi M., Haardt F., 2010, MNRAS, 409, 1057

Di Matteo T., Khandai N., DeGraf C., Feng Y., Croft R. A. C., Lopez J., Springel V., 2012, ApJ, 745, L29

Dunham M. M., Vorobyov E. I., Arce H. G., 2014, MNRAS, 444, 887

Ebisuzaki T. et al., 2001, ApJ, 562, L19

Fan X. et al., 2001, AJ, 122, 2833

Farrell S. A., Webb N. A., Barret D., Godet O., Rodrigues J. M., 2009, Nature, 460, 73

Fragile P. C., Olejar A., Anninos P., 2014, ApJ, 796, 22

Fregeau J. M., Cheung P., Portegies Zwart S. F., Rasio F. A., 2004, MNRAS, 352, 1

Fujii M., Iwasawa M., Funato Y., Makino J., 2007, PASJ, 59, 1095

Fujii M. S., Portegies Zwart S., 2014, MNRAS, 439, 1003

Fujii M. S., Portegies Zwart S., 2015, MNRAS, 449, 726

Gaburov E., Lombardi, Jr. J. C., Portegies Zwart S., 2010, MNRAS, 402, 105

Gallerani S., Fan X., Maiolino R., Pacucci F., 2017, PASA, 34, e022

Giersz M., Heggie D. C., 1994, MNRAS, 268, 257

Giersz M., Heggie D. C., 1996, MNRAS, 279, 1037

Glebbeek E., Gaburov E., de Mink S. E., Pols O. R., Portegies Zwart S. F., 2009, A&A, 497, 255

Glover S. C. O., Jappsen A.-K., 2007, ApJ, 666, 1

Goodman J., Tan J. C., 2004, ApJ, 608, 108

Greif T. H., Bromm V., Clark P. C., Glover S. C. O., Smith R. J., Klessen R. S., Yoshida N., Springel V., 2012, MNRAS, 424, 399

Greif T. H., Springel V., White S. D. M., Glover S. C. O., Clark P. C., Smith R. J., Klessen R. S., Bromm V., 2011, ApJ, 737, 75

Gürkan M. A., Freitag M., Rasio F. A., 2004, ApJ, 604, 632

Hahn O., Abel T., 2011, MNRAS, 415, 2101

Heger A., Fryer C. L., Woosley S. E., Langer N., Hartmann D. H., 2003, ApJ, 591, 288

Heger A., Woosley S. E., 2002, ApJ, 567, 532

Heggie D. C., Trenti M., Hut P., 2006, MNRAS, 368, 677

Hirano S., Hosokawa T., Yoshida N., Umeda H., Omukai K., Chiaki G., Yorke H. W., 2014, ApJ, 781, 60

Hosokawa T., Omukai K., 2009a, ApJ, 691, 823

Hosokawa T., Omukai K., 2009b, ApJ, 703, 1810

Hosokawa T., Omukai K., Yorke H. W., 2012, ApJ, 756, 93

Hosokawa T., Omukai K., Yoshida N., Yorke H. W., 2011, Science, 334, 1250

Hosokawa T., Yorke H. W., Inayoshi K., Omukai K., Yoshida N., 2013, ApJ, 778, 178

Hurley J. R., Tout C. A., Pols O. R., 2002, MNRAS, 329, 897

Ichimaru S., 1977, ApJ, 214, 840

Inayoshi K., Haiman Z., 2014, MNRAS, 445, 1549

Inayoshi K., Haiman Z., Ostriker J. P., 2016, MNRAS, 459, 3738

Inayoshi K., Hosokawa T., Omukai K., 2013, MNRAS, 431, 3036

Inayoshi K., Omukai K., 2012, MNRAS, 422, 2539

Inoue T., Omukai K., 2015, ApJ, 805, 73

Ishii M., Ueno M., Kato M., 1999, PASJ, 51, 417

Israel G. L. et al., 2017, MNRAS, 466, L48

Jeon M., Pawlik A. H., Greif T. H., Glover S. C. O., Bromm V., Milosavljević M., Klessen R. S., 2012, ApJ, 754, 34

Jiang L., Fan X., Vestergaard M., Kurk J. D., Walter F., Kelly B. C., Strauss M. A., 2007, AJ, 134, 1150

Jiang Y.-F., Stone J. M., Davis S. W., 2014, ApJ, 796, 106

Just A., Yurin D., Makukov M., Berczik P., Omarov C., Spurzem R., Vilkoviskij E. Y., 2012, ApJ, 758, 51

Kasliwal M. M., Lovelace R. V. E., Houck J. R., 2005, ApJ, 630, 875

Katz H., Sijacki D., Haehnelt M. G., 2015, MNRAS, 451, 2352

Katz J. I., 1977, ApJ, 215, 265

Kennedy G. F., Meiron Y., Shukirgaliyev B., Panamarev T., Berczik P., Just A., Spurzem R., 2016, MNRAS, 460, 240

Kimm T., Cen R., Rosdahl J., Yi S. K., 2016, ApJ, 823, 52

King A., 2003, ApJ, 596, L27

Kippenhahn R., Weigert A., Weiss A., 2012, Stellar Structure and Evolution. Springer-Verlag Berlin Heidelberg

Kızıltan B., Baumgardt H., Loeb A., 2017, Nature, 542, 203

Kollmeier J. A. et al., 2006, ApJ, 648, 128

Kormendy J., Ho L. C., 2013, ARA&A, 51, 511

Krauss M. I., Kilgard R. E., Garcia M. R., Roberts T. P., Prestwich A. H., 2005, ApJ, 630, 228

Kurk J. D. et al., 2007, ApJ, 669, 32

Latif M. A., Schleicher D. R. G., 2015, A&A, 578, A118

Latif M. A., Schleicher D. R. G., Schmidt W., Niemeyer J. C., 2013, MNRAS, 436, 2989

Liu J.-F., Bregman J. N., Bai Y., Justham S., Crowther P., 2013, Nature, 503, 500

Lodato G., Natarajan P., 2006, MNRAS, 371, 1813

Lützgendorf N. et al., 2013, A&A, 555, A26

Maccarone T. J., Kundu A., Zepf S. E., Rhode K. L., 2007, Nature, 445, 183

Machida M. N., Inutsuka S.-i., Matsumoto T., 2011, ApJ, 729, 42

Madau P., Haardt F., Dotti M., 2014, ApJ, 784, L38

Madau P., Rees M. J., 2001, ApJ, 551, L27

Magorrian J. et al., 1998, AJ, 115, 2285

Makino J., 1991, PASJ, 43, 621

Mazzucchelli C. et al., 2017, ApJ, 849, 91

McKee C. F., Tan J. C., 2008, ApJ, 681, 771

McKinney J. C., Tchekhovskoy A., Sadowski A., Narayan R., 2014, MNRAS, 441, 3177

Merritt D., Ferrarese L., 2001, MNRAS, 320, L30

Miller J. M., Fabbiano G., Miller M. C., Fabian A. C., 2003, ApJ, 585, L37

Milosavljević M., Couch S. M., Bromm V., 2009, ApJ, 696, L146

Mortlock D. J. et al., 2011, Nature, 474, 616

Muijres L., Vink J. S., de Koter A., Hirschi R., Langer N., Yoon S.-C., 2012, A&A, 546, A42

Narayan R., Yi I., 1994, ApJ, 428, L13

Nitadori K., Makino J., 2008, New Astronomy, 13, 498

Nitadori K., Makino J., Abe G., 2006, arXiv:astro-ph/0606105v2

Ohsuga K., Mori M., Nakamoto T., Mineshige S., 2005, ApJ, 628, 368

Omukai K., 2001, ApJ, 546, 635

Omukai K., Palla F., 2003, ApJ, 589, 677

Omukai K., Schneider R., Haiman Z., 2008, ApJ, 686, 801

Omukai K., Tsuribe T., Schneider R., Ferrara A., 2005, ApJ, 626, 627

Pacucci F., Volonteri M., Ferrara A., 2015, MNRAS, 452, 1922

Park K., Ricotti M., 2011, ApJ, 739, 2

Park K., Ricotti M., 2012, ApJ, 747, 9

Park K., Ricotti M., Natarajan P., Bogdanović T., Wise J. H., 2016, ApJ, 818, 184

Pasham D. R., Strohmayer T. E., Mushotzky R. F., 2014, Nature, 513, 74

Pezzulli E., Valiante R., Schneider R., 2016, MNRAS

Portegies Zwart S. F., McMillan S. L. W., 2002, ApJ, 576, 899

Rasio F. A., Fregeau J. M., Joshi K. J., 2001, in Astrophysics and Space Science Library, Vol. 264, The Influence of Binaries on Stellar Population Studies, Vanbeveren D., ed., p. 387

Reed D. S., Bower R., Frenk C. S., Jenkins A., Theuns T., 2007, MNRAS, 374, 2

Regan J. A., Johansson P. H., Wise J. H., 2014, ApJ, 795, 137

Reisswig C., Ott C. D., Abdikamalov E., Haas R., Mösta P., Schnetter E., 2013, Physical Review Letters, 111, 151101

Sakurai Y., Hosokawa T., Yoshida N., Yorke H. W., 2015, MNRAS, 452, 755

Sakurai Y., Inayoshi K., Haiman Z., 2016, MNRAS, 461, 4496

Sakurai Y., Vorobyov E. I., Hosokawa T., Yoshida N., Omukai K., Yorke H. W., 2016, MNRAS, 459, 1137

Sakurai Y., Yoshida N., Fujii M. S., Hirano S., 2017, MNRAS, 472, 1677

Sądowski A., Narayan R., 2016, MNRAS, 456, 3929

Sądowski A., Narayan R., McKinney J. C., Tchekhovskoy A., 2014, MNRAS, 439, 503

Schleicher D. R. G., Palla F., Ferrara A., Galli D., Latif M., 2013, A&A, 558, A59

Schmidt M., 1959, ApJ, 129, 243

Shibata M., Shapiro S. L., 2002, ApJ, 572, L39

Shibata M., Uchida H., Sekiguchi Y.-i., 2016, ApJ, 818, 157

Shu F. H., 1992, The physics of astrophysics. Volume II: Gas dynamics. University Science books

Soltan A., 1982, MNRAS, 200, 115

Spera M., Mapelli M., 2017, MNRAS, 470, 4739

Springel V., 2005, MNRAS, 364, 1105

Stacy A., Greif T. H., Bromm V., 2010, MNRAS, 403, 45

Stahler S. W., Palla F., Salpeter E. E., 1986, ApJ, 302, 590

Stone J. M., Norman M. L., 1992, ApJS, 80, 753

Susa H., Hasegawa K., Tominaga N., 2014, ApJ, 792, 32

Tanaka H., Takeuchi T., Ward W. R., 2002, ApJ, 565, 1257

Tanaka K. E. I., Omukai K., 2014, MNRAS, 439, 1884

Tanaka T., Menou K., 2010, ApJ, 714, 404

Tanikawa A., Yoshikawa K., Nitadori K., Okamoto T., 2013, New Astronomy, 19, 74

Toomre A., 1964, ApJ, 139, 1217

Tout C. A., Pols O. R., Eggleton P. P., Han Z., 1996, MNRAS, 281, 257

Trenti M., Padoan P., Jimenez R., 2015, ApJ, 808, L35

Truelove J. K., Klein R. I., McKee C. F., Holliman, II J. H., Howell L. H., Greenough J. A., 1997, ApJ, 489, L179

Van Borm C., Bovino S., Latif M. A., Schleicher D. R. G., Spaans M., Grassi T., 2014, A&A, 572, A22

Vanbeveren D., Belkus H., van Bever J., Mennekens N., 2009, Ap&SS, 324, 271

Venemans B. P. et al., 2013, ApJ, 779, 24

Visbal E., Haiman Z., Bryan G. L., 2014, MNRAS, 445, 1056

Volonteri M., Rees M. J., 2005, ApJ, 633, 624

Volonteri M., Silk J., Dubus G., 2015, ApJ, 804, 148

Vorobyov E. I., Basu S., 2009, MNRAS, 393, 822

Vorobyov E. I., DeSouza A. L., Basu S., 2013, ApJ, 768, 131

Vorobyov E. I., Zakhozhay O. V., Dunham M. M., 2013, MNRAS, 433, 3256

Wang R. et al., 2013, ApJ, 773, 44

Watarai K.-y., Fukue J., Takeuchi M., Mineshige S., 2000, PASJ, 52, 133

Whalen D., Norman M. L., 2006, ApJS, 162, 281

Willott C. J. et al., 2010, AJ, 140, 546

Wu X.-B. et al., 2015, Nature, 518, 512

Yoon S.-C., Dierks A., Langer N., 2012, A&A, 542, A113

Yorke H. W., Bodenheimer P., 2008, in Astronomical Society of the Pacific Conference Series, Vol. 387, Massive Star Formation: Observations Confront Theory, Beuther H., Linz H., Henning T., eds., p. 189

Yoshida N., Abel T., Hernquist L., Sugiyama N., 2003, ApJ, 592, 645

Yoshida N., Omukai K., Hernquist L., 2008, Science, 321, 669

Yu Q., Tremaine S., 2002, MNRAS, 335, 965

Yungelson L. R., van den Heuvel E. P. J., Vink J. S., Portegies Zwart S. F., de Koter A., 2008, A&A, 477, 223